SERDP

FINAL REPORT

Area and Depth Coverage Assessment for Acoustic Unexploded Ordnance Detection Surveys

Robbert van Vossen
Marten Nijhof
Mark Prior
A.J. Duijster
D.W. van der Burg
J.J.M. van de Sande,
I. Mulders
TNO (Netherlands Organisation for Applied Scientific Research)

January 2021

SERDP Project MR20-1484

DISTRIBUTION STATEMENT A
This document has been cleared for public release.

REPORT DOCUMENTATION PAGE

Form Approved
OMB No. 0704-0188

1. REPORT DATE *(DD-MM-YYYY)* 02-01-2021	**2. REPORT TYPE** SERDP Final Report	**3. DATES COVERED** *(From - To)* 20-09-2019 To 30-01-2021

4. TITLE AND SUBTITLE
Area and Depth Coverage Assessment for Acoustic Unexploded Ordnance Detection Surveys

5a. CONTRACT NUMBER W912HQ19P0116

5b. GRANT NUMBER

5c. PROGRAM ELEMENT NUMBER

6. AUTHOR(S)
R. van Vossen, A.J. Duijster, D.W. van der Burg, J.J.M. van de Sande, I. Mulders

5d. PROJECT NUMBER MR20-1484

5e. TASK NUMBER

5f. WORK UNIT NUMBER

7. PERFORMING ORGANIZATION NAME(S) AND ADDRESS(ES)
TNO
OUDE WAALSDORPERWEG 63
2597 AK
THE HAGUE
THE NETHERLANDS

8. PERFORMING ORGANIZATION REPORT NUMBER
MR20-1484

9. SPONSORING / MONITORING AGENCY NAME(S) AND ADDRESS(ES)
SERDP PROGRAM OFFICE
4800 MARK CENTER DRIVE,
SUITE 16F16
ALEXANDRIA VA, 22350-3600

10. SPONSOR/MONITOR'S ACRONYM(S)
SERDP

11. SPONSOR/MONITOR'S REPORT NUMBER(S)
MR20-1484

12. DISTRIBUTION / AVAILABILITY STATEMENT
DISTRIBUTION STATEMENT A. Approved for public release: distribution unlimited.

13. SUPPLEMENTARY NOTES

14. ABSTRACT
Low frequency synthetic aperture sonar (SAS) is a key technique for the detection and characterization of unexploded ordnance (UXO) in the underwater environment. For buried UXO, however, it is rather difficult to determine the range and depth up to which the detection of UXO is feasible. This critically depends on the detection system properties, environmental properties such as water depth and sediment type, target properties, and the actual burial depth up to which UXO needs to be detected. For the evaluation of the effectiveness of UXO detection surveys, it is therefore necessary to assess which area effectively has been covered by the survey, and up to which depth effective coverage has been obtained.
The objective of the current project is to develop an approach for coverage assessment. The development and evaluation of the coverage assessment methodology is supported by using data examples acquired with TNO's low-frequency synthetic aperture sonar (LF-SAS) system.

15. SUBJECT TERMS
Acoustic Unexploded Ordnance, Detection Surveys

16. SECURITY CLASSIFICATION OF:			**17. LIMITATION OF ABSTRACT**	**18. NUMBER OF PAGES**	**19a. NAME OF RESPONSIBLE PERSON**
a. REPORT	**b. ABSTRACT**	**c. THIS PAGE**			Robbert van Vossen
UNCLASS	UNCLASS	UNCLASS	UNCLASS	77	**19b. TELEPHONE NUMBER** *(include area code)* 0031888661052

Standard Form 298 (Rev. 8-98)
Prescribed by ANSI Std. Z39.18

Contents

Abstract

Low frequency synthetic aperture sonar (SAS) is a key technique for the detection and characterization of unexploded ordnance (UXO) in the underwater environment. For buried UXO, however, it is rather difficult to determine the range and depth up to which the detection of UXO is feasible. This critically depends on the detection system properties, environmental properties such as water depth and sediment type, target properties, and the actual burial depth up to which UXO needs to be detected. For the evaluation of the effectiveness of UXO detection surveys, it is therefore not only relevant to analyze the acquired data to determine the presence or absence of UXO, but also to assess which area effectively has been covered by the survey, and up to which depth effective coverage has been obtained.

The objective of the current project is to develop an approach for coverage assessment, and to evaluate the applicability of the coverage assessment approach. The development and evaluation of the coverage assessment methodology is supported by using data examples acquired with TNO's low-frequency synthetic aperture sonar (LF-SAS) system.

The coverage assessment approach relies on high-fidelity target-in-environment response (TIER) simulations of UXO objects of interest, which are obtained using Finite Element Modelling (FEM) simulations. They are subsequently merged with measured reverberation data. Using augmented targets, it becomes possible to assess whether a target of interest would be detectable, if present. The detectability is assessed in synthetic aperture sonar (SAS) images using an intensity threshold detector, i.e. by considering the Signal Excess (SE) for different target depths, target orientations, and target ranges. The coverage assessment for more sophisticated detectors would be supported as well by the developed high-fidelity TIER simulation approach.

The coverage assessment results show that the maximum range for detecting buried objects is limited by the critical angle of incidence for a sidelooking LF-SAS system. It is difficult to obtain information on sediment sound speed using an LF-SAS system, which primarily senses back-scattering properties of the seabed. It is therefore important to collect this information on seabed properties by alternative means, e.g. grab samples and/or gravity cores. There are well-established relations between grain size and sediment sound speed.

The coverage assessment methodology critically relies on the calibration of the measurement system, processing, and TIER simulation chain. Hardware characteristics, such as beam patterns, need to be established by conducting basin measurements, and scale factors introduced in data acquisition, processing, and simulations need to be taken into account. Errors in the calibration will result in biased coverage assessment results.

The coverage assessment approach has been successfully demonstrated on experimental data acquired by the LF-SAS system near Gdynia, Poland. Simulation results for the signal-to-reverberation ratio (SRR) for a scientific cylindrical target agree well with measurements. Single-view coverage assessment results are in agreement with range and depth trends in SRR observed in experimental data.

Finally, coverage assessment results can be generated during an UXO detection survey, provided that the simulated TIER SAS images are generated prior to the survey. Timely availability of coverage assessment results helps to improve the quality of UXO surveys. Furthermore, averaged performance curves, such as P(y) curves, are useful input to the planning of future UXO surveys. This study therefore demonstrated that high-quality coverage assessment results can be efficiently obtained to aid UXO survey planning, execution, and evaluation.

List of Figures

the circle quadrant). The variables ‘a’ and ‘d’ represent the source/receiver depth and water depth, respectively. Labels are explained in the text of Section 6.3.

Figure 6-4: The arrival angles of the same contributors as in Figure 6-3, as function of the slant range of the direct path. The variables ‘a’ and ‘d’ represent the source/receiver depth and water depth, respectively. Labels are explained in the text of Section 6.3.

Figure 6-5: An example of two SAS images of the same area and with the same settings, only taken in different wind conditions: wind speed of (a) 13 m/s and (b) 4 m/s. Source: [20]

Figure 7-1: Example of LF-SAS image with variability in the background. The image is divided in two segments with different background statistics, and consequently a different detection threshold.

Figure 8-1: Photograph of NL-REF targets.

Figure 8-2: Example of LF-SAS images for a proud object (NL-REF) and the same object buried at 0.3 m depth. The vertical axis shows the across-track range, respectively 18, 28, 38 and 58 meter for the proud cylinder, and 19, 29, 39 and 47 meter for the buried cylinder.

Figure 8-3: Maximum SRR for the proud and buried objects shown in Figure 8-2.

Figure 8-4: Downlooking image below the sonar, obtained with the upper band of the MUD LF-SAS system, acquired in the Haringvliet environment. Layering of the seabed can be recognized, with a mud layer roughly between 10.6 and 11.4 m depth. The backscattering strength increases in the sand layer.

Figure 8-5: Simulated recordings for a diffractor buried in sand with a low (a) and fast velocity (b), water arrival time snapped to peak shown with dashed line. Figures (c) and (d) are after flattening on water arrival time.

Figure 8-6: Example from field data of a diffraction of a buried object.

Figure 8-7: Normalized backscattering vs slant range for different sub-bands for the Haringvliet (left) and Gdynia (right) sites.

Figure 8-8: Normalized backscattering vs slant range for the Haringvliet site, with curve fits superimposed. The steep curves are interpreted to correspond to the BSS from the subsurface interface. The smaller decay with slant range is related to the interface scattering at the water/mud interface. At slant ranges beyond 20 m, the interpretation of the data becomes increasingly complex due to multipath contributions.

Figure 8-9: Attenuation coefficient vs grain size, based on [18].

Figure 9-1: Simulation chain for target in environment response including processing.

Figure 9-2: The different environments that can be modelled in the FE simulations. The surrounding environment can be either an homogeneous environment (a) or include a single sediment layer (b-d). In the latter case the target can be either proud, buried or partly buried.

Figure 9-3: Sketch showing incident field, the 1st and 2nd order scattering field of a target and the corresponding far field [29].

Figure 9-4: The solid red line shows the array positions (source and receivers) for the simulated run. The open red circle represents the target position and the black lines show the orientation of the incident field. The right panel shows NL-CYL.

Figure 9-5: Amplitude response (dB) for object NL-CYL as a function of frequency and array location.

sand. Right column: medium sand. Note the decreased visibility with range for medium sand compared to very fine sand due to the smaller critical angle.

Figure 12-5: TIER SAS images illustrating the effect of burial depth. Increasing burial depth from left to right.

Figure 12-6: TIER SAS images illustrating the effect of orientation. In dashed white line the target outline.

Figure 12-7: Detrending of the SAS image for SRR determination.

Figure 12-8: SRR as a function of crossline range and target orientation for NL-REF TIER simulations. Sediment type ‘very fine sand’ on the left, ‘medium sand’ on the right. Burial depth top top target is 0.5 m.

Figure 12-9: SRR as function of crossline range for buried and proud NL-REF, real data observations from Gdynia area.

Figure 12-10: P(y) curve for sediment type ‘very fine sand’ (left) and ‘medium sand’ (right), for two different detector thresholds, 20 dB and 25 dB, respectively. Dashed line indicates critical angle range.

Figure 12-11: (a) SAS image of an example track from the survey. (b) Derived background trend with added detection threshold. (c and d) Coverage maps for NL-REF for ‘very fine sand’ and ‘medium sand’, with target orientation 30° and target burial depth of 0.5 m.

Acronyms

APL	Applied Physics Laboratory
AUV	Autonomous Underwater Vehicle
BL	Background Level
BOSS	Buried Object Scanning Sonar
BSS	Back-Scattering Strength
CMRE	Centre for Maritime Research and Experimentation
DFFT	Discrete Fast Fourier Transform
DIFFT	Discrete Inverse Fast Fourier Transform
DT	Detection Threshold
FE(M)	Finite-Element (Modeling)
FFT	Fast Fourier Transform
HF	High Frequency
INS	Inertial Navigation System
LF	Low Frequency
MBES	MultiBeam EchoSounder
MUD	Mine Underground Detection
NRL	Naval Research Laboratory
NSWC-PC	Naval Surface Warfare Centre, Panama City
PG	Processing Gain
PHINS	PHotonic Inertial Navigation System
REMUS	Remote Environmental Monitoring Units
RNLN	Royal Netherlands Navy
ROC	Receiver Operating Characteristic
ROV	Remotely Operated Vehicle
RTK-GPS	Real Time Kinematic Global Positioning System
SAS	Synthetic Aperture Sonar
SBES	Single-Beam EchoSounder
SBI	Sub-Bottom Imager
SBP	Sub-Bottom Profiler
SBR	Signal-to-Background Ratio
SE	Signal Excess
SERDP	Strategic Environmental Research and Development Program
SNR	Signal-to-Noise Ratio
SRR	Signal-to-Reverberation Ratio
SSAM	Small Synthetic Aperture Minehunter
SSS	Side Scan Sonar
TEL	Target Echo Level
TIER	Target In Environment Response
TNO	Netherlands Organisation for Applied Scientific Research
TS	Target Strength
UXO	UneXploded Ordnance

1 Introduction

This is the final report of the SERDP MR-20-S1-1484 project entitled '*Area and Depth Coverage Assessment for Unexploded Ordnance Acoustic Detection Surveys*'. Coverage is meant in this context as the volume, characterized in terms of range and depth, in which the unexploded ordnance (UXO) objects of interest can be detected with sufficient probability of detection at an acceptable level of false positives.

Figure 1-1 illustrates the coverage assessment problem. It presents LF-SAS imagery acquired using TNO's Mine Underwater Detection (MUD) system in two different environments [1]. The first image is acquired in an environment with a sandy seabed, the second image in an environment with a mud layer with sand underneath. It is a former tidal estuary, but the access to the sea has been closed off since 1971 to protect the inland from flooding, and the mud layer has been formed since then. As a consequence of the fluvial-tidal characteristics in the past, the mud/sand interface is not flat and has a complex sediment structure, and the mud/sand interface is likely to contain wave ripple features.

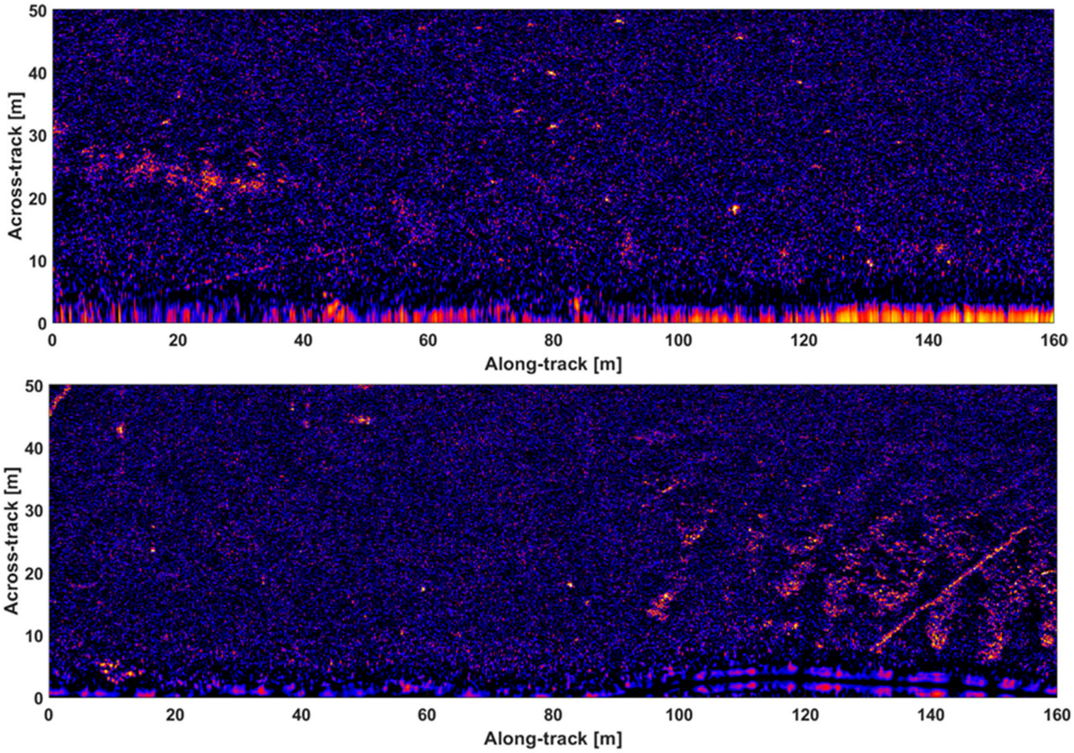

Figure 1-1: Example of LF-SAS images in an environment with a sandy seabed (top) and with a layered seabed, consisting of a mud layer with sand underneath (bottom).

In both environments, it is a non-trivial problem to assess up to which range and depth UXO objects of interest, such as shells and bombs (Figure 1-2) or UXO of smaller calibre, are detectable[1]. This does not only depend on the target and environmental conditions, but also on the sonar system characteristics, such as frequency, bandwidth, transmitter properties, and processing gain. Insight in the achieved range and depth coverage is important to support further planning of both wide area and detailed UXO surveys. This knowledge is

---

[1] The example images here are clean UXO test objects. In practice, corrosion and/or bio-fouling could occur, leading to variation in target scattering properties even if the type of UXO to be detected is known [2].

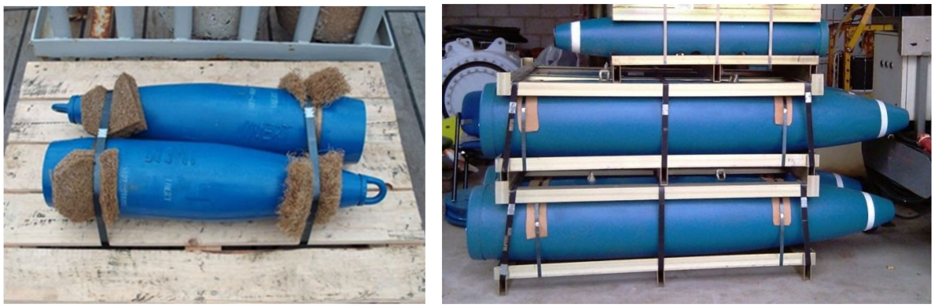

Figure 1-2: Example of UXO exercise objects; 155 mm shells (left) and 2000 lb concrete filled bombs (right).

required to establish the performance achieved in an UXO survey, i.e. what is the risk that UXO at a specific position and depth remains undetected.

To establish an approach for coverage assessment, the following research questions have been formulated to guide the research:

A) *Which environmental and target information is needed for range and depth coverage assessment?*
B) *How can relevant environmental information be obtained from LF-SAS data?*
C) *How can the detectability of relevant UXO targets be determined? How can aspect-dependent variations in target strength be taken into account in the coverage assessment approach?*
D) *How can coverage assessment be validated?*

The coverage assessment methodology will be developed for monostatic LF-SAS systems, which are considered as the main type of acoustic sensor systems for buried UXO detection. Other configurations (bistatic) or sensors (side scan sonar, parametric sonar systems) could be of interest as well, and we anticipate that the methodology could be generalized to these type of systems as well.

To establish the coverage that is achieved in a survey, it is required to establish coverage for a single track first. The next step then is to aggregate the single-track coverage results to assess coverage for an entire survey. To assess the feasibility of the coverage assessment approach, we primarily focus on the single-track coverage assessment, which is considered as the critical step. The generalization from single track results to an entire survey is not addressed in the current study.

This report is organized as follows:

- Section 2 provides an inventory of sonar systems for buried UXO detection.
- Section 3 gives a description of the envisaged methodology for coverage assessment and defines relevant terminology. Different terms are further developed in the subsequent sections, including aspects and choices related to the implementation of coverage assessment.
- Section 4 introduces TNO's MUD system, which will serve as a use case to support the development of the coverage assessment methodology.
- Sections 5-7 provide an overview of physics related to the coverage assessment methodology, with Section 5 focusing on the Target In Environment Response (TIER), Section 6 on the environmental response, and Section 7 on the UXO detectability.
- In Section 8, environmental assessment approaches are developed, i.e. approaches to obtain information on the environmental parameters that are required for coverage assessment. It

is also investigated whether information on those parameters can be obtained from measurements acquired from an LF-SAS system.

- In Sections 9 and 10, the TIER simulation approach and the corresponding processing are discussed, such that TIER LF-SAS images can be generated at a range and depth of interest, including the effects of LF-SAS processing.
- Section 11 discusses the calibration and validation of TIER processing and modeling. Calibration is essential before TIER simulations can be combined with measured reverberation data, and representative estimates of SNR can be obtained.
- Section 12 presents coverage assessment results, and evaluates these results by comparison to measurements.
- The conclusions of this study are presented in Section 13.

2 Inventory of sonar systems for buried object detection

In this section different system configurations will be identified, along with examples of these systems. The focus is on LF-SAS systems in monostatic configurations. Parametric echo sounders are not considered here as they are impractical for performing area surveys due to their limited footprint. System deployment is varied: on AUVs, ROVs, tow body, or systems attached to surface platform. The systems are listed based on the dominant looking direction of the systems, ranging from downlooking to sidelooking.

Downlooking systems have the receiver array placed horizontally perpendicular to the sailing direction and source (array) placed centrally on the track in close proximity. Acoustic wave propagation is predominantly in the vertical direction, perpendicular to the seabed. Examples of these systems are the GeoAcoustics system [3][4] which uses depth migration for imaging of reflections; The Pangeo Subsea Sub-Bottom Imager (SBI) system [5], operationally used for UXO surveys (wind farms) and depth of burial surveys (cables); The PennState Sediment Volume Search Sonar shallow water system [6]. These systems have the following characteristics in common:

- a good depth coverage below the seabed (up to 10 m depending on sediment properties);
- swath width is limited (2-5 m), giving a low coverage rate for area surveys; and
- difficulty to detect objects in the presence of a layered seabed.

Subsequently, there are downlooking systems with near vertical angle of incidence to inclined angle of incidence. Examples of these are: Buried Object Scanning Sonar (BOSS) [7][8]; Next-generation BOSS [9]; Small Synthetic Aperture Minehunter (SSAM) [10][11]. The NRL Structural Acoustic Look-Down and Side-Look Sonar [12][13][14] has both downlooking and sidelooking sensors. The TNO MUD system [15][16][1] has a receiver array that can be tilted from downlooking to sidelooking orientation. It will be covered in more detail in Chapter 4.

In sidelooking mode, last-mentioned systems offer a large swath width, giving a good coverage rate for area surveys. With inclined angle of incidence, pre-critical and postcritical incidence at the water bottom and deeper sediment layers become important. Object backscattering is dominant. The effect of inclining angle of incidence on sub-bottom acoustic imaging is illustrated in [17].

3 Coverage assessment methodology

In the previous section, an inventory for sonar systems for buried object detection was presented. There is a variety of sonar systems that operate either in a downlooking geometry or in a sidelooking geometry. The objective in this section is to develop a coverage assessment methodology that is able to assess the range and depth coverage for different types of buried object sonar systems.

3.1 Sonar equation

The sonar equation will be used as a starting point for the development of a coverage assessment methodology, i.e. to determine whether an UXO object of interest is detectable at a certain position. The sonar equation reads:

$$\mathrm{SE} = \mathrm{TEL} - \mathrm{BL} + \mathrm{PG} - \mathrm{DT}, \qquad (3.1)$$

where SE is signal excess, TEL denotes the target echo level, BL the background level, PG the processing gain, and DT the detection threshold, respectively.

In practice, it is difficult to estimate the signal and background level prior to processing, and the processing gain individually. It is therefore more convenient to consider both the signal level and background level including processing. This leads to the sonar equation in the form:

$$\mathrm{SE} = \mathrm{TEL}^{*} - \mathrm{BL}^{*} - \mathrm{DT} \qquad (3.2)$$

where $[]^{*}$ denotes the quantity including processing. Processing includes beamforming or SAS processing and matched filtering. It influences both signal and background level. The background level comprises reverberation and noise.

3.2 Target echo level in coverage assessment

In coverage assessment, the detectability of a target that may be present needs to be assessed, i.e. would a specific target be detectable. This requires a capability to estimate the target echo level, also referred to as the Target In Environment Response (TIER), including the effects of processing. This comprises:

1) A simulation capability to estimate the target echo level;
2) A calibrated processing chain; and
3) Insight in the effect of signal processing on the target echo level.

The idea is to compare the TEL including processing to the BL including processing, so TEL^{*} compared to BL^{*}.

Approaches for estimating the TIER including the processing, including the information that is required as input to a TIER estimating process, are further discussed in Chapter 5.

3.3 Background level in coverage assessment

The background level including the processing is measured. This implies that range and depth coverage assessment does not rely on model predictions for reverberation and noise. It requires a capability for estimating the target echo level including the effects of data acquisition and processing. In addition, the detection threshold will have to be established.

To enable a meaningful interpretation of achieved coverage, a thorough understanding of the environmental response is required. For this purpose, factors contributing to the environmental response will be discussed in more detail in Chapter 6. Understanding of the environmental response can also help to make inferences on the environmental parameters that are required as input to estimate the TIER by using data-driven methodologies.

3.4 Detection threshold in coverage assessment

The detection threshold is a difficult term to estimate. It is defined as the signal-to-background ratio (including processing) at which a 50% probability of detection is achieved at an acceptable false positive rate [18]. The detection threshold depends on the detection process, and is commonly established based on practical experience.

An important factor that reduces the detection performance, and consequently increases the detection threshold, is variability in the environmental response. The processing to mitigate this variability, which is commonly referred to as normalization, should therefore be taken into account in the assessment of detection performance of a sonar system in a specific environment. It is, however, rather challenging to estimate the detection threshold for different types of buried object detection sonar systems including the processing tailored to these systems. A generic approach would be to establish Receiver Operator Characteristic (ROC) curves in which the probability of detection is plotted against the false positive rate. The Signal-to-Noise Ratio (SNR) at which a 50% probability of detection is achieved at an acceptable user-defined false alarm rate is then the detection threshold. The detection threshold term is further discussed in Chapter 7.

3.5 Reducing uncertainties in environmental information

The coverage assessment methodology outlined in this Chapter relies on the availability of environmental information. Not all information will be a priori available at a sufficient level of accuracy. We will therefore pay special attention to parameters on which commonly insufficient knowledge is available, and assess methodologies how additional information on these parameters can be obtained. It will be explored whether through-the-sensor approaches can be used to make direct measurements or inferences on unknown parameters. When through-the-sensor methodologies cannot provide the requested information, auxiliary sensors or supporting measurements may have to be done.

3.6 Envisaged result of coverage assessment

Coverage assessment provides information on the progress and effectiveness of UXO surveys. It is expected that the coverage depends on a number of factors, including:

- target scattering properties;
- target depth;
- target range, or more precisely the grazing angle;
- acoustic properties of the seabed;
- water depth;
- sonar system properties (frequency, bandwidth, transmit beampattern, receiver array properties); and
- sonar processing.

The development and application of the coverage assessment methodology should provide important information on the potential and limitations of buried object sonar systems in different configurations.

4 Use case for coverage assessment: MUD system

The development and implementation of the coverage assessment approach will be supported by using the Mine Underground Detection (MUD) system as a use case.

The MUD system is shown in Figure 4-1. The system is platform based and is applicable to environments with a water depth greater than 5.0 m. It combines low-frequency synthetic aperture sonar (LF-SAS) with a high-frequency side scan sonar (HF-SSS) that operates at a center frequency of approximately 450 kHz, such that detailed information on the seabed is obtained, both in terms of scattering properties and bathymetry. The LF-SAS system delivers the capability to detect and localize buried objects.

The system has a 2D receiver array that can be lowered below the platform. The tilt angle of the sonar frame can be adjusted to change the illumination of the seabed. As a result, the system can be used both in a downlooking and a sidelooking configuration.

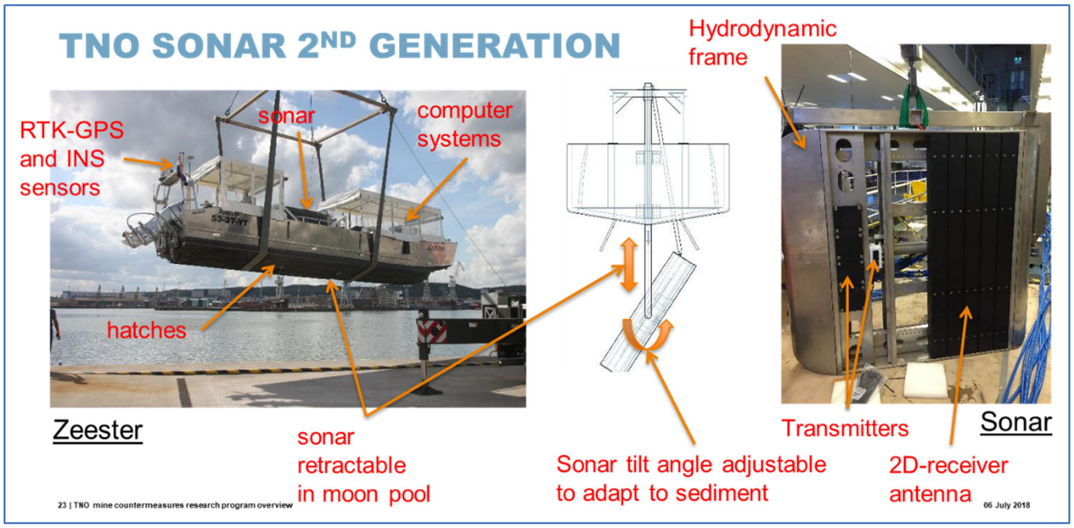

Figure 4-1: TNO's prototype Mine Underground Detection (MUD) system.

The system is suitable as a use case for coverage assessment, because coverage can be assessed for a broad range of aspect angles and for a broad range of frequencies. Furthermore, data have been collected in different environments. It enables therefore the investigation of most of the aspects that are expected to influence the coverage, as mentioned in the previous section.

Figure 4-2 presents imagery in multiple frequency bands that is acquired in a single pass by the MUD system. It shows an upper band and lower band image from the LF-SAS MUD system, and a HF-SSS image. The high frequency image does not reveal any contrast difference of importance, whereas high scattering contacts are clearly observable in the LF-SAS MUD images in both frequency bands, which correspond to a deployed buried object. Another interesting observation is a larger variability in the background response in the lower frequency band compared to the higher frequency band of the MUD system. A similar observation has been presented by Sternlicht et al. with SSAM [10].

To illustrate that a multi-frequency system has a potential for collecting relevant information on the environment that is needed for coverage assessment during a target detection survey, georeferenced HF-SSS and LF-SAS imagery is shown in Figure 4-3. The images reveal that there is hardly texture visible on the HF-SSS imagery in the specific environment where these images are collected, whereas high and low intensity patterns are observable on the LF-SAS imagery. The explanation is that the images were collected in an area with a seabed consisting of a mud layer with sand underneath. At low frequencies for which attenuation of sound in mud is not significant, the mud layer becomes acoustically transparent. At high frequencies, on the other hand, the attenuation of sound in the sediment becomes so high that the scattering from the water/mud interface, or from the volume just below the interface, becomes dominant. The differences in intensity in the LF-SAS imagery are attributed to wave ripples on the mud-sand interface. The area in which the data are collected is a former tidal estuary, which has been closed-off from the sea by a dam for which construction was completed in 1971. Since then, the mud layer has been formed due to fluvial deposition. The mud/sand interface still has features, such as wave ripples, related to the tidal characteristics in the past. The straight sharp line in the LF-SAS image with high scattering is attributed to the presence of gas in the sediment caused by anchor drag in the past.

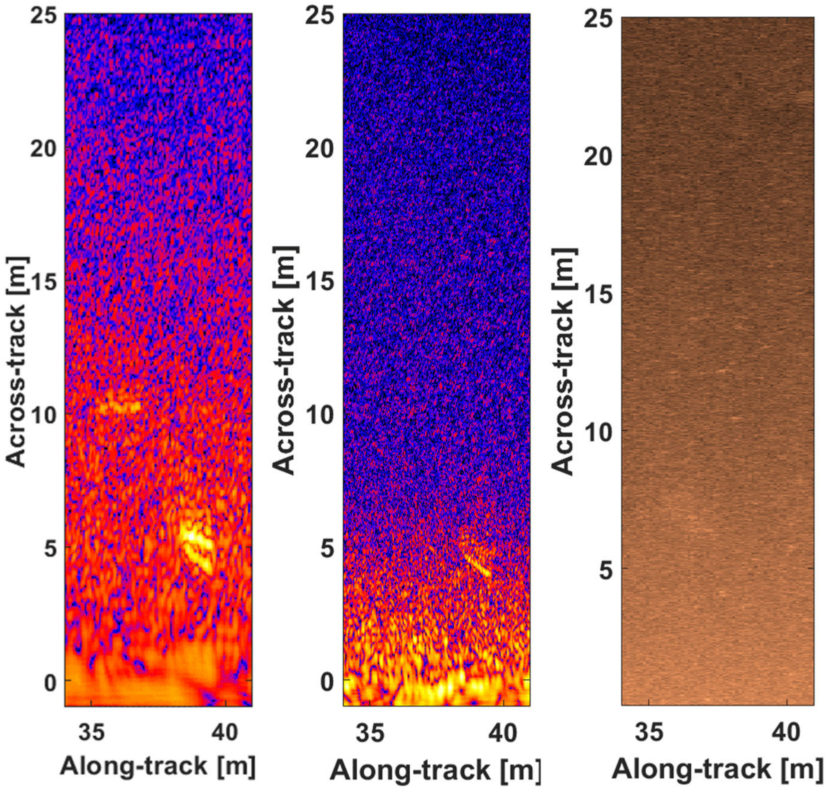

Figure 4-2: Imagery that is simultaneously obtained with the MUD system in different frequency bands: LF-SAS image – lower band (left); LF-SAS image – upper band (center); HF-SSS image (right).

The interpretation above is further supported by the corresponding interferometric height estimates (Figure 4-4) that are derived both from the HF-SSS and LF-SAS images. The interferometric height estimates reveal that they are different for HF-SSS and LF-SAS images. For HF-SSS, dominant scattering occurs at the water/mud interface, or close to this interface. As a consequence, the HF-SSS interferometric result is interpreted as being the water/mud interface. For LF-SAS, on the other hand, dominant scattering is expected to occur at the mud/sand interface. This is indeed confirmed by the LF-SAS interferometric height estimates.

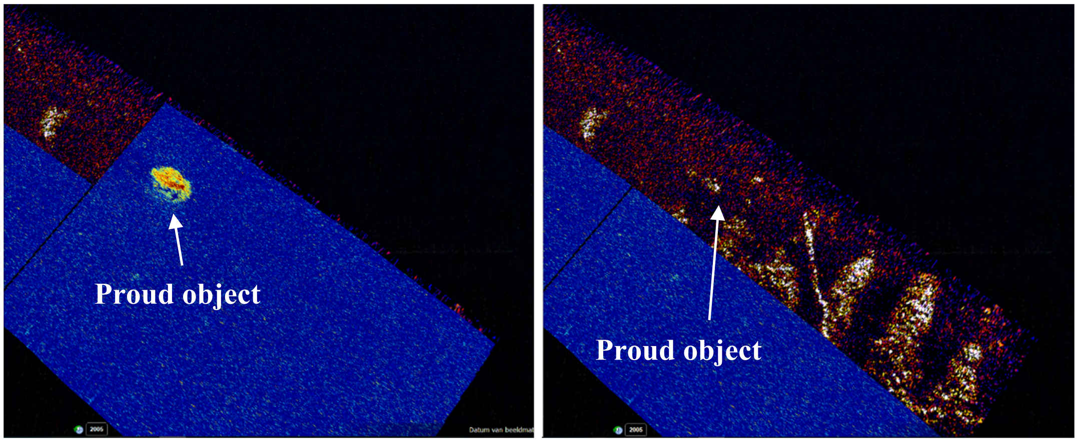

Figure 4-3: Georeferenced images obtained with the HF-SSS (top layer with blue-yellow-red color scale with high intensity in red) and with the LF-SAS system (black-red-yellow, with high intensity in yellow). A contact corresponding to a proud object is clearly visible in the HF-SSS image layer (left). It has a more compact high-intensity footprint in the LF-SAS image layer (right). The LF-SAS image layer furthermore shows that the environmental response in this frequency band is completely different from the HF-SSS.

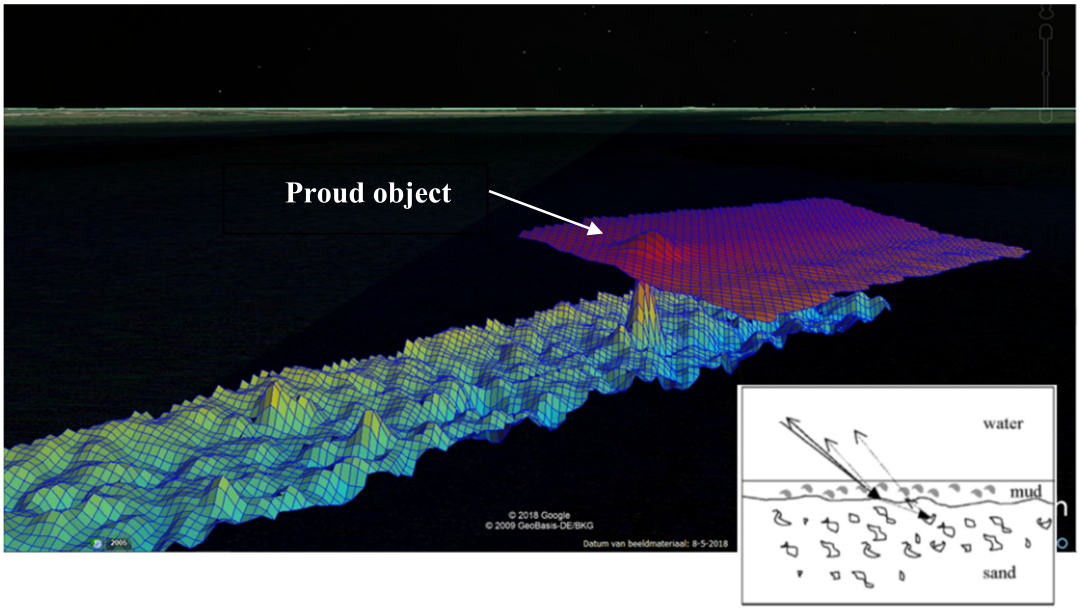

Figure 4-4: LF-SAS and HF-SSS interferometric height estimates corresponding to the same area as the intensity data in Figure 4-3, and a representative cartoon to illustrate the situation [19]. The HF-SSS interferometric height estimates are interpreted as the height of the water/mud interface and are shown in purple. The bottom layer corresponds to the LF-SAS interferometric height estimates. At low frequencies, dominant scattering occurs at the mud/sand interface. Note that the LF-SAS and HF-SSS interferometric height estimates are identical for the proud object.

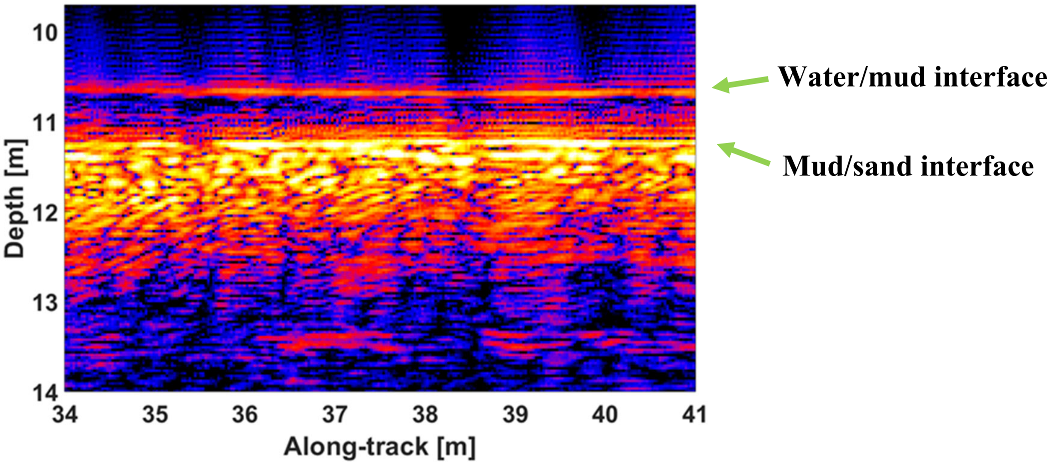

Figure 4-5: Downlooking image below the sonar, obtained with the upper band of the MUD LF-SAS system. The mud layer in the depth range between 10.5 and 11.5 m is also observable in the downlooking configuration.

Note that the LF-SAS and HF-SSS interferometric height estimates are similar for the surface contact for which corresponding intensities are shown in Figure 4-3.

Downlooking measurements obtained in this environment are presented in Figure 4-5. In a downlooking configuration, or by using a sub-bottom profiler as an auxiliary sensor (which should not interfere with the primary sensor), information on layering of the seabed can be obtained. Reflection of sound at the water/mud interface and at the mud/sand interface can be observed in this image, supporting the interpretation of the LF-SAS and HF-SSS interferometric height estimates.

A last example of the MUD system in this environment presents again imagery of the lower and upper band of the LF-SAS system, together with the corresponding interferometric coherence (Figure 4-6). Interferometric coherence is a metric that indicates the similarity between the observations made at the two sub-arrays that are used to derive interferometric height estimates [20]. Interferometric coherence is a normalized cross-correlation, which is equal to 1 when waveforms are identical. It decreases when waveforms are decorrelated. A high value indicates that a single scatterer is dominant in the range window that is being considered. A lower value indicates that multiple scattering mechanisms are of importance. This causes interference patterns and, as a consequence, decorrelation of the recorded signal on the two sub-arrays.

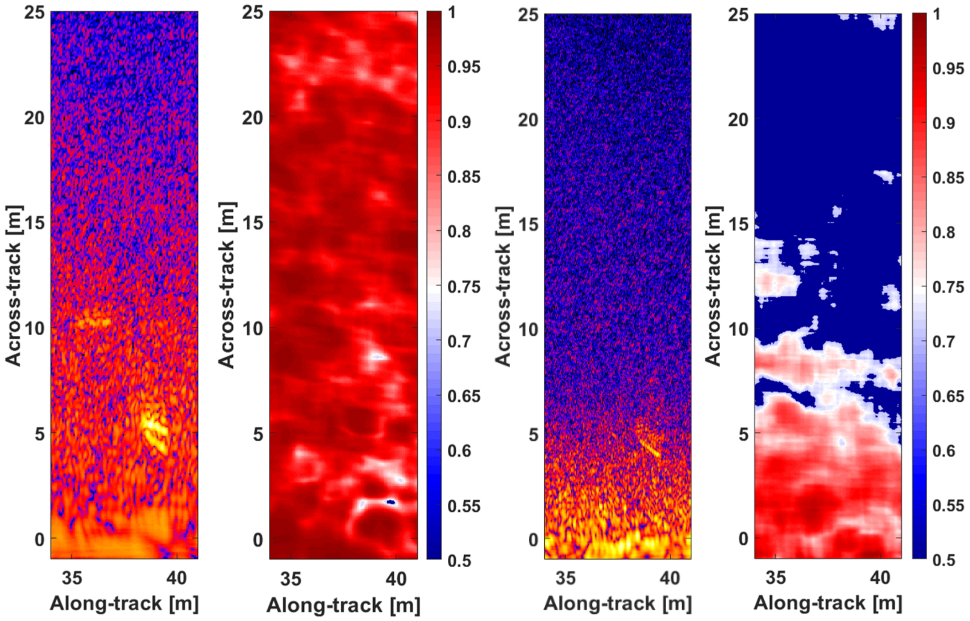

Figure 4-6: LF-SAS images and the corresponding interferometric coherence. The left two panels are the lower band, the right two images the upper band.

The interesting observation is that a high interferometric coherence is obtained for the lower band of the LF-SAS system, whereas the interferometric coherence rapidly decreases with range on the higher band. This suggests that attenuation of sound in the mud layer starts to become significant in the upper band of the LF-SAS system. Compared to the lower band, the scattering received from the mud/sand interface is, according to the interferometric coherence metric, not dominant any more at longer ranges.

The examples presented in this section illustrate that the MUD system use case enables to investigate both range and depth coverage assessment in a downlooking and sidelooking configuration. Furthermore, the system covers a frequency range that is sufficiently broad such that frequency diversity in the environmental response can be observed. The data products obtained with the MUD system suggest that relevant information may be obtained to aid coverage assessment. It is anticipated, though, that this will strongly depend on the environmental conditions that are encountered, i.e. the concepts presented in this section may only be applicable to this specific environment. The application of the coverage assessment methodology introduced in Chapter 3 therefore requires a more generalized description on which information is required for coverage assessment in different environmental conditions, and how this information can be obtained. This will be discussed in the next Chapters for the different relevant terms in the sonar equation.

5 Target in environment response

This Chapter discusses the Target In Environment Response (TIER). First, target scattering will be discussed in Section 5.1. Section 5.2 then combines the target scattering with propagation to obtain the TIER in different environments, because the propagation of sound into the seabed heavily depends on the seabed conditions. Section 5.3 subsequently discusses methodologies how to obtain the TIER including the effects of processing.

5.1 Target scattering

The amount of target scattering is an essential part in determining the target in environment response and depends on properties of both the target and the surrounding environment and on the used sonar pulse. The target scattering is determined by how the target oscillates as a result of an impinging acoustic pulse and by how these oscillations are radiated. Both can be described using structural acoustics [21].

The oscillations of an isotropic elastic solid due to an impinging load can be derived from the wave equation:

$$(C_{ijkl}u_{k,l})_{,j} + \omega^2 \rho_s u_i = F_i \tag{5.1}$$

where C denotes the elasticity tensor, u the displacement of the solid particles, ω the angular frequency, ρ_s the density of the solid and F the load on the solid. i, j, k, l are indices in the range $1,2,3$ for which the summation convention is used for repeated indices and $[]_{,j}$ represents differentiation in j.

For elastically isotropic materials the elasticity tensor simplifies and depends only on the Lamé parameters, μ and λ, which are related to the longitudinal and transverse sound speeds via:

$$V_{\mathrm{solid},L} = \sqrt{(\lambda + 2\mu)/\rho_s} \tag{5.2}$$

$$V_{\mathrm{solid},T} = \sqrt{\mu/\rho_s} \tag{5.3}$$

This means that the density and longitudinal and transverse sound speeds of each material are required to determine the target scattering. By using complex sound speeds this can be slightly extended to include damping as well. Together with the internal design, shape and size of the target these are the target properties that are relevant for determining target scattering. Note, that it is generally assumed that different materials in the target are assumed to be perfectly coupled meaning that there is continuity of displacement and stress across the interface. Naturally, the excitation of the target by the incident acoustic field also affects the scattering level. The incident acoustic field results from both the used sonar pulse (amplitude, frequency, aspect and elevation angle) and the propagation of the pulse from the sonar to the target as described in the section above.

The pressure in the surrounding fluid, Ω_f, as a result of the target oscillations is given by the Helmholtz wave equation, which describes the solid-fluid interaction:

$$\nabla \cdot \left(\frac{1}{\rho_f(\mathbf{x})} \nabla p(\mathbf{x}) \right) + \frac{k^2}{\rho_f(\mathbf{x})} p(\mathbf{x}) = 0, \quad \mathbf{x} = \Omega_f \tag{5.4}$$

where ρ_f denotes the fluid density, p the pressure in the fluid at position $\mathbf{x}$ and $k = \omega/c_f$ the wavenumber.

Note that it is assumed that the medium is treated as an unbounded fluid domain, where the Sommerfeld radiation criterium must hold at infinity. The variables that are of importance for the radiation part of the target follow directly from the Helmholtz equation and are the sound speed and density of the surrounding medium such as water, mud or sand.

To summarize, the target scattering strength depends on the following parameters:

- Incident acoustic field which results from a combination of the sonar pulse (amplitude, frequency, aspect and elevation angle) and environmental parameters that affect the propagation of the sonar pulse to the target (a.o. sound speed, range).
- Target properties: shape, size, internal design and densities and complex longitudinal and transverse sound speeds of each material.
- Properties of the surrounding medium: density and sound speed.
- Frequency

The effects of some of these parameters on the target strength can be quite severe as is demonstrated by several measurements [22][23]. Figure 5-1, for example, shows the TIER for three different targets, an aluminum UXO, a steel UXO and a solid steel artillery shell, measured in a fresh water pool [22][23] as a function of frequency and azimuthal angle. A clear variation with both frequency and azimuthal angle can be observed. Two elements that stand out are the high target response at broadside (90° and 270°) and the constructive and destructive interference effects at different frequencies. Furthermore, the influence of target properties becomes immediately clear when comparing all three TIERs.

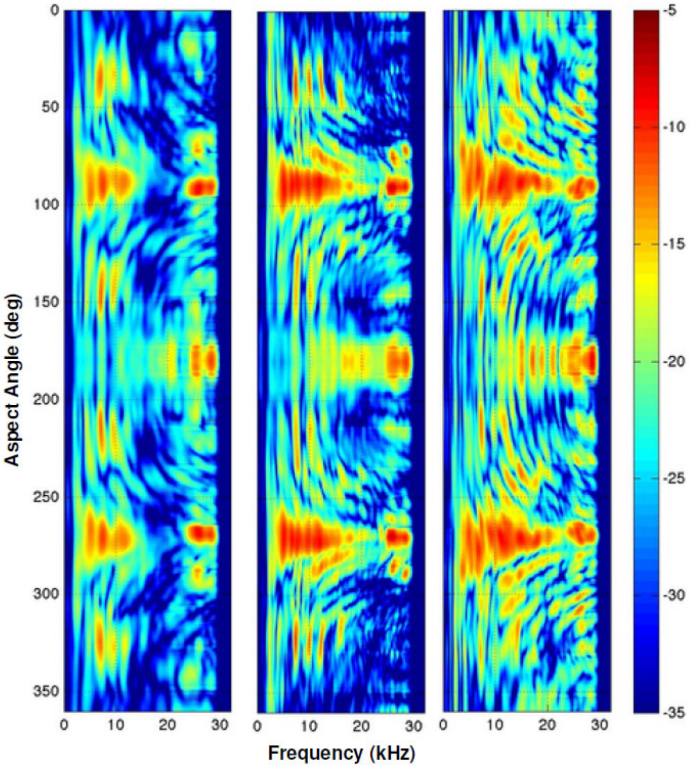

Figure 5-1: Measured target in environment response (TIER) as a function of frequency and aspect angle for an aluminum UXO (left), an steel UXO (middle) and a solid steel artillery shell (right). Here 90° and 270° represent broadside and 0° the nose of the target [21][23].

Another interesting possible effect on target scattering is the state of target. Bucaro et al. [2] measured two different targets after they had been exposed to severe biofouling and after a thin corrosion layer had formed. Figure 5-2 shows the effect of 16 weeks of biofouling on a 155 mm shell, which is filled with an epoxy resin. The TIER level is slightly lower for some frequencies and angles towards a maximum deviation of 5 dB. However, the main pattern of the acoustic color image remains the same after the target has been exposed to biofouling. The effects of corrosion (not shown here) have been measured as well. They do not influence the general pattern observed in the acoustic color of the object in the frequency band that is considered.

When looking at the operational use of TIER for coverage assessment, there are different ways to determine the target strength (TS) of relevant objects which vary in detail and computational demand. The first and easiest way to include the target response when searching for a specific object is to use an empirically derived target scattering level, which can possibly be a function of frequency as well. Secondly, the target of interest can be simplified to a shape for which an analytical solution is known such as sphere or a cylinder [24]. This requires a low level of computational power and variations with frequency and orientation can be taken into account. However, an amount of detail that can be essential for classification is lost due to simplification of the target. The third method for calculating TS is to use finite element modeling (FEM) to solve the wave and Helmholtz equations for a given incident acoustic wave and a given target. Most targets have a distinct TS pattern depending on frequency and aspect angle as presented in the figures in this section. With FEM these distinct patterns can significantly increase classification performances if data at sufficient frequencies and aspect angles is collected. There are two different flavors when using FEM to compute TS: 2.5D modelling of axisymmetric targets [25] and full 3D modeling [26]. Full 3D modeling has the obvious advantage that targets of any shape can be included, though at the cost of high computational cost. Selecting which method is the most relevant depends on the performance and time constraints of the operation. Naturally, the dependency of the TS computation, and thus of the coverage assessment, on the target properties changes with the selection of the TS method.

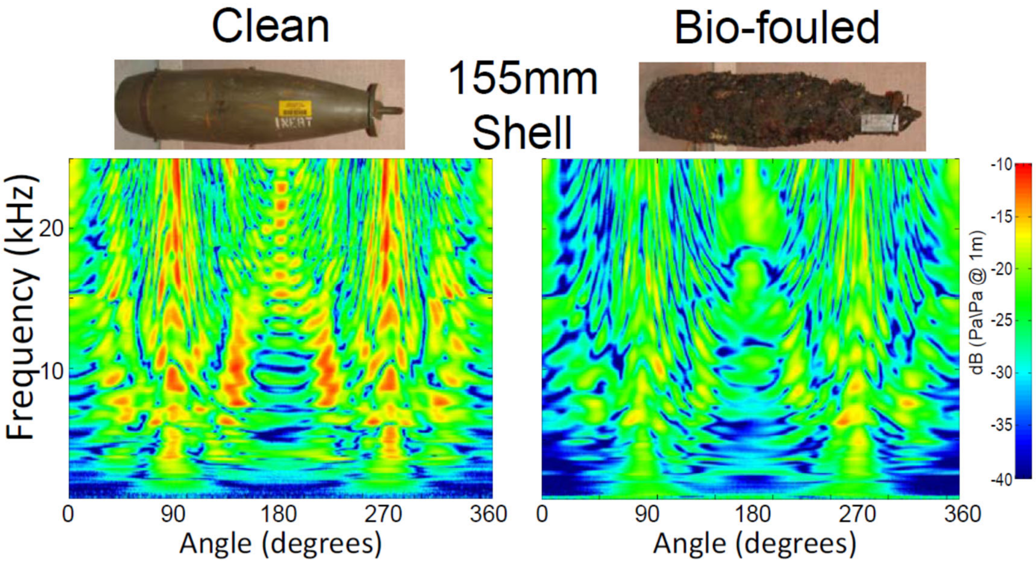

Figure 5-2: Measured target in environment response (TIER) for a clean (left) and bio-fouled (right) shell filled with epoxy resin [2].

5.2 Seabed conditions and target in environment response

The previous section primarily focus on the target scattering. To obtain TIER, the seabed conditions and the corresponding impact on TIER need to be considered as well. This will be discussed for three different scenarios with different seabed conditions (Figure 5-3):

1. A muddy seabed;
2. A sandy seabed:
3. A layered seabed.

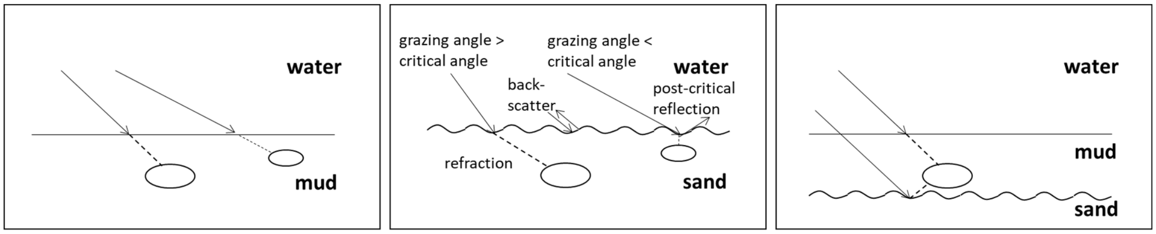

Figure 5-3: Cartoon illustrating mechanisms relevant to target in environment response for different seabed conditions: mudday, sandy and layered.

5.2.1 Target in environment response in muddy seabed

In a muddy seabed, the sediment predominantly consists of fine-grained sediment (silt, clay). Geoacoustic parameters that are commonly used as default values for these sediments, e.g. [18], indicate that the sound speed and density ratios between the sound speed in water and the compressional sound speed in the sediment is close to one. As a consequence, there is hardly a loss in the intensity at the water/mud interface and there is no critical angle of incidence. Volume scattering and absorption of sound in the sediment are important processes to consider for the coverage assessment, in addition to the target scattering response itself in a frequency band of interest.

For volume scattering, sound speed and absorption, large variability may be encountered in soft sediments due to the presence of gas bubbles. This occurs especially in the frequency range between 1.5 and 25 kHz in which gas bubbles are excited at resonance. The variability is attributed to the highly variable spatial distribution of bubble volume and bubble size distribution [27]. Using a through-the-sensor approach, it can be determined whether volume scattering is important. It is, however, much more difficult to estimate the corresponding effect on sound speed and absorption without conducting additional measurements based on the analysis of cores, which provide information only at specific locations.

5.2.2 Target in environment response in sandy seabed

A sandy seabed predominantly consists of coarser sediments compared to a muddy seabed. As a consequence, the sound speed and density ratios are larger, resulting in regimes with grazing angle above and below the critical angle of incidence. In both regimes, the detection of buried objects has been demonstrated [28].

For grazing angles above the critical angle of incidence, geoacoustic parameters are needed to estimate the transmission of sound into the seabed, the distance to be travelled within the sediment, and the absorption of sound in the sediment.

For grazing angles below the critical angle of incidence, information on sand ripple properties are required to make inferences on the detectability of a buried UXO object. The

SNR of the buried spheres observed at low grazing angles was reduced compared to the above-grazing angle detections [28].

5.2.3 Target in environment response in layered seabed

In a layered seabed, for example a seabed with a layer of fine sediments, with coarser sediments underneath, the TIER becomes more complex. When the impedance contrast between sediment layers is significant, such as in the examples as presented in Chapter 4, not only the direct path to the target needs to be taken into account, but also the paths that reflect at the interface between the different sediment layers, e.g. the mud/sand interface. This problem is also encountered for proud objects on the water/sand interface, and the effects have been thoroughly reported by Williams et al., [22]. Another complexity that may be encountered are higher-order TIER responses, in which more complex interactions between UXO object and sediment interface are taken into account [29].

To estimate TIER in a layered sediment, properties on sound speed and attenuation of the individual sediment layers need to be available.

5.3 Effect of processing

To assess the effect of processing on TIER, synthetic data can be generated for a variety of objects using one of the (potentially compute intensive) methods mentioned previously, after which the data can be put through the processing chain for evaluation.

A simple example of this is modeling a single track of synthetic data for a series of point scatterers. Note these are omnidirectional, so there is no amplitude variation with aspect and elevation angle. In the example, the scatterers are positioned in water (no sediment) at 10-15-20-25-30 m across-track distance and at a depth of 13 m. Subsequently, a generic volumetric SAS processing flow is applied including matched filtering. A depth slice and cross-line through the location of the objects are displayed in Figure 5-4. The effect of matched-filtering and acquisition angle (aperture) limitations can be assessed from the images.

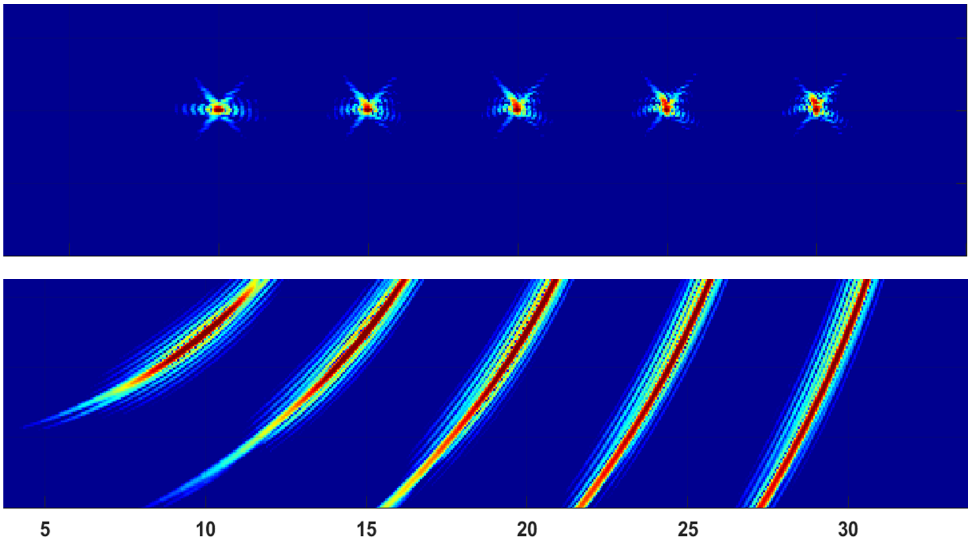

Figure 5-4: Depth slice (top) and cross-line (bottom) through the location of five point scatterers, after generic volumetric SAS processing.

The images presented in Figure 5-4 show that a generic sidelooking SAS system has a high-resolution in a horizontal plane, which means that individual scatterers can be resolved within a resolution cell [30]. There remains, however, an ambiguity in the vertical plane. The point scatterer response function shows that in this plane, individual scatterers cannot be fully resolved at larger across-track ranges.

This does not mean that the depth of scatterers cannot be determined. As indicated in Chapter 4, interferometric processing can be used to estimate the 3-D position of a scatterer. This requires, however, that a single scatterer is dominant in a specific range window.

Downlooking systems more easily achieve a higher depth resolution, because resolution is then mainly provided by the time resolution, and is further supported by the source and receiver beampattern.

6 Environmental response

The main terms in the sonar equation (3.2), which determine Signal Excess SE are the Target Echo Level TEL*, the Background Level BL*, and the Detection Threshold DT. The first and last terms are dealt with in Chapters 5 and 7, respectively. This Chapter focuses on the Background Level, including the Processing Gain.

‘Background’ is a collective term for all contributions to the received sound, caused by or influenced by the environment. Emitted signals have a specified frequency content and duration and are inherently shaped by transmitter characteristics. After transmission the signals propagate through the medium, traversing various paths, reflecting and scattering at any encountered surface or volume. Each of those interactions results in a loss of energy. At the receiver, the returning signal can be measured, influenced by all the aforementioned environmental interactions. Beside the actual signal to be measured, additional sound can be part of the received signal, caused by various external noise sources.

Four terms contributing to the total Background Level are dealt with below: reflection, reverberation, multipath contributions to reverberation, and noise.

6.1 Reflection

In downlooking mode, reflection from the seabed-sediment interface and interfaces between deeper sediment layers is dominant. The fraction of pressure from an incident wavefield reflected back is described by the reflection coefficient. It is dependent on the contrast in density and propagation velocity between the layers. For normal incidence, the reflection coefficient R is defined as follows ([31], Eq. VII-5a),

$$R = \frac{\rho_2 c_2 - \rho_1 c_1}{\rho_2 c_2 + \rho_1 c_1} \tag{6.1}$$

in which ρ is density and c is propagation velocity, and the subscripts 1 and 2 refer to upper and lower layer, respectively.

In sidelooking mode, the incident wavefield will arrive at an angle θ with respect to the layer normal. The angle-dependent reflection coefficient $R(\theta)$ is given by ([31], Eq. VII-9b),

$$R(\theta) = \frac{\rho_2 c_2 \cos\theta \; - \rho_1 \sqrt{c_1^2 - c_2^2 \sin^2\theta}}{\rho_2 c_2 \cos\theta + \rho_1 \sqrt{c_1^2 - c_2^2 \sin^2\theta}} \tag{6.2}$$

Note that this equation describes the specular reflection at the interface, not the non-specular backscatter that may occur at layer interfaces or within a layer. Also, wave conversion into different modes is neglected.

The reflected signal is a band-limited response; whether individual layers can be discerned depends on the center frequency and bandwidth. If dominant wavelength is defined as the distance between successive principal troughs of the wavelet, a common resolution criterium for minimum separation between layers is dominant wavelength divided by eight [32].

6.2 Reverberation

Emitted sonar signals interact with encountered volumes and surfaces. This leads to various forms of absorption, scattering and reflection. Ainslie defines reverberation as *"the sound originating from the sonar transmitter and subsequently scattered by underwater boundaries and obstacles other than the target, before arriving back at the receiver"* [18]. Hence, the sonar system not only receives responses from targets of interest during a survey, but also unwanted responses from the sea surface, the sea floor or the water column. All these interfering, undesired responses are called reverberation. Two types of reverberation are distinguished:

- surface reverberation, referring to sound scattering at a surface. In a layered shallow water environment, surfaces of interest are the top layer at the sea floor, a lower layer in the sea sediment, or the sea surface. The roughness of the surface (and the used frequency) plays a key role in the amount of surface reverberation.
- volume reverberation, which is caused by inhomogeneities in the medium. Suspended solid particles, air bubbles or marine life can contribute to the volume reverberation.

In a mud-sand layered environment, the main contributors to reverberation are fourfold: the scattering a the top layer of mud, volume scattering from the mud (due to heterogeneity), scattering from the surface of the sand below the mud, and volume scattering from the sand layer. Those are schematically shown in Figure 6-1. At low frequencies, the mud layer has a low impedance contrast compared to the mud/sand interface, and hence its contribution to reverberation is less prominent. Dominant scattering in LF-SAS originates from the mud-sand interface in contrast with HF-SAS and HF-SSS, as illustrated in Figure 4-2. At higher frequencies, absorption of sound in the mud layer becomes significant.

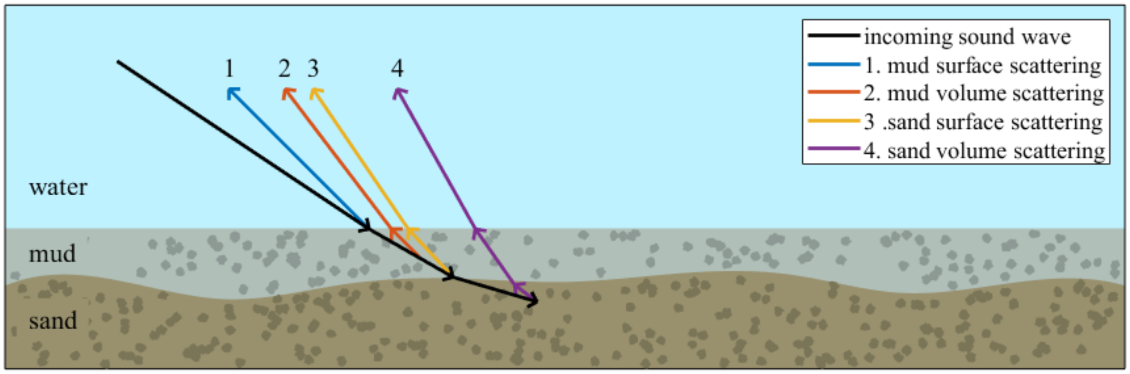

Figure 6-1: An overview of the main sources of reverberation due to scattering from layered volumes.

Although reverberation can be a nuisance in detection targets of interest, it also can be useful in remotely measuring the properties of the sea bed. In [19], a model of the sea floor is presented, where the sediment is treated as a fluid with a frequency-dependent effective density, and with volume heterogeneity included. The model is capable to deal with layers of mud and sand, and can predict surface and volume scattering effects, as shown in Figure 6-1. Williams provides a detailed model-data comparison, dealing with many unknowns. Ivakin presents a different modeling approach, which provides a fast first-order estimation of midfrequency (1-10 kHz) volume reverberation in complex shallow water environments [33].

Note that the contribution of the diverse scattering mechanisms is not the same at each given distance. The amount of sound penetrating into the mud and/or the sand layer is limited by the angle of incidence. Due to the velocity contrast, the angle of refraction can differ from the angle of incidence at the border of two media, following Snell's law

$$\frac{\sin\theta_2}{\sin\theta_1} = \frac{v_2}{v_1} \tag{6.3}$$

where θ_1 and θ_2 are the incident and refracting angle (w.r.t. to the normal), and v_1 and v_2 are the velocities in the first and second medium. When travelling to a medium with a higher velocity, there exists a critical angle $\theta_{c,2}$ at which the wave no longer couples into the second medium, but travels along the surface. Increasing the incidence angle results in total reflection. The critical angle is defined as

$$\theta_{c,2} = \sin^{-1}\frac{v_1}{v_2} \tag{6.4}$$

with the constraint that $v_2 > v_1$.

Figure 6-2 shows a few propagation paths, increasing the incidence angle from water to mud from 0° upwards. The critical angles of the mud/sand (2) and the water/mud (1) interfaces are shown in orange and purple, respectively. At incidence angles larger than those two critical angles, sound no longer penetrates into the sand, or even into the mud, respectively. This implies that buried objects at ranges corresponding to those incidence angles, are no longer ensonified, and hence cannot be detected. Critical angles have also been dealt with in Section 5.2.

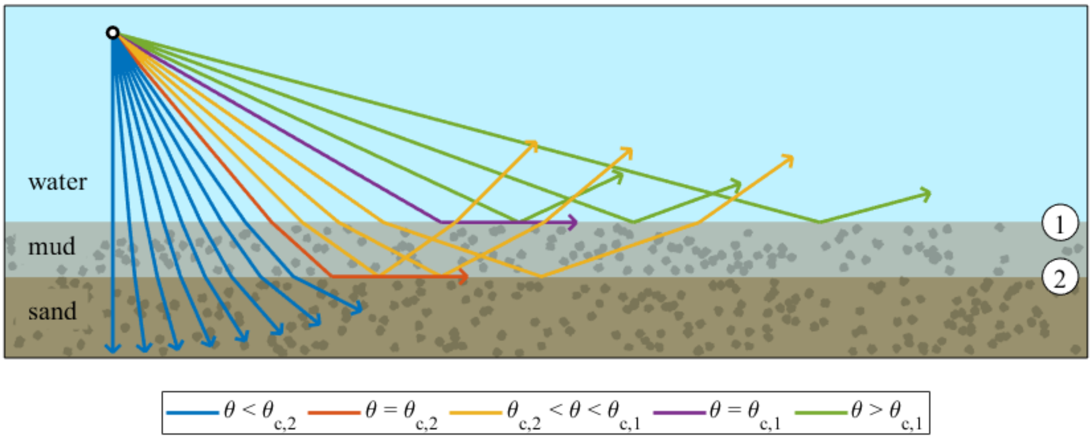

Figure 6-2: An overview propagation paths as function of incidence angle, with the two relevant interfaces water-mud (1) and mud-sand (2).

6.3 Multipath

The performance of sonar systems in relatively shallow water is limited by the effects of multipath interference. The recorded signal is not only the response of the direct path (source – bottom – receiver), but contains also signals due to various reflections and scattering at the water surface and sea bottom. As a result, the incoming waves interfere with each other, degrading the quality of the resulting image. The effects of multipath can be observed in sonar imagery as 'ghosts', and as a decrease in image contrast (shadows are filled in) [20][34]. Other types of sonar data processing also suffer from image degradation due to multipath, as interferometric imaging, due to a lower spatial coherence, leading to lower quality bathymetries [30][34][35], and Synthetic Aperture Sonar (SAS) processing, due to a decrease in the correlation of pings (in other words, with a lower temporal coherence) needed for estimating the platform's micronavigation [36][37][38].

As an example, a series of 7 paths with an identical path length (here eight times the water depth) is shown in Figure 6-3. Only those paths are shown which arrive at the receiver from the sea floor (i.e. below the horizontal line). Each path is labelled in accordance with the encountered reflection or scattering. A 'B' means a non-specular scattering at the bottom, a 'b' means a specular reflection at the bottom; similarly the 'S' and 's' stand for a non-specular scattering and specular reflection at the surface, respectively. Note that the paths 'bsB' and 'Bsb' coincide, but with a different wave travel direction, and hence a different arrival angle. In sonar processing, all those contributions with the same travel time add up, and are mapped at a position corresponding with the direct path.

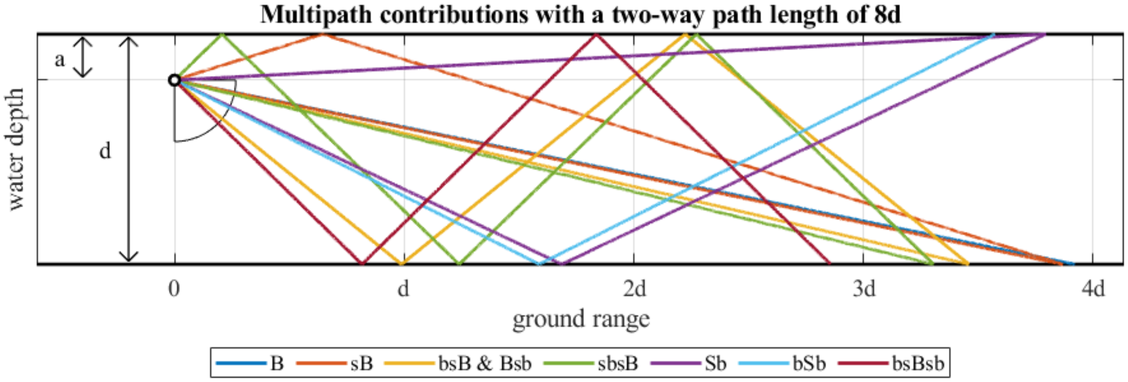

Figure 6-3: The wave paths of the main multipath contributors, with the same two-way path length. Only those paths are shown which are incoming from below the receiver (denoted by the circle quadrant). The variables 'a' and 'd' represent the source/receiver depth and water depth, respectively. Labels are explained in the text of Section 6.3.

The influence of multipath increases with range, which is illustrated in Figure 6-4. This figure shows the arrival angles (w.r.t. the horizontal plane) of the incoming waves. For slant ranges below the altitude of the source/receiver, obviously no bottom signal can be obtained. Up to double the water depth minus the source depth, three paths can be present ('B', 'sB' and 'Sb'). Note that the latter two are caused by a source signal that travels upward from the source towards the surface. Proper shaping of the source beam pattern and orientation can reduce those paths, and hence mitigate their corresponding multipath effects. After double the water depth, four additional paths can be present ('bsB', 'bSb', 'Bsb' and 'sbsB'). Appropriate beamforming can reduce the influence of some of those paths, but as can be seen in Figure 6-3 and Figure 6-4 (around a slant range of 4 times water depth), the arrival angles of the incoming 'B', 'sB', 'bsB', and 'sbsB' are almost indistinguishable.

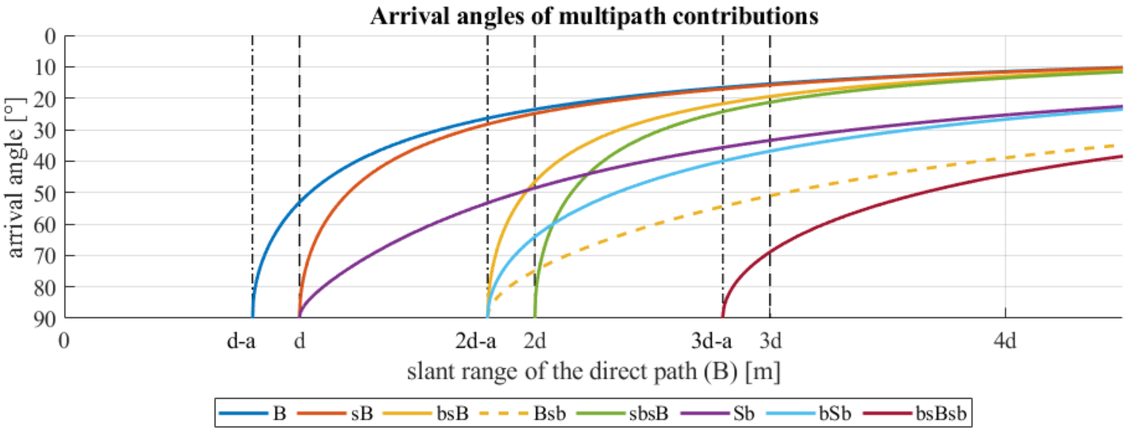

Figure 6-4: The arrival angles of the same contributors as in Figure 6-3, as function of the slant range of the direct path. The variables 'a' and 'd' represent the source/receiver depth and water depth, respectively. Labels are explained in the text of Section 6.3.

The influence of multipath on the sonar imaging depends on several factors:

- **Water depth.** This is one of the primary factors which influences the occurrence of multipath. Shallow water leads to a short range without multipath echoes, as can be seen in Figure 6-4. The most contributing multipath echoes (second-order 'bsB', 'bSb' and 'Bsb') can be found at ranges larger than twice the water depth [20].
- **Sea state and weather.** All multipath echoes contain at least one (non-)specular reflection at the water surface. A rough surface leads to a more dampened and smoothened scattering effect. However, the impact of specular reflections is increased when the sea surface acts as a mirror, that is, when the surface is smooth and flat. Scattering and reflection at the sea surface is worst at windless weather conditions or very low sea states, as illustrated in Figure 6-5 for a high-frequency SAS image.
- **Sediment properties.** The scattering at the sea bottom affects not only the direct echo, but also the higher-order multipath signals contain scattering and/or reflections from the sea floor.

6.4 Noise

In addition to source-generated noise (reflection, reverberation, multipath), other noise sources not related to the active sonar transmission may have to be considered as well in coverage assessment. It includes ambient noise, electronic noise, flow noise, shipping noise (engines).

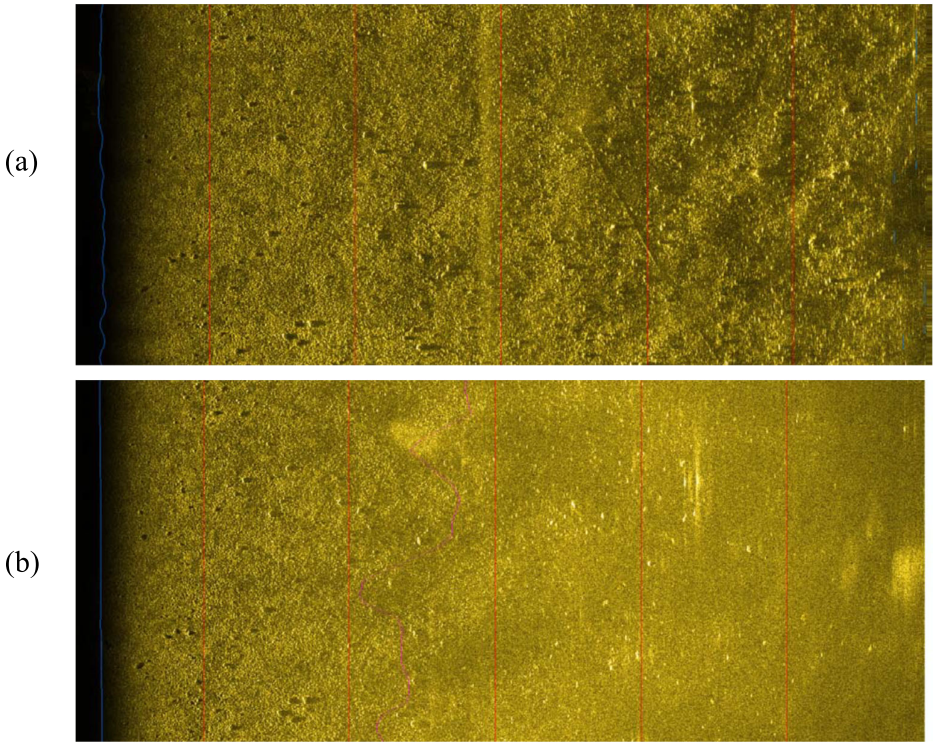

Figure 6-5: An example of two SAS images of the same area and with the same settings, only taken in different wind conditions: wind speed of (a) 13 m/s and (b) 4 m/s. Source: [20]

7 Signal-to-background ratio and detection threshold

The difference between TIER of simulation results, in which the effect of processing is taken into account, and the measured background response yields an estimate for the signal-to-background ratio (SBR), which is also often referred to as the signal-to-noise ratio (SNR), for an object of interest.

The TIER examples presented in Chapter 5 show that the target strength of UXO objects generally has significant variations with frequency and with aspect angle and target orientation. To make inferences on the detectability of these objects, this variability needs to be taken into account.

- The procedure to take variability with frequency into account depends on the detector that is used. When a detector, such as an energy detector, operates in the entire frequency band, the variability with frequency is not explicitly taken into account in the detection process. A sub-band detector, on the other hand, in which detection is considered in individual frequency bands independently, is a natural procedure to take variability with frequency into account. Individual sub-bands should be chosen such that matched filter gain is sufficient for mitigating reverberation and noise.
- Different target orientations and illumination from specific directions – it is assumed that straight tracks are sailed in an UXO detection survey, which means that a limited range of aspect angles are covered – result in differences in the observed target echo level. To assess the detectability of an UXO object at a specific location, different UXO orientations and illumination therefore have to be considered.

According to the definition of the detection threshold DT, it is the SBR at which a probability of detection of 0.5 is achieved at an acceptable false positive rate. In addition to the variability in TIER, the background needs to be considered as well to establish a DT. In areas with variability in the background response, as in Figure 7-1, it is first required to segment the area into different regions. In the example presented below, the DT in segment I will be lower than in segment II, because, at a certain threshold, the number of contacts in area I will be lower compared to the number of contacts in segment II.

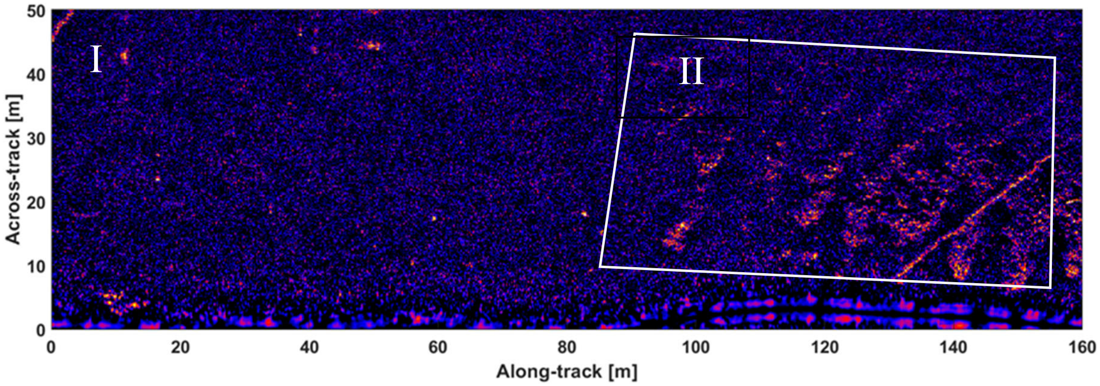

Figure 7-1: Example of LF-SAS image with variability in the background. The image is divided in two segments with different background statistics, and consequently a different detection threshold.

In downlooking configurations, reflections at the seabed and sub-surface layers can introduce large intensity variations. Image processing techniques to suppress the reflections and dynamic gain corrections are commonly used as pre-processing prior to the detection [6]. The potential of these techniques should be included process of assessing the detectability of buried objects, and thus in the coverage assessment for buried object sonar systems that operate in a downlooking configuration.

8 Environmental assessment

8.1 Introduction

8.1.1 Problem statement

To illustrate the need for environmental information as input to coverage assessment, an example is provided from an experiment conducted near Gdynia in Poland. In the data example provided, the TIER of two identical scientific cylinders, referred to as NL-REF, is considered. One of the deployed objects was proud, the second one was buried in sandy sediment at approximately 0.3 m depth. LF-SAS images for the proud and buried objects are presented in Figure 8-2, the corresponding maximum signal-to-reverberation ratio in Figure 8-3.

The following can be observed:

1) For the proud object, the SRR increases with across-track range, whereas the buried object cannot be detected at long ranges. An explanation for the increased SRR for the proud object is that the backscattering strength of the sediment decreases with grazing angle. The buried object cannot be detected when the grazing angle becomes smaller than the critical grazing angle.

Figure 8-1: Photograph of NL-REF targets.

Proud reference cylinder

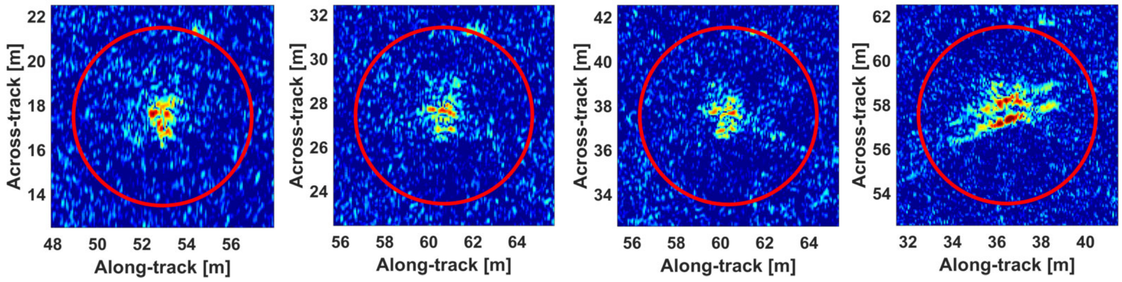

Reference cylinder at 0.3 m depth

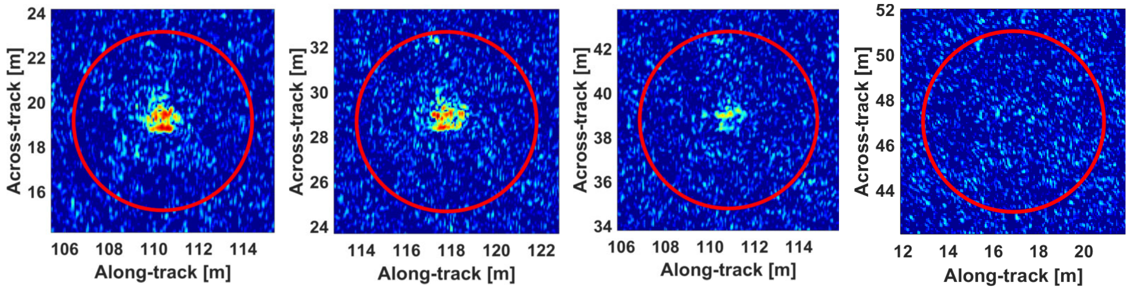

Figure 8-2: Example of LF-SAS images for a proud object (NL-REF) and the same object buried at 0.3 m depth. The vertical axis shows the across-track range, respectively 18, 28, 38 and 58 meter for the proud cylinder, and 19, 29, 39 and 47 meter for the buried cylinder.

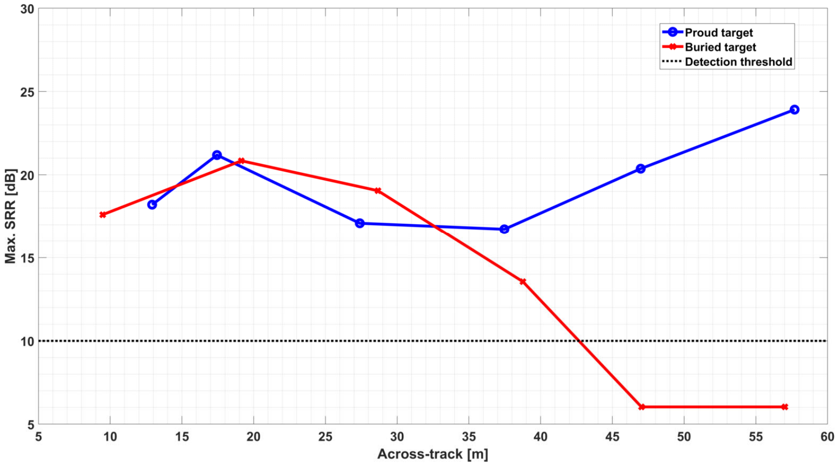

Figure 8-3: Maximum SRR for the proud and buried objects shown in Figure 8-2.

2) For the proud object, the TIER itself does not show significant variability with across-track range between different runs, except the image corresponding to the longest range. This difference is caused by some defocusing in the LF-SAS imaging.
3) For the buried object, the intensity of the TIER reduces with range. This is attributed to the longer path length of the sound in the sediment and the corresponding increased absorption.

This example illustrates that the acoustic seabed conditions have a large impact on the performance on the detection performance against buried UXO vs range. Beyond the critical angle, the data do not provide any indication that a buried UXO object is present. As a consequence, information on the acoustic seabed properties is considered as essential input for the assessment of UXO detection surveys. The goal of this section therefore is to identify acoustic seabed classification techniques that can be used to determine the relevant acoustic seabed properties to enable coverage assessment.

8.1.2 Research questions

It is anticipated that an acoustic system designed to be capable to detect and localize buried UXO objects also has capabilities to collect information on geoacoustic seabed properties. This has several benefits:

(i) Information on geoacoustic seabed properties is then obtained in the entire survey area.

(ii) No additional data acquisition efforts (and time) would be required to collect the environmental information.

The research question therefore is:

> Can relevant information on acoustic seabed properties be obtained from LF-SAS data, including data from supporting sensors, and if so, how? If not, are there suitable alternatives?

8.1.3 Approach

To address the research questions, this section is organized as follows. Section 8.2 reviews literature on acoustic seabed classification. Section 8.3 investigates which information on acoustic seabed parameters can be obtained using a downlooking configuration. Section 8.4 discusses whether information on acoustic seabed properties can be obtained from data acquired in a sidelooking configuration. Conclusions on acoustic seabed classification are drawn in Section 8.5

8.2 Literature review on acoustic seabed characterization

A wide variety of techniques exist to obtain information on acoustic seabed properties, often related to seabed classification [41][42][43]. Important parameters in the characterization of seabed sediments are the composition (grain size, density), the geometry (layer thickness, surface roughness), the sound speed (compressional, shear), and the sound absorption. These environmental parameters are important to determine parameters which quantify the sonar performance, e.g. the acoustic backscatter strength, critical angle and attenuation. When information on sediment properties, such as grain size or composition, is measured, it is common to use empirical relationships to make inferences on the corresponding acoustic properties [18]. However, significant uncertainties remain in these relationships, because naturally occurring sediments are always composed of different grain sizes, and porosity may differ as well.

Since most muddy sediments have very low shear speeds, they can be considered as fluid media. To characterize the behavior of the acoustic wave in a fluid medium, the plane wave reflection coefficient $R(\theta)$ is of main importance. This reflection coefficient depends on the sediment density ρ_{sed} and sound speed c_{sed} (combined in the acoustic impedance), and the attenuation coefficient α_{sed} [18].

Sound speed, density and attenuation are also strongly correlated with the sediment's grain size. Empirical relations (third-order polynomials) for those parameters have been determined for various grain sizes, valid for frequencies above 10 kHz, and in the top few centimeters of the sediment layer. Those are listed in [18] (Table 4.17). Since the attenuation is approximately proportional to the frequency, the attenuation coefficient in terms of dB per wavelength β_{sed} can be computed as

$$\beta_{\mathrm{sed}} = 20\log_{10}\left(\exp\left(\alpha_{\mathrm{sed}}\frac{c_{\mathrm{sed}}}{f}\right)\right) \tag{8.1}$$

where α_{sed} is the attenuation in Np per meter, c_{sed} is the sound speed and f is the frequency. The dimensionless term in the exponent can be regarded as the amount of attenuation per wavelength. Ainslie explains this as follows *"Despite appearances, the symbols* "Np/λ" *and* "dB/λ" *both represent dimensionless units. This can be confirmed by inspection of Equation (8.1), the right-hand side of which is dimensionless. Therefore, so too must be the left-hand side. The paradox is resolved by realizing that the notation* 'dB/λ' *is used as shorthand for a decibel per wavelength which is the same as a decibel per meter multiplied by the wavelength in meters. In other words* 1 "dB/λ" $= \lambda \times 1$ dB/m*, which is dimensionless"* [18](Section 4.4.1.3, footnote 27).

For lower frequencies, roughly between 1 and 10kHz, bulk geoacoustic parameters have been derived, representing the top few meters of the sediment. Sound speed and density are polynomial functions as function of grain size, and are also listed in [18] (Table 4.18). Since the attenuation coefficient β_{sed} is approximately independent of the frequency, it can be scaled using only the sound speed.

The uncertainties of the sound speed and density estimations are in the order of 1.5% and 7.5% respectively, and the attenuation coefficient uncertainties are one order of a magnitude higher [18].

The critical angle θ_{crit} at the interface between water and sediment, is defined as

$$\theta_{\mathrm{crit}} = \cos^{-1}\left(\frac{c_{\mathrm{w}}}{c_{\mathrm{sed}}}\right) \tag{8.2}$$

where c_{w} and c_{sed} are the sound speeds in the water and sediment, respectively. At grazing angles smaller than this angle, total reflection occurs, meaning that all sound is reflected and nothing penetrates into the sediment. Effectively, this means that when the grazing angle becomes too small (i.e. increased ranges at fixed altitude), buried objects cannot be detected anymore, since they will not be ensonified. This has been described in Section 8.1, and illustrated in Figure 8-2 and Figure 8-3, where the buried object 'disappears' at larger ranges. This proves the importance of knowing the critical angle by measuring the underlying sound speeds, since this critical angle determines the maximum observation range. Note that if the sediment consists of multiple layers, a different critical angle exists between each distinct layer.

Some of the relevant environmental parameters can be obtained by in-situ measurements, others require remote sensing methods [44]. An example of an experiment in which a multitude of methods has been applied is the SeaBed Characterization Experiment (SBCEX), which took place in an area called the New England Mud Patch in 2017. The experiment focused on understanding the underlying physics, quantifying estimation uncertainties, correlating observations and measurements, and assessing the performance of geoacoustic models [45].

In general, in-situ measurements from a limited number of sample points (taking grab samples or sediment cores or by diver inspection) offer the best opportunity for accurate information. The samples provide information on the sediment composition (grain size) and geometry (thickness, layering), and the measurement systems can be used to obtain sediment sound speed profiles as well [46][47]. However, these methods are time consuming, require a lot of effort, and ultimately provide information which is only accurate in a limited area around the sample points. Especially in environments with much spatial or temporal variability, using only in-situ measurements might be insufficient for a good characterization.

Remote sensing methods are a way to obtain seabed information on a larger scale in any environment. Those type of techniques are commonly used for geoacoustic inversion, where measurement data is used to estimate the parameters of an underlying model of the water column and sediment. The majority of geoacoustic inversion techniques use data acquired in a bistatic geometry as input, and provide information on sediment layering [48]-[53], sediment density [50]-[52][54], water column and (depth- and frequency-dependent) sediment sound speed [50]-[56], and sediment attenuation [51][52][55].

Through-the-sensor systems are a subset of remote sensing systems. This type of system utilizes the same data collected for specific tasks (e.g. detection) to also characterize the environment, with the benefits that there is no temporal or spatial difference, and that no additional sensors are required. As a consequence, this type of systems contains mostly monostatic systems, e.g. sub-bottom profilers (SBP), single beam echosounders (SBES), multibeam echosounders (MBES) or sidescan sonars (SSS).

Echosounders are downlooking systems based on analyzing the backscattered signal from the seabed. Sonar backscatter depends on the used acoustic frequency, the angle of incidence on the seabed and the geoacoustical and physical properties of the seabed. The magnitude and shape of reflected echoes from the water-sediment interface provide information on the sediment itself. Parameters which can be derived from the echoes are surface hardness and roughness, depending on the angle of incidence. Statistical and empirical models are used to perform the geoacoustic inversion ant to classify responses and thus characterize the seabed [57][58]. Hence, sub-bottom profilers [59][60], single beam echosounders [61][62], multibeam echosounders [63][64][65], and other types of echosounders [66] can be used for classification of the seabed. Although echosounder methods are capable in characterizing and classifying different types of sediment, this is only a distinction in terms of their acoustic signature. Assigning a physical meaning to the obtained sediment classes, leading to identification of individual sediment types, requires a validation with ground truth, i.e. in-situ data from grab samples or gravity cores [44][57][58][61].

Sidelooking sidescan sonar systems are often used for seabed mapping, especially when operating at higher frequencies. At lower frequencies, those systems can also be used for sediment characterization. However, compared to downlooking systems, these systems provide much more complex data, prone to multipath effects, scattering effects due to the more shallow angle of incidence, and reflection due to exceedance of the critical angle. Interpretation of sidescan data for environmental assessment and characterization is more challenging than for downlooking systems.

Since in-situ measurements require large efforts, providing accurate but spatially limited information, these are less suitable as a primary source for obtaining data for seabed characterization. However, they are invaluable for calibration and verification purposes.

Remote sensing methods for bistatic geoacoustic inversion require well-separated source and receiver systems, a thorough scheme of measurements and sophisticated models in order to obtain sufficiently accurate data in an environment. Geoacoustic inversion is a topic on its own, focusing on the development of robust inversion methods, dealing with numerous inferences and uncertainties while avoiding nonuniqueness in the solutions. At the moment, those methods are less suitable for our desired operational approach.

In the next sections, it is explored whether information on relevant acoustic sediment properties that are required for coverage assessment can be directly obtained using data acquired with an UXO detection systems. Such an approach would be of interest, since this would not require additional data acquisition time, and information on acoustic seabed properties would then become available in the entire survey area.

8.3 Downlooking geometry for acoustic seabed classification

A downlooking geometry is provided for by a downlooking sonar configuration, or by using a sub-bottom profiler as an auxiliary sensor.

8.3.1 Sub-bottom profiling – layering & impedance contrast

In the downlooking direction, sound waves travel predominantly perpendicular to the layering in the seabed. Hence the downlooking image offers the best resolution in the depth direction. Figure 8-4 gives an example of such an image. At around 10.6 m depth a reflection interpreted as the water/mud interface is visible, and at 11.4 m a reflection of the mud/sand interface. A slight decrease in layer thickness occurs of the mud with increasing along-track.

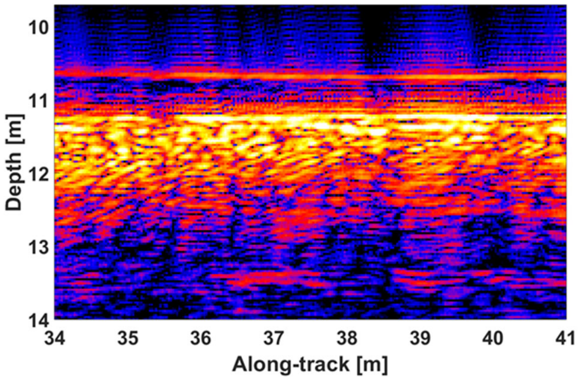

Figure 8-4: Downlooking image below the sonar, obtained with the upper band of the MUD LF-SAS system, acquired in the Haringvliet environment. Layering of the seabed can be recognized, with a mud layer roughly between 10.6 and 11.4 m depth. The backscattering strength increases in the sand layer.

Amplitude variation of the reflector is related to change of contrast in impedance (the product of speed of sound and density), according to Eq. (6.1). It can be seen that the mud/sand interface is much brighter than the water/mud interface, from which it follows that the impedance contrast between water and mud is not so strong as that between mud and sand. Also, lateral variations in reflection strength are visible, suggesting slight changes of sediment properties along-track. It is, however, difficult to extract information on sediment sound speed directly from the impedance contrast, because the density contrast dominates the impedance contrast. A common approach therefore is to first characterize the sediment type, and subsequently use empirical relations to make inferences on the sediment sound speed. For this approach, it is common to use systems with a smaller opening angle, such as a single beam or multi-beam echo sounders (SBES/MBES), as discussed in the previous section.

In this section, it is explored whether information on sediment sound speed can be inferred from diffractors.

8.3.2 Sub-bottom profiling – diffraction

Diffractions are the seismic response of small, but structurally relevant, elements in the subsurface, like small near surface scattering objects, or small scale faults, in general all objects which are small compared to the seismic wavelength. Arrival times of diffractions from objects buried into the sediment carry information about the sediment speed of sound. In for example [39], this property is used in a sub-bottom-profiler-like geometry to estimate sediment velocities in the deeper subsurface. In a shallow marine environment however, the majority of the propagation path of diffractions is spent in the water column. To investigate the potential of this technique in such an environment, first a simple 2D finite difference modeling was performed to obtain the response of a diffractor buried 0.4 m under a water-sand interface. Dominant frequency of the source pulse is 4 kHz, similar to the MUD system. Receivers were placed in the water half-space 8 m above the sand interface.

Figure 8-5 (a) and (b) show the response at the receivers for sand with a compressional velocity of 1700 m/s and shear velocity of 500 m/s, and for 2000 m/s and 700 m/s, respectively. The dashed line indicates the arrival time if there is only water, aligned to the peak of the event at point of closest approach. Displays after flattening on the water arrival time are shown in (c) and (d). The arrival time difference builds with distance from the diffractor and with the velocity contrast. Also there is a small change of arrival time at the point of closest approach. Applying a monostatic imaging algorithm with a series of different sediment velocities, and observing the focusing of the imaged diffraction point could reveal the optimal sediment velocity.

Figure 8-6 shows a field record with a diffraction of a buried object with known depth. The dashed line shows the arrival time based on only water velocities. The signal-to-noise makes it difficult to assess arrival time difference especially in the tails farther away from the diffractor, which are expected to be most sensitive to the sediment velocity. Moreover, the object may exhibit oscillations which may make it difficult to pick the location of the first cycle. The effect of sediment on arrival time would be larger for objects buried deeper, however for those the diffraction tails will be attenuated more quickly. Unfortunately in the field data most of the diffractions with clear tails are from non-buried scatterers. Therefore it was not considered opportune to investigate this method further.

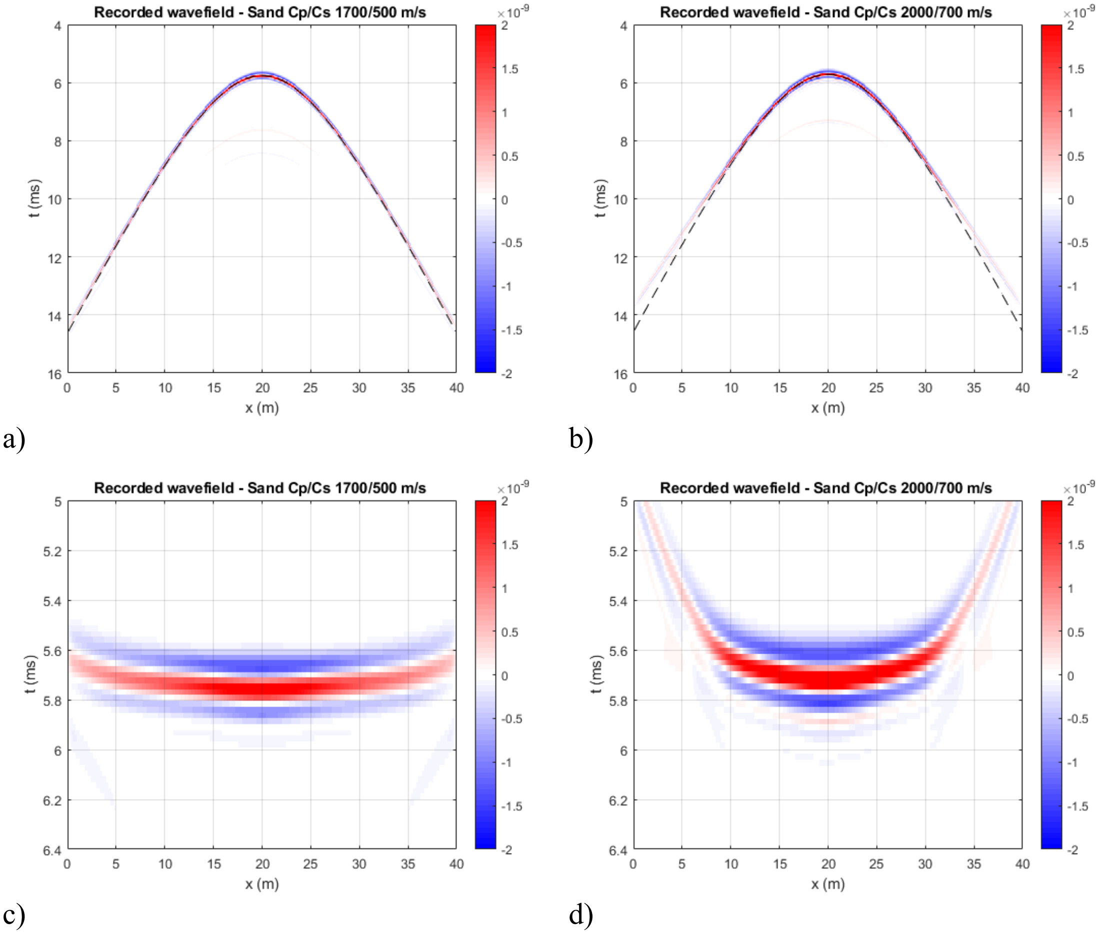

Figure 8-5: Simulated recordings for a diffractor buried in sand with a low (a) and fast velocity (b), water arrival time snapped to peak shown with dashed line. Figures (c) and (d) are after flattening on water arrival time.

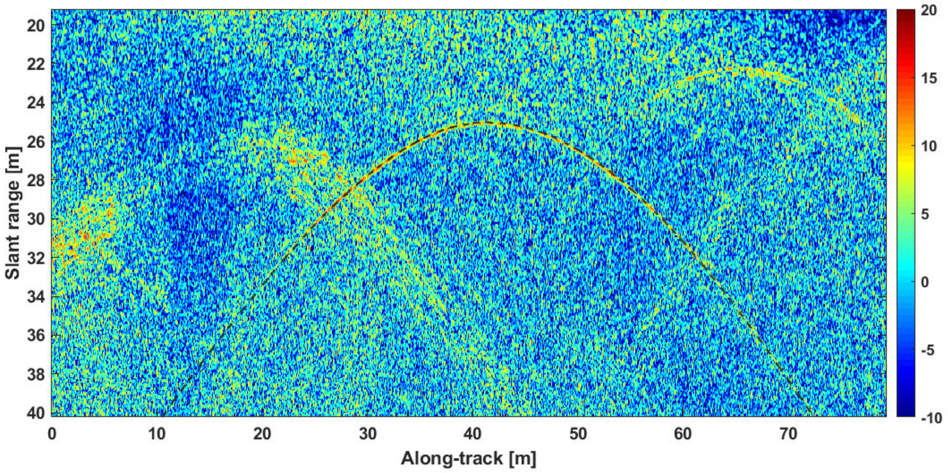

Figure 8-6: Example from field data of a diffraction of a buried object.

8.4 Sidelooking geometry for acoustic seabed classification

This section explores whether acoustic seabed parameters can be derived from multi-band backscattering measurements. It would be rather beneficial if this information can be obtained using the same system as used for the detection of buried UXO. Then, no additional measurements would be required to support the coverage assessment. It is, however, not straightforward to relate backscattering to acoustic seabed properties such as sound speed and attenuation, because interface roughness and inhomogeneities are the main contributors to backscattering. Based on observations in data acquired by the MUD system, introduced in Chapter 4, a concept has been developed to estimate the attenuation coefficient in a soft sediment layer. This concept will be developed and discussed in this section.

Sediment sound speed and attenuation are important parameters for the coverage assessment. While sediment sound speed can be reliably inferred from information on the grain size of the seabed sediment, which is commonly available a priori or which could be derived from SBES/MBES acoustic seabed classification techniques, there are larger uncertainties in the sediment attenuation [18]. An additional complexity is that it is difficult to obtain reliable estimates of the attenuation of sound in seabed sediments without conducting dedicated measurements, either using in-situ recordings or wide-angle reflection survey data [47].

In this section, the feasibility of a through-the-sensor concept is explored to retrieve information on sediment attenuation, i.e. whether information on sediment attenuation can be derived from wideband back-scattering measurements.

The idea originated from observations in back-scattering data in the Haringvliet estuary and Gdynia environments:

- The Haringvliet site has a layered sediment. The seabed consists of a mud layer with sand underneath. As reported in Chapter 4, the backscattering mechanisms vary with frequency. At high frequencies (> 100 kHz), sound does hardly penetrate into the seabed due to the high attenuation, and dominant scattering consequently occurs at the water/mud interface. At frequencies below 30 kHz, the mud layer appears to be acoustically transparent, resulting in dominant scattering at the mud/sand interface. This is confirmed by the interferometric height estimates. Water depth is around 10 m.
- The Gdynia site has a sandy seabed. The water depth is larger compared to the Haringvliet, 23 m.

For these two environments, Figure 8-7 presents normalized back-scattering strength (BSS) versus slant range for different frequency bands below 30 kHz. The curves have been compensated for geometrical spreading loss. Figure 8-7 reveals that there are significant differences in BSS vs range between Gdynia and Haringvliet. For Gdynia, the BSS vs range shows a similar trend for all frequency bands, whereas there are significant differences in the BSS in the Haringvliet environment. In the Haringvliet environment:

- the BSS slowly decreases with slant range for two upper bands (Band 3 and Band 4), whereas the BSS decreases more rapidly with slant range at the lower frequencies, especially for the lowest band.
- The graph suggests that there is a transition in Band 2 from the rapid decrease at short ranges to the slower decrease at larger slant ranges.

- Note furthermore that backscattering at slant ranges beyond 22 m does not only contain direct-path contributions, but also paths that interfere with the sea surface. This explains the increase in normalized BSS at the larger slant ranges.

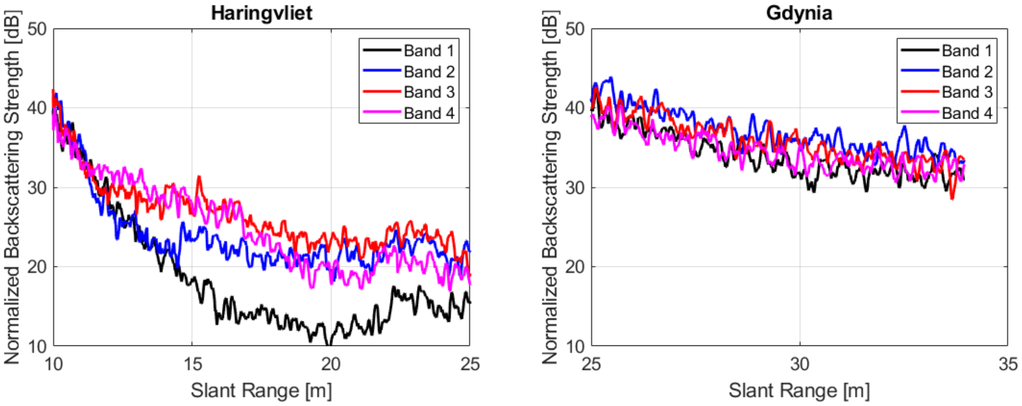

Figure 8-7: Normalized backscattering vs slant range for different sub-bands for the Haringvliet (left) and Gdynia (right) sites.

Ignoring multipath contributions, it is anticipated that there are two mechanisms that influence the change in BSS with slant range in the Haringvliet environment:

1) The interface BSS varies with grazing angle. The general trend is that the BSS decreases with grazing angle
2) The BSS of the sub-surface interface also varies with slant range due to an increased path length in the sediment. Due to attenuation of sound in the sediment, this results in an increased sediment transmission loss $\mathrm{TL_s}$.

Assuming that refraction can be neglected in the mud layer, The change in BSS due to attenuation in the sediment can be expressed in terms of a transmission loss:

$$\mathrm{TL_s} = \frac{2R_s\alpha_s}{\lambda} = \frac{2}{\lambda}\frac{H_s}{(H_w+H_s)}\alpha_s R, \tag{8.3}$$

with R the slant range; R_s the path length travelled in the sediment layer; H_s the thickness of the sediment layer; H_w the height of the water column below the sonar; λ the wavelength, and α_s the attenuation of sound in the sediment, expressed in dB/λ. The corresponding trend with slant range caused by sediment attenuation is:

$$\frac{\mathrm{dTL_s}}{\mathrm{d}R} = \frac{2}{\lambda}\frac{H_s}{(H_w+H_s)}\alpha_s. \tag{8.4}$$

Consequently, sediment attenuation can be expressed as:

$$\alpha_s = \frac{(H_w+H_s)}{H_s}\frac{\lambda}{2}\frac{\mathrm{dTL_s}}{\mathrm{d}R}. \tag{8.5}$$

The remaining question now is how to obtain the variation in the sediment transmission loss.

Figure 8-8 shows again the Haringvliet BSS vs slant range, with linear curves fitted through the BSS data vs range. The steep curves follow the short-range trend in BSS of the two lower bands. It is hypothesized that the dominant scattering at these frequencies corresponds to the sub-surface interface. According to this interpretation, the curves contain both the changes in interface scattering and transmission loss in the sediment vs slant range. At larger slant ranges, the decay in BSS vs range follows the same trend as observed in Band 3. Our current interpretation is that at larger ranges and higher frequencies, the interface scattering at the water/mud interface becomes dominant.

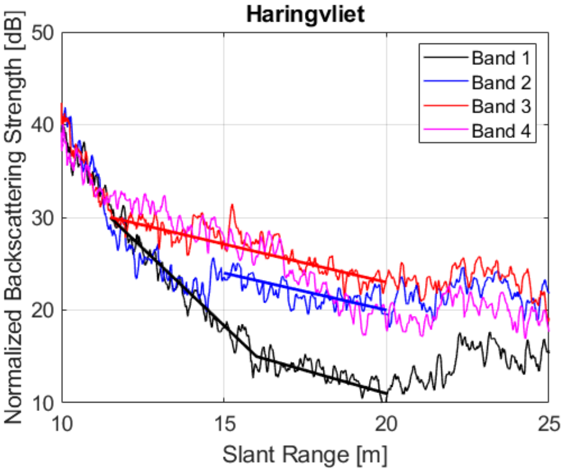

Figure 8-8: Normalized backscattering vs slant range for the Haringvliet site, with curve fits superimposed. The steep curves are interpreted to correspond to the BSS from the sub-surface interface. The smaller decay with slant range is related to the interface scattering at the water/mud interface. At slant ranges beyond 20 m, the interpretation of the data becomes increasingly complex due to multipath contributions.

Assuming that the trend in interface scattering vs slant range is similar for the seabed and the sub-surface interface – which is a fair assumption because the main variations with range are introduced by the change in the grazing angle – it is possible to separate the subsurface interface scattering term from the sediment transmission loss:

$$\frac{\mathrm{dTL_s}}{\mathrm{d}R} = -\left[\left(\frac{\mathrm{dBSS}}{\mathrm{d}R}\right)_A - \left(\frac{\mathrm{dBSS}}{\mathrm{d}R}\right)_B\right] \tag{8.6}$$

Where the subscript A corresponds to the linear curve with fast decay with range due to sub-surface interface scattering and transmission loss in the sediment, and the subscript B corresponds to the linear curve interpreted to correspond to interface scattering at the water/mud interface only.

Based on the straight line fits in Figure 8-8, $\mathrm{dTL_s}/\mathrm{d}R = 2.3$; using $\lambda = 0.125$ m; $H_w = 10$ m; $H_s = 1$ m, this results in the following estimate for the sediment attenuation: $\alpha_s = 1.6$ dB/λ. This value is compared to empirical values which list the attenuation coefficient for different representative grain sizes [18] (Figure 8-9). This comparison reveals that the estimated attenuation coefficient is high. Ainslie, 2010 [18] also reports significant uncertainties in the attenuation coefficient vs grain size, because attenuation heavily depends on the porosity of sediments and the presence of (resonating) bubbles [27].

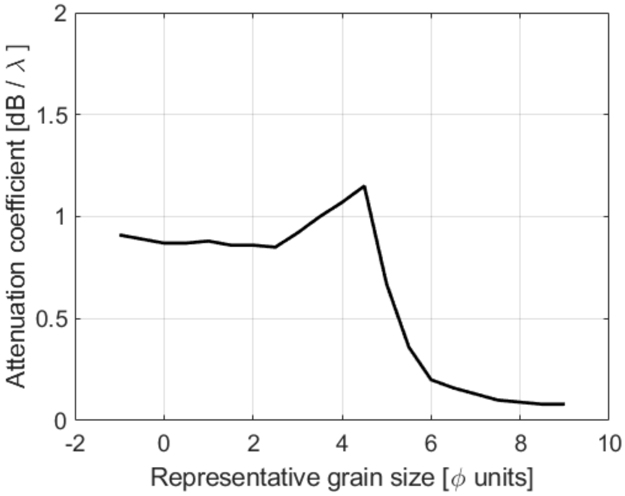

Figure 8-9: Attenuation coefficient vs grain size, based on [18].

To gain insight in the validity of the estimated attenuation coefficient, it is compared to the variability in a target echo response for a buried object with frequency. Such a measurement can also only be used as an indicator, because it combines the target echo response with the effect of attenuation. Nevertheless, the trend observed with frequency in the measured data suggests that the estimated α_s =1.6 dB/λ is too high. A value of α_s in the range between 0.5 and 0.7 dB/λ would better explain the observed trend in the observed echo level with frequency. This indicates that the interpretation of the measured BSS with range is not correct, or at least that there is insufficient understanding of the trends in BSS versus range. Possible explanations is that the mud layer consists of multiple layers, there may be additional reflection and transmission losses, or unexpected source directivity effects.

8.5 Conclusions

Information on seabed sediment types is often available prior to the start of an UXO detection and remediation survey. By using empirical relations between grain size and acoustic sediment properties, reliable estimates can be obtained on the sediment sound speed. Knowledge on sediment sound speed is important, because the existence of a critical angle has a large impact on the coverage that can be achieved in detection surveys for buried UXO objects.

In a scenario in which there is significant uncertainty on the acoustic seabed parameters, or significant variability, additional information on acoustic seabed parameters will be required to support coverage assessment:

- In a downlooking configuration, information on acoustic seabed properties can be obtained using a downlooking single-beam or multi-beam echo sounder. It is known that with SBES or MBES, good insight can be obtained in the variability in acoustic seabed properties. Absolute calibration of SBES/MBES measurements often remains challenging. Based on a combination of SBES/MBES measurements and in-situ measurements (grab samples, gravity cores), inferences can be made on grain size of sediment, and empirical relations can be subsequently used to estimate the sediment sound speed. However, there remains a significant uncertainty in the sediment attenuation in this approach.
- It is challenging to obtain information on acoustic seabed parameters relevant for coverage assessment from a sidelooking sonar system. The analysis of backscattering data is

complex. It is not straightforward to make inferences on sediment sound speed and attenuation, because scattering mainly originates at rough interfaces and inhomogeneities.

- By using bistatic measurements, geoacoustic inversion techniques can be used to make direct inferences on sediment sound speed and absorption. Additional information on attenuation improves the accuracy of predications up to which depth UXO objects of interest are detectable. A drawback is that bistatic measurements will require additional equipment and time. Furthermore, there are often significant uncertainties that remain in the geoacoustic parameters that are to be estimated.
- In-situ measurements are an important aid for acoustic seabed classification. At specific locations, direct measurements of relevant properties can be obtained. In-situ measurements can be obtained with dedicated equipment, such as buried hydrophones or instrumented test targets. The analysis of SNR for buried objects, observed at different ranges (or the absence of a contact corresponding to such an object) and frequencies, can also provide information on the relevant acoustic seabed properties. In-situ measurements are rather valuable. A drawback is that they provide information only at a specific location.

9 Simulation of target in environment response

The target in environment response (TIER) is a combination of target scattering, source-target propagation, target-receiver propagation and processing of the received signal as shown in Figure 9-1. The TIER depends on signal, target and environment properties as explained in Chapter 5. The interaction of the incident field with the target can be modelled in several ways and varies in level of complexity and required computational efforts. Different methods to calculate the target strength (TS) are

- to use an empirically derived TS based on a simplification of the target to a shape for which an analytical solution is available, or
- to use 2.5D or 3D finite element modeling (FEM) to compute the TS.

For this study 2.5D FE modeling is used, which is a good balance between being able to model a high level of detail and reasonable computation time at the cost of only being able to simulate axisymmetric targets. This is often the case for UXO objects. In this way it is possible to perform coverage assessment for a large range of different target properties.

In this chapter the simulation approach to obtain the target in environment response including processing of the received signal is explained. Simulations of the TIER have been shown before in other studies, but results including processing are limited. Therefore, the focus of the results is how to obtain a time series response of an UXO object of interest, which is needed as input to LF-SAS processing. The approach is explained here using a simulated scattering response of a proud solid aluminum cylinder. The same method applies to the simulation of the time series response of a buried UXO object. The only difference is that then the transmission of sound into the sediment has to be taken into account as an additional step.

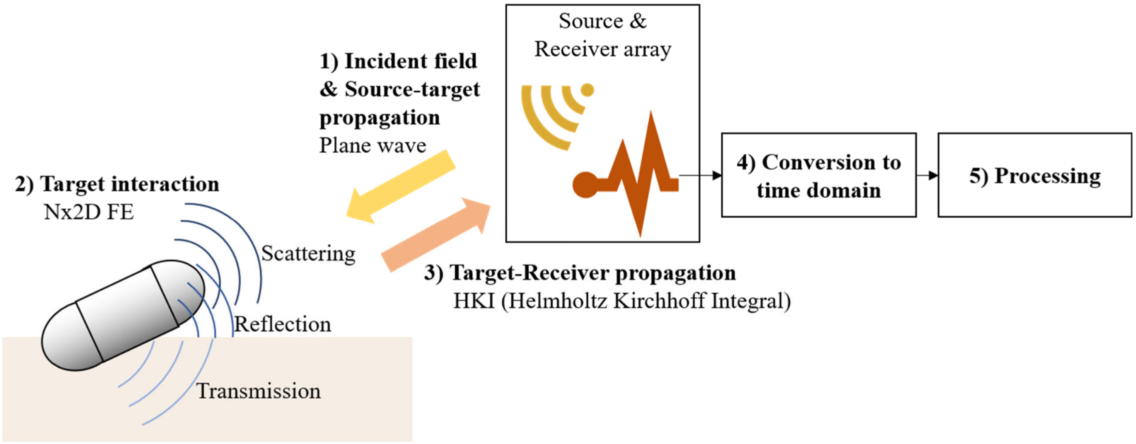

Figure 9-1: Simulation chain for target in environment response including processing.

9.1 Simulation approach

9.1.1 Target strength simulation

The target strength is simulated using a 2.5D FE method, which assumes an axisymmetric target and can include a single sediment layer. The sediment and water are both treated as half-spaces, unbounded fluid domains where the Sommerfeld radiation criterium must hold at infinity.

The simulation starts with the propagation of the incident field from source to target. A plane wave oriented towards the center of the target is currently taken as incident field, but it is possible to implement a more complex incident wave. The direct, reflected and transmitted parts of the incident field on the target are all calculated in the case of a fluid-sediment interface.

The elastic response of the target is determined by how the target oscillates as a result of the impinging acoustic pulse and by how these oscillations are radiated. Both can be described by structural acoustics and can be modelled using the finite element method. To minimize the computational cost only the scattering of axisymmetric targets can be computed as the FE calculation can then be split in a set of 2D calculations. The size of the set depends on the maximum circumferential Fourier component (mode) that is taken into account, which is derived from the target size and the maximum frequency. Higher modes can be discarded as they mostly excite evanescent waves [25][29]. The FE simulations include currently only first-order scattering. Higher-order scattering such as the target-seafloor-target field is not taken into account. However, by adding an additional FEM step in which the target is excited by the reflected field it is possible to add higher-order scattering as well [29].

The short-range elastic response is calculated and given by the pressure and normal particle displacement at a surface enclosing the object and needs to be propagated to the receiver positions to obtain the long-range response. The propagation is done using a numerical approximation of the Helmholtz-Kirchhoff integral for which the appropriate Green's kernel of the background medium needs to be evaluated [40]. The model outputs the target scattering at the receiver positions as a function of frequency.

9.1.2 Target strength simulations for different types of environment

Besides the environmental parameters as sound speed and attenuation of the medium, other environmental properties can be directly included in the target strength simulations as well. The FE approach allows for either an homogeneous surrounding medium (water) or a medium with a single sediment layer (water-sediment). For the latter case the target can be proud, buried or partly buried. The modeling assumptions related to the different environments shown in Figure 9-2 are described in this section.

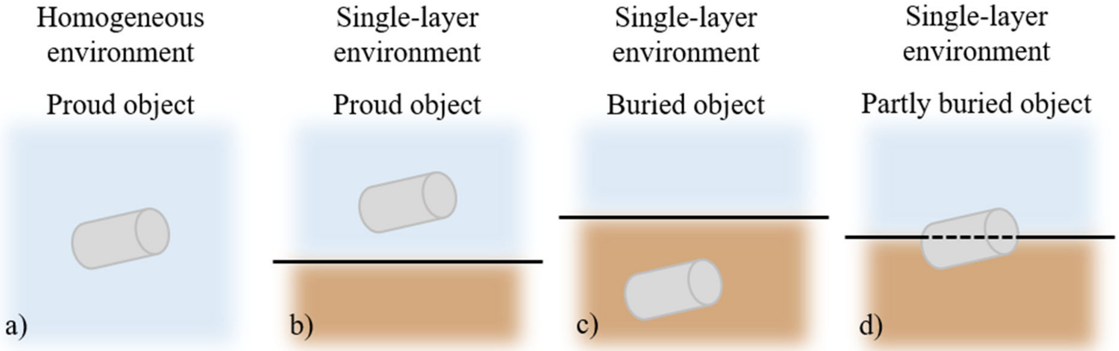

Figure 9-2: The different environments that can be modelled in the FE simulations. The surrounding environment can be either an homogeneous environment (a) or include a single sediment layer (b-d). In the latter case the target can be either proud, buried or partly buried.

For all cases it is assumed that each medium is fully elastic and homogeneous. Local variations in sound speed or attenuation are not incorporated in the model. When a sediment layer such as sand or mud is present, refraction and reflection effects are taken into account in the propagation part of the simulation, though interaction with the target is limited to first-order effects. Second order scattering can be included by running a second iteration of FE scattering calculations with the reflection of the 1st scattered field as the incident field, as shown in Figure 9-3. Including higher order scattering results in a slight improvement of the far field response at specific frequencies [29], though the effect on the estimated coverage assessment is expected to be small. Therefore, the TS simulations are limited to 1st order scattering effects in order to reduce computational cost.

The elastic response of the target depends on the target properties as well as on the properties (speed of sound and attenuation) of the surrounding medium. The surrounding medium is assumed to be homogeneous and fully elastic and can thus be either water or sediment. This means that for partly buried objects the water-sediment interface is not taken into account in the calculation of the near-field elastic response, but only in the propagation of the incident and scattered fields. For partly buried targets either water or sediment has to be chosen as surrounding medium.

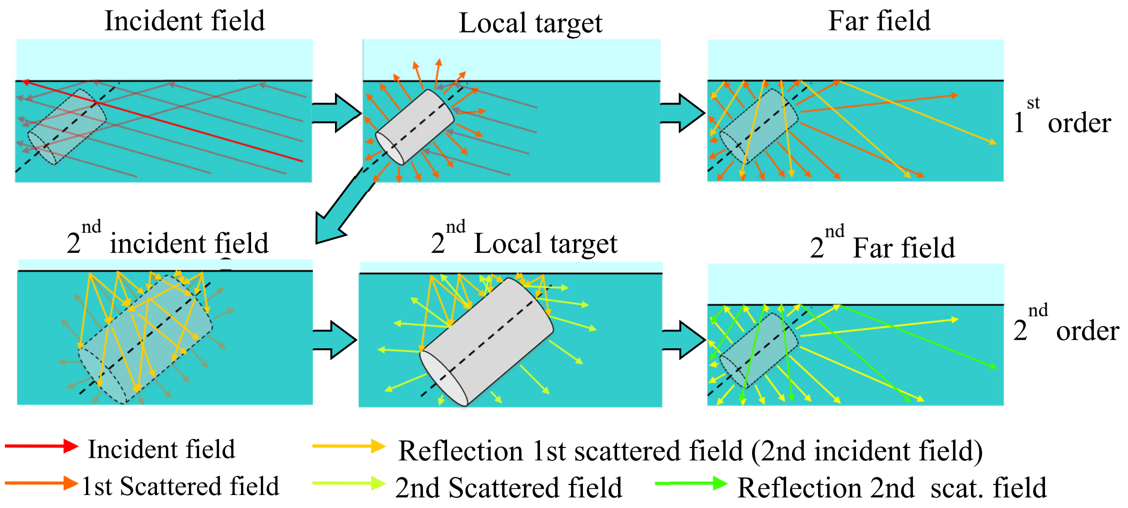

Figure 9-3: Sketch showing incident field, the 1st and 2nd order scattering field of a target and the corresponding far field [29].

9.1.3 Table-look-up approach for target strength simulations

When one wants to determine the TS for a range of source and receiver positions and/or different target positions, orientations and depths, a look-up table can be used to increase efficiency [25]. The look-up table consists of the responses for each forcing point of the target (the Gauss points). The response for any incident field can then be reconstructed by recombining the results of FEM calculations from different forcing points. Note that the FEM calculations still depend on the surrounding medium, so different look-up tables are needed for proud and buried targets. The look-up table approach is useful if the number of incident fields that need to be modelled exceeds the number of Gauss points of the target as the amount of FEM calculations can then be reduced.

9.2 Simulation results

The target in environment simulations including processing as described above can be done for any axisymmetric object. In this section simulation results are shown for a solid aluminum cylinder "NL-CYL" with a length of 61 cm and a diameter of 30.5 cm. It is a replica of the target used by Williams et al. [22]. The target is located at a depth of 18 m lying proud on a sandy bottom. The source and receiver positions are chosen to be exactly the same as for an experimental run performed in Gdynia, Poland. In this way, the simulated results can be compared to recorded data at a later stage. The source and 100 hydrophones are positioned close to each other on an array. Figure 9-4 shows the target and array positions for the run. The target's axis is aligned with the y-direction.

The sections below will show the simulated target response as a function of frequency, the results after conversion to time domain and the simulated response after processing has been applied.

Figure 9-4: The solid red line shows the array positions (source and receivers) for the simulated run. The open red circle represents the target position and the black lines show the orientation of the incident field. The right panel shows NL-CYL.

9.2.1 Conversion to time domain

For each array location (‘ping’), the complex frequency response including wave propagation effects was calculated for 100 frequencies ranging from 100 Hz to 10 kHz, with increment of 100 Hz. The absolute amplitude corrected for geometrical spreading is displayed in Figure 9-5 for receiver (‘hydrophone’) 100.

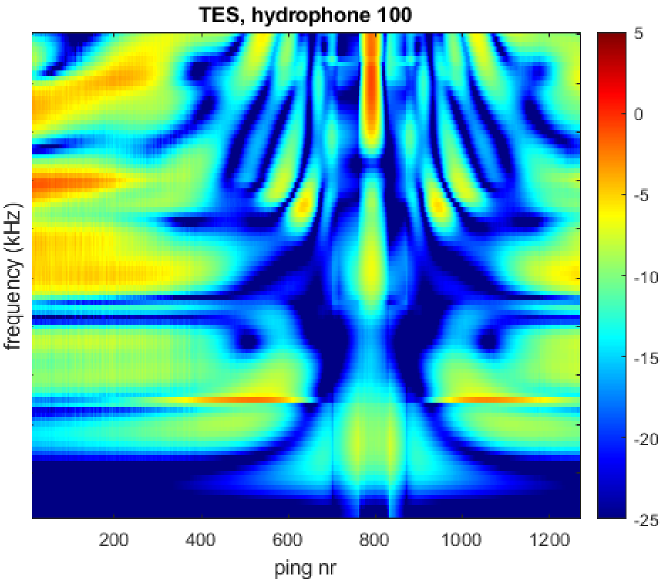

Figure 9-5: Amplitude response (dB) for object NL-CYL as a function of frequency and array location.

By applying an inverse Fourier transform, the time domain signal will be obtained in terms of a band-limited zero-phase pulse. Also some over-sampling in time is desired. By setting the Nyquist frequency to f_N = 40 kHz, the sampling frequency $f_s = 2^* f_N$ becomes 80 kHz with a corresponding sampling interval dt in the time domain of $dt = 1/f_s$ = 12.5 µs.

Subsequently, in order to transform to time, a frequency sample was added at 0 Hz and zero-padding was applied up to the sampling frequency of 80 kHz (800 samples). This was then inverse Fourier transformed, taking the real part and amplitude multiplied by two. This gives the inverse transform result for a 10 ms time window.

The complex frequency response included wave propagation. Hence the obtained time response includes propagation as well, which means the event is expected at arrival times according to the shape of an hyperbola with the apex at CPA, at times greater than 10 ms. This hyperbolic event will be wrapped around in the inverse transform. Hence, to recover the event in time domain the response is concatenated a number of times such that the complete travel time range at all simulated platform locations is covered. Subsequently, the desired response is extracted using a window around the expected travel time. Figure 9-6 shows the time response after concatenation and windowing. The fact that the wrapped-around events can be separated, proves that sufficient amount of frequencies were computed in the TIER modeling. A zoomed version after flattening on arrival time is shown in Figure 9-7.

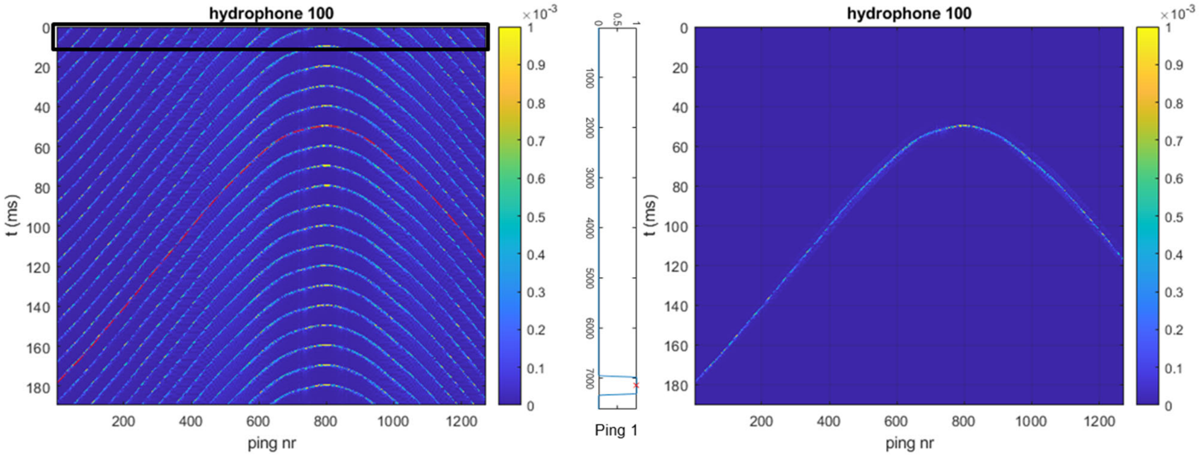

Figure 9-6: Left: time response after concatenation of inverse transform result indicated with a black box. Red dashed line indicates source-target-receiver travel time for hydrophone 100. Right: After windowing. Inset shows flat top window for ping 1.

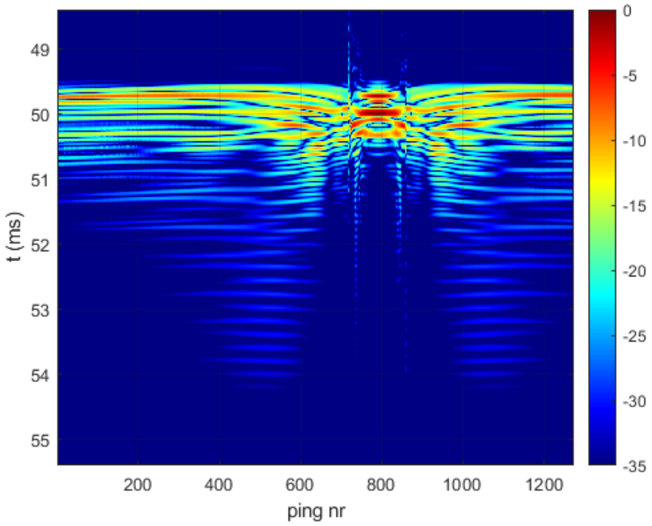

Figure 9-7: Zoomed time response for hydrophone 100 after flattening on arrival time of the object's center.

9.3 Summary

Using FE modeling, high-fidelity TIER data can be obtained. By using the table-lookup-approach, time series data can be obtained for different tracks, target orientations, target positions, target depths without having to repeat the time-consuming FE simulations. They can be all done a priori, and only the table look-up postprocessing is then required to generate the time series data. The first-order effects of changes in acoustic sediment properties (sound speed and attenuation) can also be addressed in the table look-up postprocessing. This covers then the propagation effects, the effect of changes in sediment sound speed and attenuation on the target scattering is then ignored.

10 Processing of target in environment response

Once the time series response of the target in environment is modelled for all source and receiver locations of the MUD system according to the sailed track shown in Figure 9.4, this data is ready to be taken forward to low-frequency synthetic aperture sonar (LF-SAS) processing. The result of this processing will be an image of the object in environment, including data acquisition and processing effects, but otherwise noise-free. Subsequently, reverberation will be blended in from the field data recordings before any processing, as a first look with a signal-to-noise ratio empirically derived from the field data. Finally, this data is processed again to an image comparable to an actual image obtained from the field dataset. Calibration of TIER modeling and processing is critical to allow the insertion of simulated TIER in measured data. The calibration is discussed in Section 11.

10.1 Preprocessing

The main preprocessing steps for SAS processing are propagation loss compensation and basebanding. The propagation loss compensation removes the effect on amplitude of spreading along the travel path. In case of the modelled data, this is done by multiplying with the distance r between target and receiver only. This removes the spherical spreading loss ($1/r$) from target to receiver; for the plane wave propagation from source to target there is no spreading loss. Basebanding moves the signal down its center frequency for data compression. The synthetic data already comes as a zero-phase pulse in the time domain, so no matched filtering is required. Figure 10-1 shows a zoom close to the target location of the time response for a single hydrophone after preprocessing. Near the closest approach, three high-amplitude events are seen with increasing slant range.

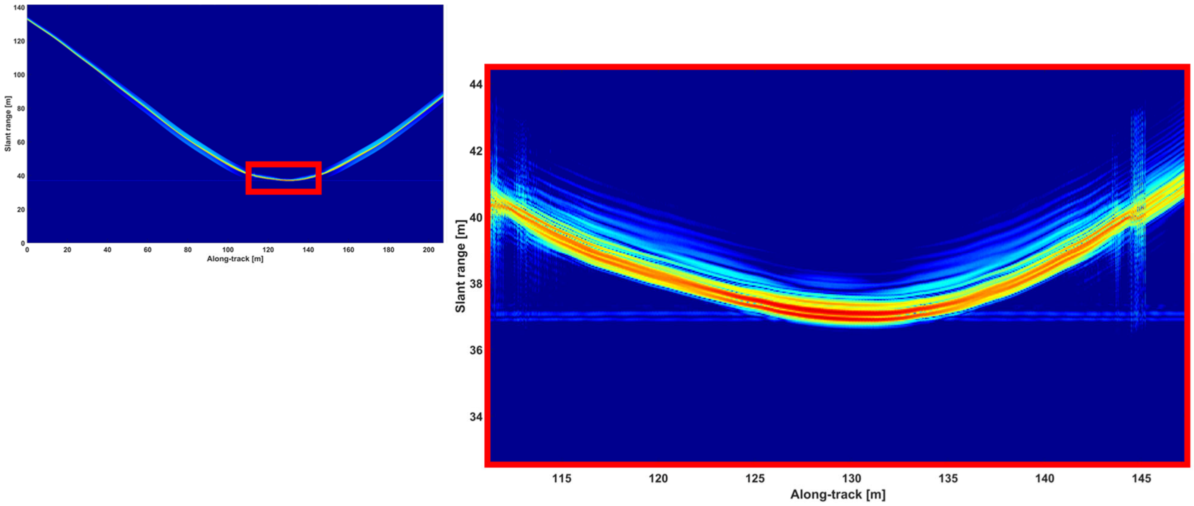

Figure 10-1: zoomed time response for a single hydrophone after preprocessing.

10.2 SAS processing

In the SAS processing workflow, SAS imaging is applied directly to 2D array data, taking the actual receiver positions at each ping into account. Figure 10-2 shows an image of the target. The processing for this image was done in four frequency sub-bands, where the integration angle was reduced from maximum 90 degrees for the higher frequencies in order to get a similar resolution for each band. The target is looked at from broadside. The length along-track of the high-amplitude response in red corresponds well with the target length of 61 cm. Across-track, three main events are visible like in the time response. In this direction, the target width is 30.5 cm. The target center was modelled at 30.78 m across-track and 127.76 m along track, indicated with dashed lines in the image. The response looks similar to the broadside image of a comparably sized object for a controlled experiment described in [22] (although placed at smaller range and imaged with different frequencies). Three main events emanate from the object too in their measurements, which adds confidence to the obtained result.

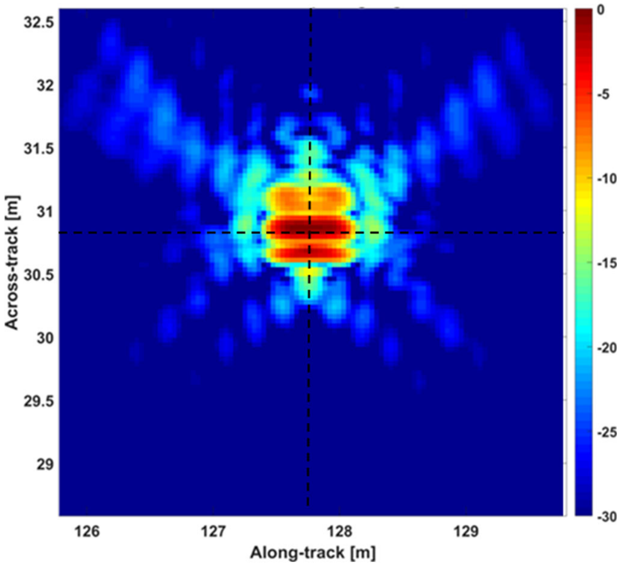

Figure 10-2: SAS image of the NL-CYL for a maximum opening angle of 90 degrees. Amplitude scale in dB relative to the maximum value.

10.3 Fusion of simulated TIER with measured data

This section discusses the fusion of simulated TIER with measured data. This is accomplished by adding the TIER time series to the hydrophone data. Compared to the simulation results in which reverberation is absent, a number of changes is expected in SAS images:

1) The signal-to-reverberation ratio will vary with target range. The SRR, for a buried object will deteriorate when an object is at a higher slant range (e.g. Figure 8-3). This has impact on SAS images, and especially on multi-aspect acoustic color images when data acquisition is being conducted with straight tracks. For proud objects, however, object SRR may increase as a result of reduced backscatter from the sediment due to small grazing angles. This would assume no or little multi-path responses, little background noise and accurate imaging.
2) Data acquisition effects have to be taken into account, such as directivity of transducer and receivers, variations of SL with frequency, and the sailed track.

Figure 10-3 compares the result of the fusion of the TIER-SAS image of the cylinder with the SAS image of the measured reverberation with the corresponding TIER-SAS image in which the reverberation is absent. The SRR of the TIER time series at the closest point of approach is 5 dB, resulting in an SRR in the SAS image of more than 15 dB. The frequency range is limited compared to the simulation results presented in Figure 10-2. The corresponding acoustic color images are displayed in Figure 10-4.

When the angular and spectral properties of the transducer are taken into account in the TIER processing, the angular and range resolution are reduced in the image (Figure 10-5). The compensation for these transducer properties, which can be achieved using a stabilized spectral division [67] improves the resolution, but reduces the SRR.

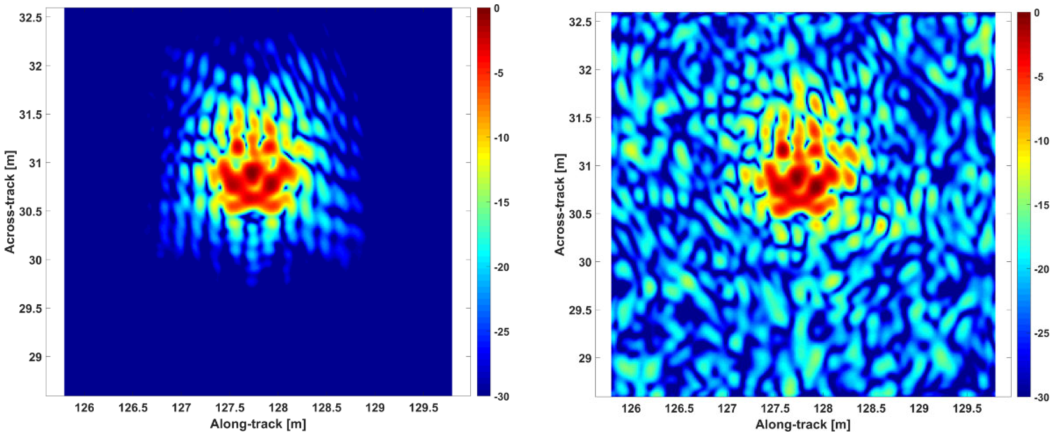

Figure 10-3: SAS image of NL-CYL for a maximum opening angle of 90 degrees using only simulated TIER time series data (left) and fused TIER time series with measured reverberation data (right).

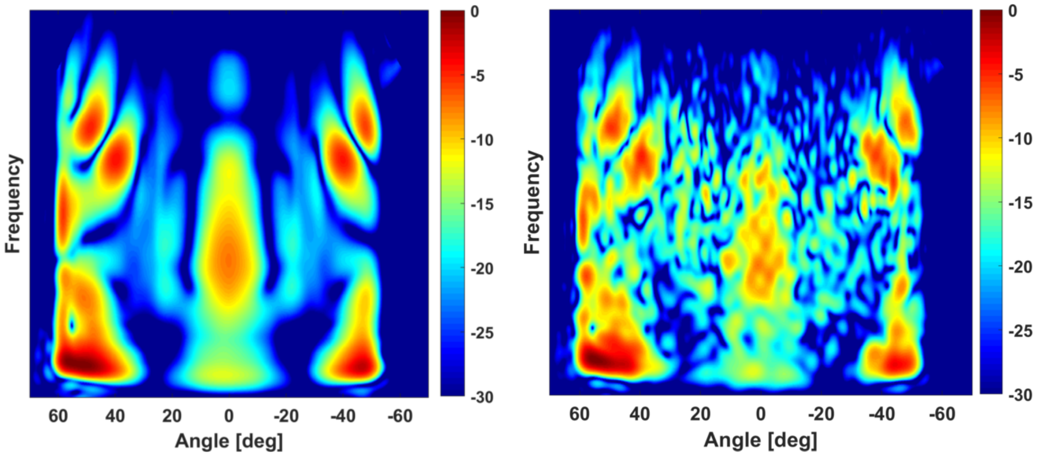

Figure 10-4: Acoustic color images corresponding to Figure 10-3.

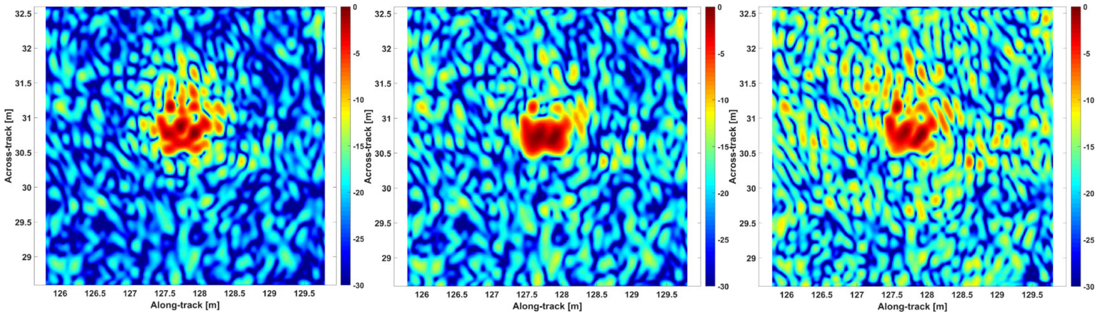

Figure 10-5: SAS image of fused TIER time series with measured reverberation data as shown in Figure 10-3 (left), the corresponding SAS image taking the angular and spectral transducer properties in the TIER time series into account (center), and SAS image compensated for the transducer properties (right).

11 Calibration and validation of TIER processing and modeling

The signal-to-reverberation ratio analysis for coverage assessment relies on the augmentation of simulated TIER in field data recordings. To ensure the compatibility between simulated time series and measured hydrophone data, calibration is required, both for the TIER modeling and for the measured data.

For the TIER simulations, calibration involves the following aspects:

1. Conversion of TIER simulations from acoustic color to time series (section 11.1): Note that we directly simulate matched-filtered data;
2. Source directivity pattern;
3. Propagation loss;
4. Receiver directivity pattern;

For the TIER modeling, matched filtered data are simulated directly. This implies that appropriate normalization is required for the matched filter in the processing chain. Also, consistent scaling needs to be applied for the transformation from frequency to time domain and vice-versa, such that energy is conserved.

For the processing chain, proper calibration for hydrophone sensitivity and A/D conversion needs to be applied, such that the recorded data can be interpreted in dB re $\mu\mathrm{Pa}^2$.

In the calibration, the conversion from TIER to time series from matched filtered data is considered as most complex. This will be discussed in Section 11.1. The source directivity pattern can be established, for example by conducting dedicated measurements in an acoustic test basin, and the receiver directivity pattern can be measured as well. Alternatively, it can be predicted based on information on directivity of individual elements and the array geometry. Finally, spherical spreading is used for propagation loss.

The calibration of the TIER modeling and processing is validated by comparing a simulated for a specific track to the measured TIER of the same response. The validation is discussed in Section 11.2. Challenges in the validation based on model-data comparisons are discussed in Section 11.3.

11.1 Calibration/scaling of TIER modeling: from Acoustic Color to Time Series

In Section 9 it was described how with FE modeling, high-fidelity TIER data can be obtained in the form of acoustic color, i.e. a complex frequency response with aspect angle, which is subsequently transformed to a time series. Transformation from frequency to time series and back is implemented using the discrete Fourier and inverse Fourier transformation (DFFT and DIFFT). They are defined as follows.

Discrete FFT:

$$X(k) = \sum_{n=1}^{N_{\mathrm{fft}}} x(n) \exp[-j2\pi(k-1)(n-1)/N_{\mathrm{fft}}]; \qquad (11.1)$$

Discrete IFFT:

$$x(n) = \sum_{k=1}^{N_{\mathrm{ifft}}} X(k) \exp[j2\pi(k-1)(n-1)/N_{\mathrm{ifft}}]; \qquad (11.2)$$

The frequency sampling interval is $\Delta f = f_s/N$, where $f_s = 1/\Delta t$ is the sampling frequency, and N is the number of samples used in the DFFT and DIFFT.

The DFFT uses a transformation $t' = at$ such that the integrand runs between 0 and $N - 1$, with $a = 1/\Delta t$. Changing the integration from t to t' results in an additional scalar, a multiplication with Δt . Likewise for the DIFFT, which results in a multiplication with Δf. Using this scaling, the DFFT/DIFFT will be energy preserving, which was verified using Parceval's theorem:

$$\sum_{i=1}^{N} |x(n)|^2 \Delta t = \sum_{i=1}^{N} |X(k)|^2 \Delta f. \tag{11.3}$$

With this scaling in place, the expected amplitude of the TIER simulation in the time domain can be understood as follows. First, the concept Source Level Energy SL_E is introduced, which is the total energy contained in a source pulse:

$$SL_E = SL + 10\log_{10} T \tag{11.4}$$

In this equation, SL is the source level and T the pulse duration. Source level energy can also be defined in the frequency domain:

$$SL_E = 10\log_{10} |M|^2 + 10\log_{10} B \tag{11.5}$$

In this equation, B is the bandwidth, and M is referred to as the spectral amplitude [18]. Note that $10\log_{10}|M|^2$ has dimensions [dB re $\mu\text{Pa}^2\text{m}^2/\text{Hz}^2$].

Suppose that the TIER simulations are conducted using $10\log_{10}|M|^2 = 0$ dB re $\mu\text{Pa}^2\text{m}^2/\text{Hz}^2$. Consequently, the $SL_E = 10\log_{10} B$. Assuming that the duration of a matched filter signal in the time domain is equal to 1/B, the corresponding $SL = 20\log_{10} B$. This corresponds then to a sinc function with peak amplitude B. Virtually all energy is contained in the resolution cell with duration 1/B. This was confirmed on the TIER simulations. In order to interpret the resulting amplitudes as target strength TS, $10\log_{10}|M|^2$ is scaled with $20\log_{10} B$.

Another aspect that deserves attention is the calibration is scaling of the matched filter, because we simulate directly matched-filtered data.

For the measured data, matched filtering is implemented in the frequency domain as a stabilized deconvolution:

$$X^{MF} = \frac{X * conj(P)}{\max(|P|^2, \epsilon)} \tag{11.6}$$

In which X is the signal and P is the source wavelet, and ϵ is a small number used to avoid zeros in the denominator.

11.2 Validation of results using proud target: NL-CYL

The simulated and measured response for NL-CYL are displayed after vertical beamforming in Figure 11-1. It shows the simulated TIER for NL-CYL, which has a diameter of 0.30 m, half-buried, and just 0.05 m buried, and also simulated TIER with added background. The exact burial conditions are not known – targets were deployed several months before the survey was conducted in this specific trial to mitigate perturbations introduced in the sediment caused by target burial, and, unfortunately, they were not established during the trial or during the target recovery.

The reverberation background in the data with the measured target response differs from the reverberation background added to the simulated TIER response. The reason is that the addition of the simulated TIER to reverberation background cannot be done using exactly the same reverberation background because of the presence of the target, i.e. a target-free part of the seabed in the same survey has been used instead for the background reverberation to avoid interferences.

The comparison between the modeled and measured TIER shows that a good agreement is obtained in the magnitude and also in the TIER observed for different aspect angles. It furthermore reveals that small differences in the burial conditions of the target impact the magnitude of the TIER. The differences between the TIER of the two different simulations is larger than the difference between the simulated TIER (half-buried target) and the corresponding measured TIER. This result is confirmed by the corresponding SAS images which are presented in Figure 11-2. It shows a good agreement between the modeled and measured TIER, both in intensity as in character.

Based on these results, we have sufficient confidence in the calibration of the simulations for TIER and in the process to augment targets to measured reverberation data. The model-data comparison also reveals challenges that are encountered in TIER model-data comparisons. They are further discussed in the next section.

11.3 Discussion on validation of TIER modeling

The validation results presented in the previous section suggest that it is difficult to get a good agreement between the simulated TIER and measured TIER, i.e. to get a good agreement on the full TIER response, especially in settings which are not specifically designed to enable model validation. Possible explanations are discussed in the subsequent sub-sections.

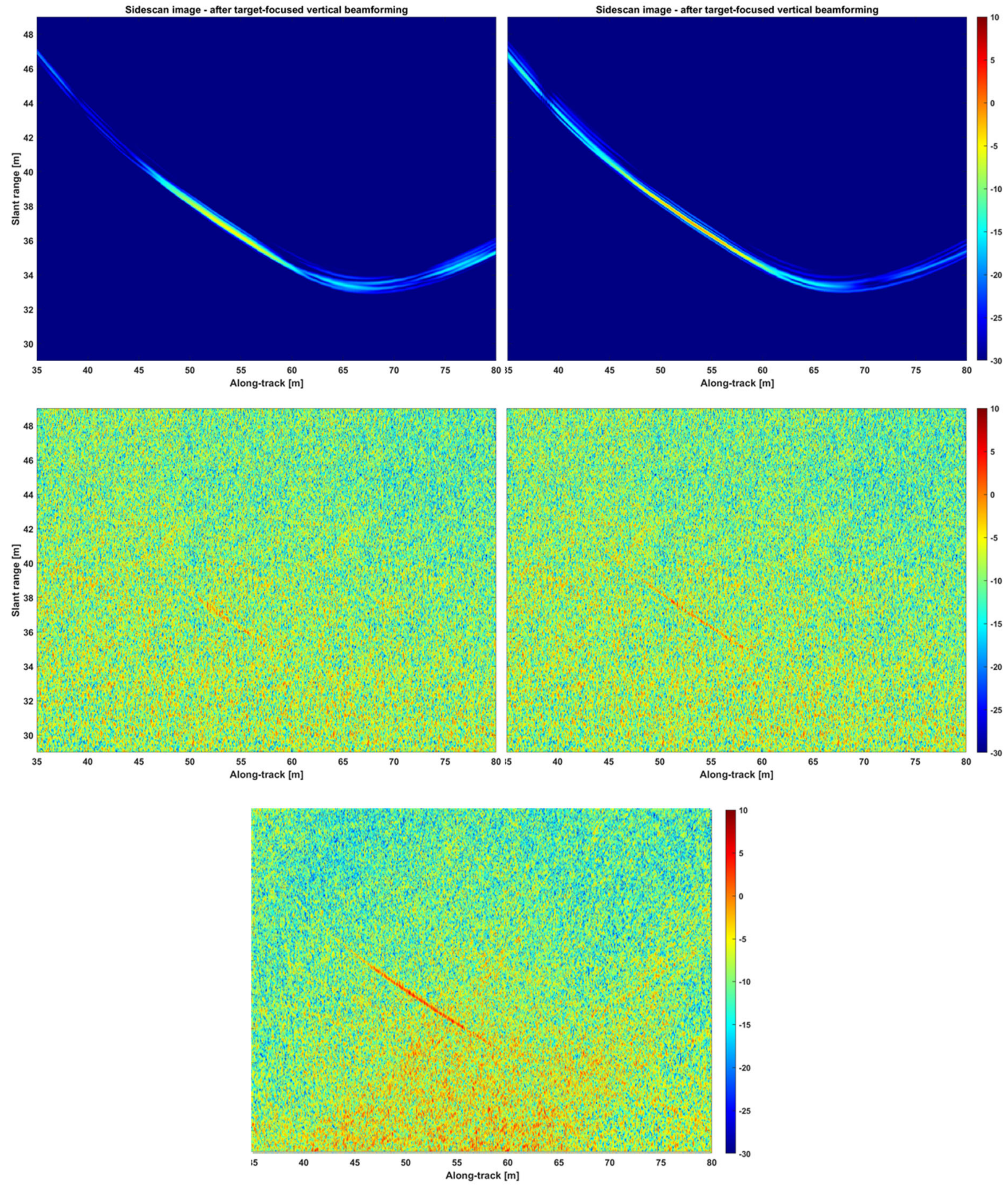

Figure 11-1: Upper 4 panels: NL-CYL simulated TIER response before (top) and after blending (middle) with measured reverberation data . On the left the target base was buried 5 cm, on the right half-buried. Bottom panel: NL-CYL on measurements.

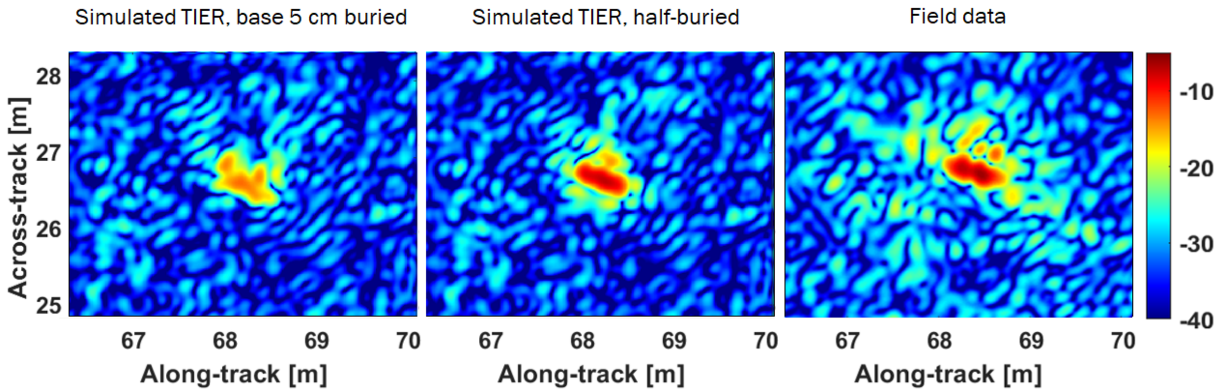

Figure 11-2: SAS images for NL-CYL simulated TIER response after blending with measured reverberation data (left – base 5 cm buried; middle – half-buried); NL-CYL on measurements (right).

11.3.1 Uncertainty in target orientation

Especially for buried targets, it is likely that there remains uncertainty in the target orientation, because it cannot be validated by visual inspection. To avoid this source of uncertainty, it is recommended to use instrumented targets [68] deployed with INS and communication devices to resolve this source of uncertainty.

11.3.2 Burial conditions

As already shown in Figure 11-2, simulations suggest that there are significant differences in TIER for proud objects vs partially buried objects. To mitigate this uncertainty for partially buried objects, it is recommended to measure exactly the burial depth (or partial burial) during the target deployment and recovery, and/or to measure the height of the object above the seabed using a) a multi-beam echo sounder, b) interferometric sonar, or c) to derive it indirectly from shadow length in SSS measurements. Note that a low-frequency interferometric sonar may not give the correct reference depth for the seabed (cf Section 4).

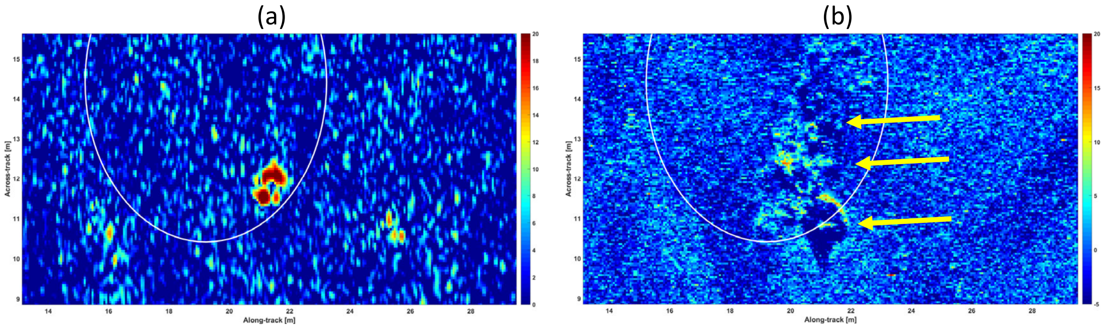

Figure 11-3: (a) LF-SAS response of a deployed buried object in Den Helder harbour (b) and corresponding high-frequency SSS image showing perturbations of the water/mud interface. The white circle denotes the ground-truth position measured during target deployment with GPS (and associated uncertainty), the yellow arrows indicate perturbations of the seabed introduced during target deployment.

11.3.3 Perturbations introduced during target deployment

When experiments are being conducted, target burial may result in perturbations of the sediment. This could subsequently lead to a more complex TIER in comparison to the modeled TIER. An example is presented in Figure 11-3. The high-frequency SSS image shows perturbations in the water/mud layer interface which potentially impact the LF-SAS TIER.

11.3.4 Changes in TIER over time

In environments with tidal currents, scour will occur, which also is believed to impact the TIER. The impact of corrosion and biofouling has been investigated in [2], and the effect on LF-SAS was considered to be small. The buoyancy factor of the target will impacts the target mobility.

11.3.5 Complex seabed sediment structures

All the previous aspects considered primarily the target itself. The sediment itself also contributes to the complexity of the TIER response. As indicated by [29] complex interaction of sound with target and sediment leads to high-order scattering responses.

The Haringvliet environment, which is one of our test sites, is well studied. The complexity of seabed sediment structures encountered in a fluvial-tidal regime are discussed in [69], and two examples from this paper are presented in Figure 11-4. It shows that sediment layer is not necessarily horizontally layered, i.e. in fluvial tidal environments, so-called X-bedding structures can be encountered.

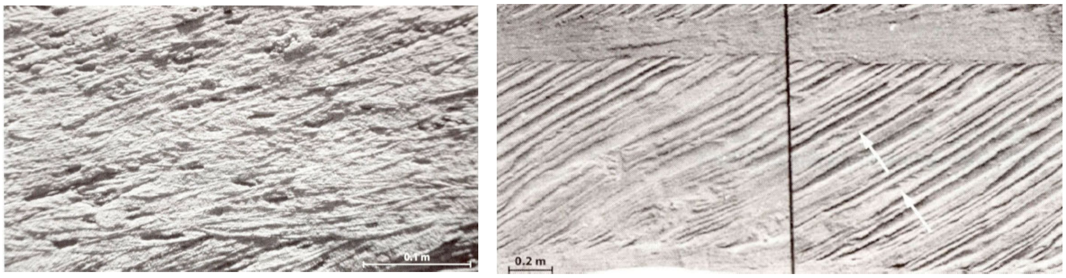

Figure 11-4: Examples from an exposure (during the construction of a tunnel) revealing sediment structures in the Rhine-Meuse delta, from [69].

11.3.6 Data acquisition and processing

As detailed in this report, the comparison of modelled TIER to measured TIER requires that the entire data acquisition chain and processing is calibrated. In addition, platform motion needs to be accurately measured such that it can be fully taken into account in the SAS processing. Uncompensated motion errors will lead to artefacts in SAS images.

11.3.7 Acoustic color

An important image representation is multi-aspect acoustic color (MAAC). This image representation contains valuable information to aid target classification. For these applications, it is important to know which information can be reliably obtained, and which information in the MAAC representation is sensitive to the reverberation background. An example of MAAC derived from simulations only and MAAC for simulation and background is presented in Figure 11-5. It illustrates the sensitivity of MAAC to the reverberation background.

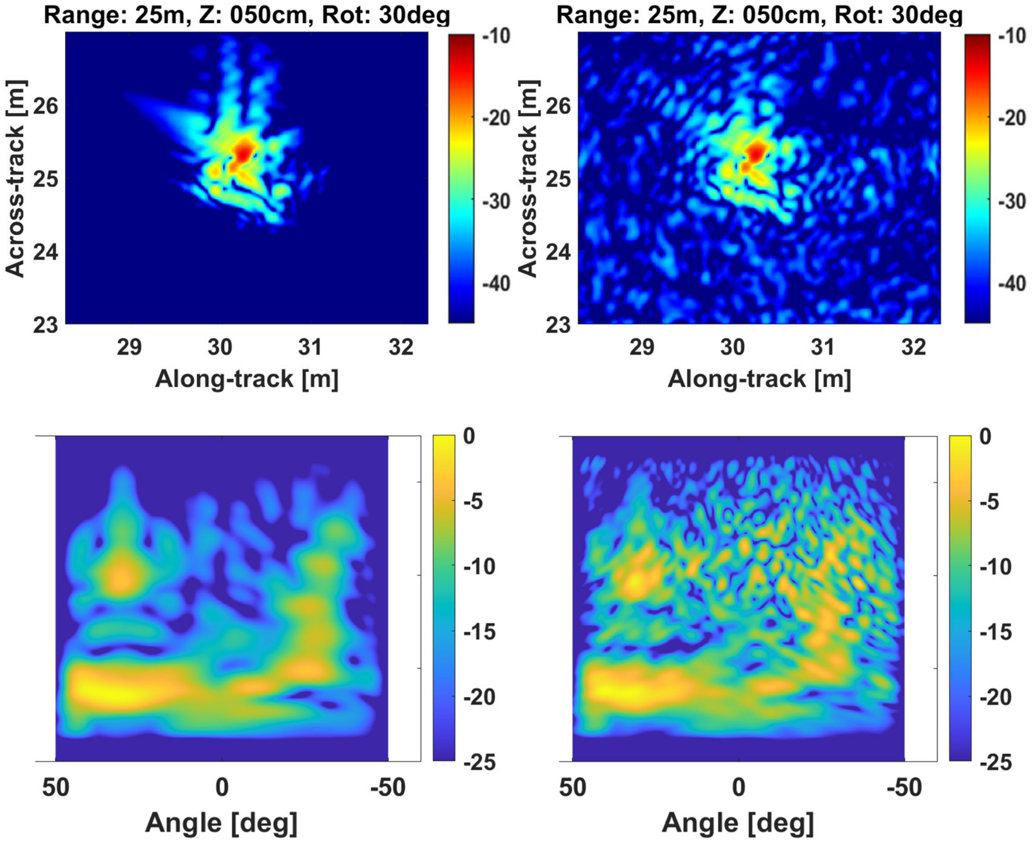

Figure 11-5: SAS images (top) and corresponding multi-aspect acoustic colour (bottom), for simulated TIER wihout mixing of measured data (left) and with (right). Note how the reverberation noise at and around the target in the SAS image spreads and obscures the multi-aspect acoustic colour image.

12 Coverage assessment results and comparison to measurements

12.1 Introduction

This section presents coverage assessment results, and compares these results to measurements. By augmenting simulated targets in measured reverberation data, information is obtained in the signal-to-reverberation ratio (SRR) and on the signal excess (SE), assuming a detection threshold. These quantities are derived for different target positions (range, along-track), target depths, and target orientations. Based on these quantities, P(y) curves, expressing the probability of detection vs across-track range, and coverage maps can be obtained. Finally, the sensitivity to different seabed sediment conditions is investigated.

This section is organized as follows. The simulation approach to enable coverage assessment is presented in Section 12.2. Corresponding TIER SAS images augmented to measured reverberation data are discussed in 12.3, and SRR, P(y) curves, and coverage maps are presented in 12.4.

12.2 Coverage assessment simulation approach

The environment for the simulations is chosen to resemble the Gdynia area where field measurements were done with a scientific target at multiple depths. In this way a validation of the predicted coverage assessment can be performed. The buried target is NL-REF, a cylinder with a diameter of 0.5 m and a length of 1.0 m. The axis of symmetry of the cylinder is orientated in the horizontal plane, parallel to the water/sediment interface. Water depth below array center is 20 m. Straight tracks are simulated; track length is such that target is illuminated for the full opening angle of 100° (Figure 12-1). Platform speed is 1.2 m/s; Pulse repetition frequency: 8 Hz.

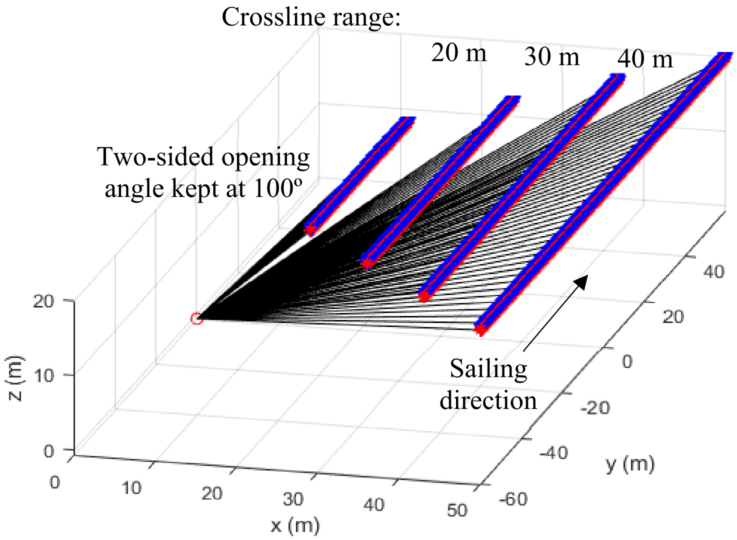

Figure 12-1: Simulated tracks for various crossline ranges, with incident rays from source to target. Opening angle is kept at 100°.

For the base simulation case, a homogeneous sediment half-space of very fine sand was inserted below the water column, this resembles the sediment found in Gdynia based on in-situ sediment samples (Figure 12-2). Speed of sound with critical angle, and density used in the simulations are listed in Table 1. The attenuation in the sediment was taken constant at 0.88 dB/wavelength [18].

Figure 12-2: Sediment sample taken in the Gdynia area. Below 0.19 m, the sediment dominantly consists of fine and very fine sand.

Table 1: Sound speed and density used in the simulations. Values taken from [18].

	Sound speed [m/s]	Sound speed ratio	Critical angle	Density [kg/m^3]	Density ratio
Water	1488	-	-	1025	-
Very fine sand	1655	1.1122	64°	1860	1.8146
Medium sand	1782	1.1976	57°	2138	2.086

To evaluate detectability as a function of target range, target orientation, burial depth and sediment type, a series of simulations were conducted. In the simulations:

- the across-track range to the target was varied from 5 m to 50 m in steps of 5 m;
- Target orientation was increased from 0° to 90° in steps of 15°, where 0° denotes a broadside target response;
- Two sediment types were investigated, very fine sand and medium sand;
- Burial depth to top of target was kept constant at 0.5 m for these tests.

Finally, to obtain a coverage map, the simulated targets can be augmented at different positions, provided that the range to the sailed track is kept constant. All simulations were conducted using a straight track.

The simulation procedure, which relies on FEM simulations, is time consuming. It is, however, applicable to the coverage assessment application, because all simulations can be conducted prior to an experiment, provided that information on acoustic seabed properties are available. With the simulations and the corresponding SAS images available, these SAS images can be augmented in the SAS images of the reverberation. This final step is not time consuming and enables therefore to conduct coverage assessment directly when SAS images become available. It is important that coverage assessment results become quickly available. It enables the modification of UXO survey plans if insufficient coverage is achieved.

12.3 TIER Results for NL-REF

All these simulated TIER in the frequency domain were converted to the time domain as described in section 9.2.1. Subsequently, SAS imaging was applied, with and without measured data blended into the time recordings on hydrophone level (section 10.3). Figure 12-3 shows an example of the blending.

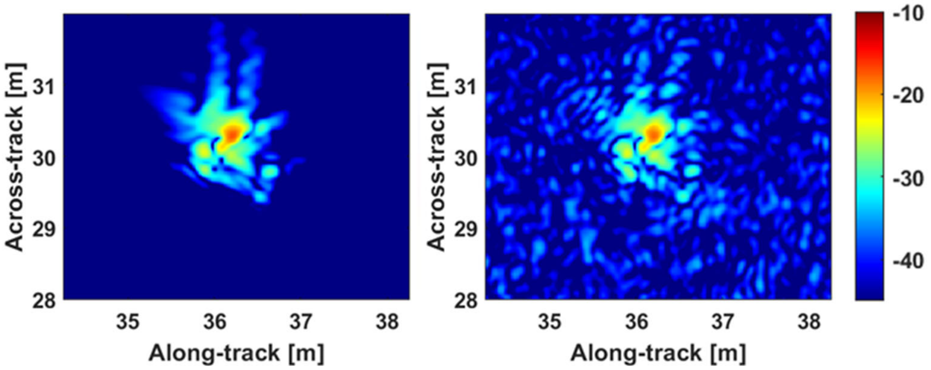

Figure 12-3: Example SAS images of a simulated TIER of NL-REF without (left) and with (right) measured data blended into the time recordings. Target orientation was 30°, crossline distance 30 m, burial depth to top target 0.5 m, sediment type very fine sand.

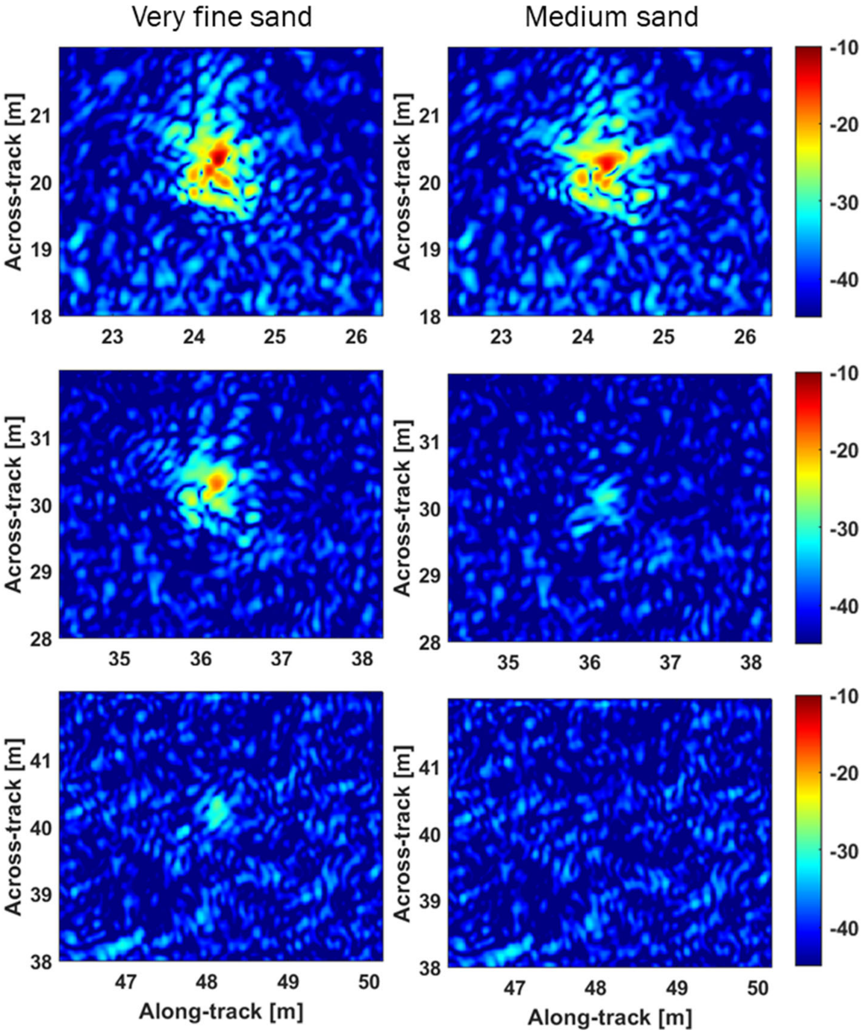

Figure 12-4: TIER SAS images for comparing crossline range and sediment type. Increasing crossline ranges to target from top to bottom: 20-30-40 m. Left column: very fine sand. Right column: medium sand. Note the decreased visibility with range for medium sand compared to very fine sand due to the smaller critical angle.

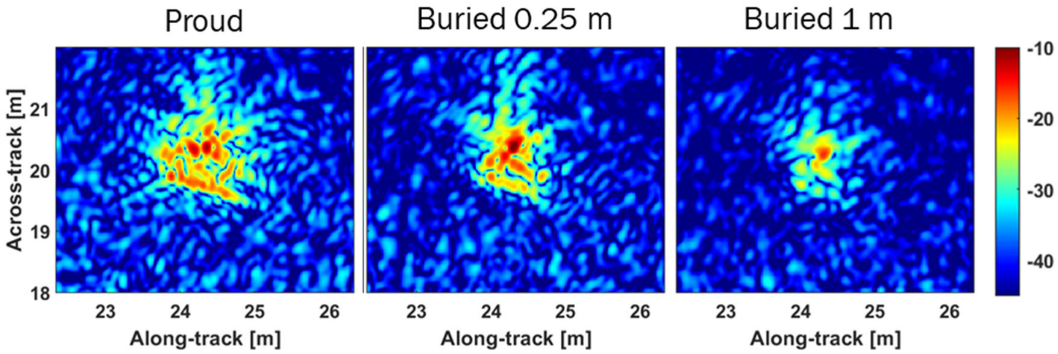

Figure 12-5: TIER SAS images illustrating the effect of burial depth. Increasing burial depth from left to right.

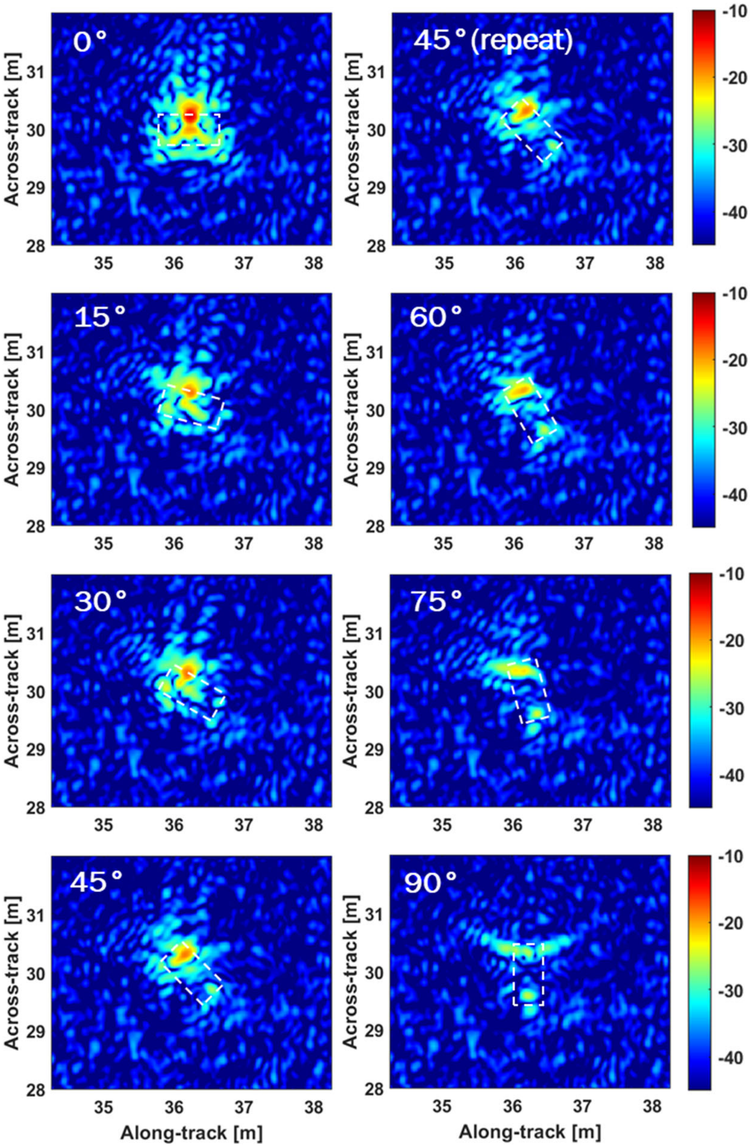

Figure 12-6: TIER SAS images illustrating the effect of orientation. In dashed white line the target outline.

Figure 12-4 illustrates the effect of increasing across-track range. For the ranges shown, there is a general decrease in intensity, with hardly any detectability left for ranges corresponding to angles around the critical angle. Also the effect of a different sediment type is discernable. For ‘medium sand’ the critical angle is smaller, lowering the maximum crossline range for which the target is visible.

In Figure 12-5, the effect of increasing burial depth is shown. Intensity decreases due to increasing absorption. Note the proud object has the largest footprint, but not the largest intensity. Finally, in Figure 12-6 the effect of orientation is shown. Broadside orientation has the largest intensity, while for 90° not much backscatter occurs from the flat end of the target.

Also it appears most of the intensity coincides with the location of the back side of the target.

12.4 Signal-to-reverberation ratio, P(y) curves, and coverage maps

In this section, first signal-to-reverberation (SRR) ratio is calculated from the simulations as a function of cross range and burial depth. Subsequently, coverage assessment results are presented using probability of detection and coverage maps.

12.4.1 Signal-to-reverberation ratio

On the obtained TIER-SAS images fused with measured data, the signal-to-reverberation ratio (SRR) was computed by first subtracting the background trend (Figure 12-7), and then determining the peak magnitude in an area covering the target after some mild spatial smoothing to suppress outliers.

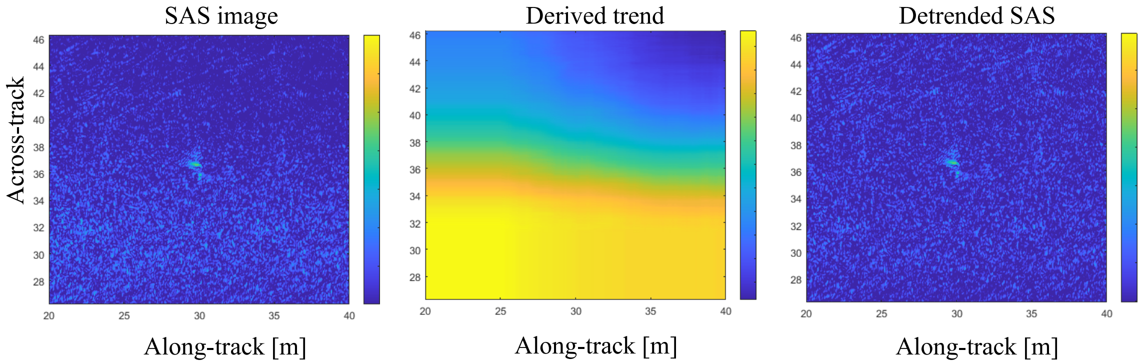
SAS image

Derived trend

Detrended SAS

Figure 12-7: Detrending of the SAS image for SRR determination.

The SRR plots for the experiments where cross range and target orientation were varied, are given in Figure 12-8, with sediment type ‘very fine sand’ on the left and ‘medium sand’ on the right. Note how ‘medium sand’ negatively affects SRR with range due to the smaller critical angle. Also, note how the SRR decreases with increasing orientation angle beyond 45° off-broadside, as the cylinder end comes into view. The cylinder end has a much smaller cross-sectional area, and the flat surface causes incident waves to reflect deeper into the subsurface rather than to scatter back (for the geometrical part of the target response). The behavior with orientation will be highly dependent on the shape of the target.

The corresponding SRR observations in data are presented in Figure 12-9. A similarly shaped curve is observed in the data as on the simulations for ‘very fine sand’ (the sediment assumed to be dominantly present in Gdynia), with a peak approximately at 20 m cross-range, an SRR increase of about 2.5 dB between 10 and 20 m, and a drop of about 15-20 dB from 20 m to 45 m.

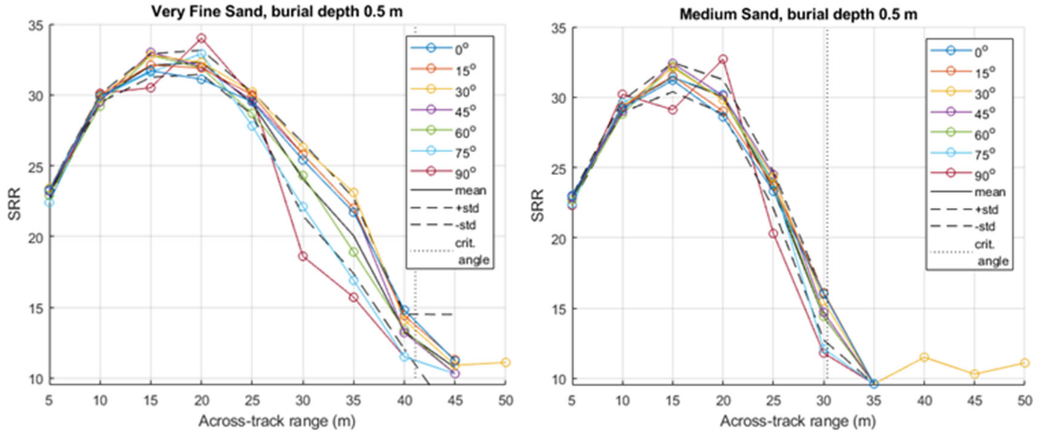

Figure 12-8: SRR as a function of crossline range and target orientation for NL-REF TIER simulations. Sediment type 'very fine sand' on the left, 'medium sand' on the right. Burial depth top top target is 0.5 m.

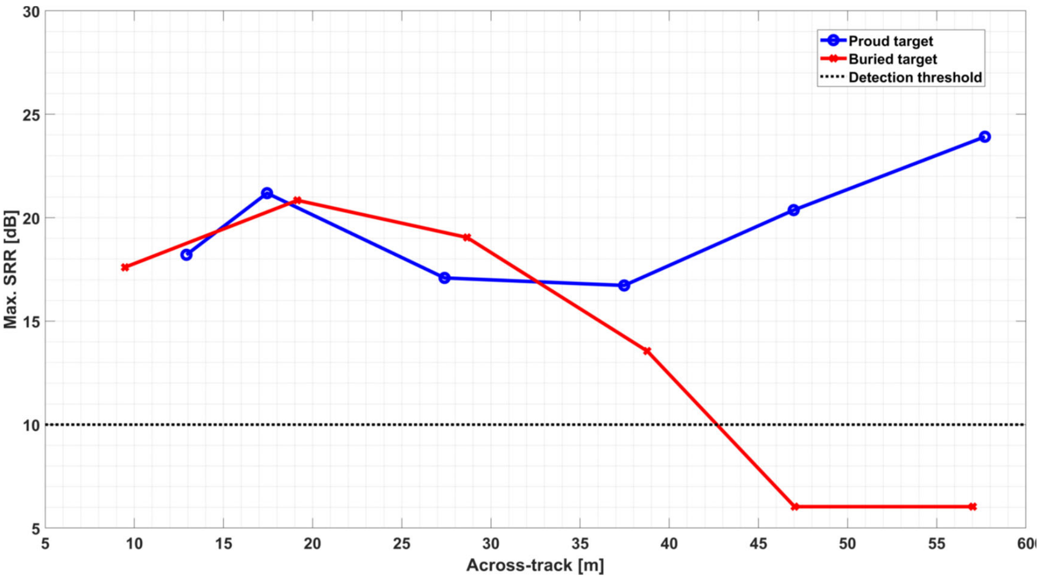

Figure 12-9: SRR as function of crossline range for buried and proud NL-REF, real data observations from Gdynia area.

12.4.2 P(y) curves

P(y) is the probability of detection (P) as a function of cross range (y). It is an averaged performance metric commonly used for survey planning. To obtain P(y) curves, range bins are defined, and subsequently the ratio of number of observations in a range bin (i.e. with SRR above a detector threshold) is divided by the number of sighting opportunities in that range bin.

In Figure 12-10, P(y) curves are shown for sediment type 'very fine sand' and 'medium sand', using all simulations available for those sediments (most simulations have target burial depth 0.5 m). Crossline bin size was 5 m. It is shown for two different detector thresholds, for example representing interpreter skill. Based on these curves a decision can be made on the maximum distance between tracks in order to still have a good chance on detection.

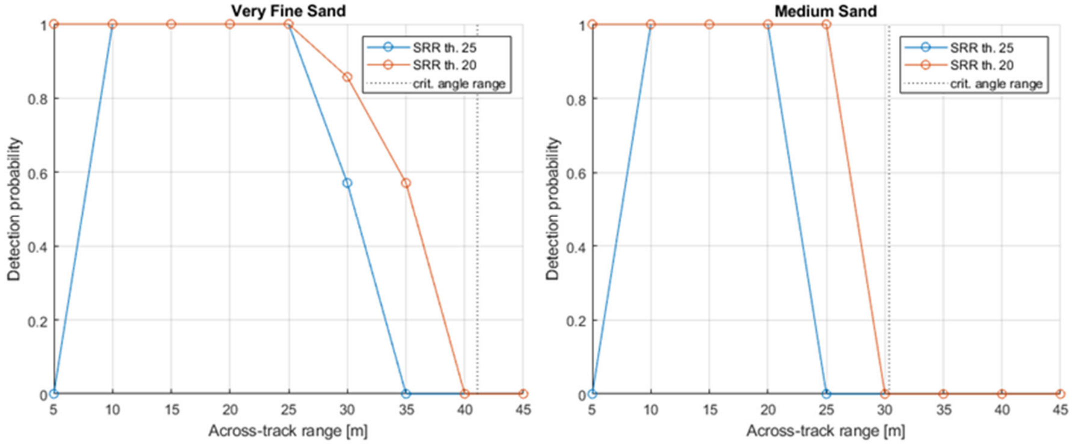

Figure 12-10: P(y) curve for sediment type 'very fine sand' (left) and 'medium sand' (right), for two different detector thresholds, 20 dB and 25 dB, respectively. Dashed line indicates critical angle range.

12.4.3 Coverage maps

The main usage of P(y) curves is to support planning. They provide and averaged performance as a function of cross-range. Coverage maps are important to gain insight in the achieved performance, especially when the reverberation level varies with location.

Once simulations are obtained for targets of interest at different cross-ranges, burial depths, and orientations, and the corresponding SAS images are obtained, which can be achieved prior to a survey, the calculation of a coverage map is not time consuming any more. This means that this can be achieved to quickly evaluate the coverage during a survey, such that it is possible to use the coverage assessment results for further planning.

In the coverage maps, the quantity Signal Excess (SE) is depicted, which is defined as:

$$SE = SRR - DT \qquad (12.1)$$

In this relation, DT is a detection threshold. It has been set to 10 dB. A SRR threshold detector is a simple detector that is used to demonstrate the coverage-assessment principle. The methodology should also be applicable to more sophisticated detectors.

In Figure 12-11, (a) is a SAS image for a particular track from the Gdynia area. Using spatial smoothing, a background level was extracted. Subsequently a detection threshold of 10 dB was chosen and added to the background level, giving image (b). Using the signal level as a function of cross range from the simulations, the Signal Excess map is obtained (c and e). These were constructed for sediment type 'very fine sand' and 'medium sand', burial depth of 0.5 m, and 30° target orientation. As can be seen from Figure 12-8, the map should also be valid within a standard deviation for orientations 0-60° of target NL-REF.

The coverage maps illustrate the importance of geoacoustic characterization of the seabed. The maximum range with SE > 5 dB is reduced from 40 m to 30 m in the case of a transition from very find sand to medium sand. At short ranges, the SE is smaller compared to intermediate ranges. This is because the high-reverberation levels that are obtained at large grazing angles.

Short-range target detection requires that imaging systems have sufficient depth resolution to separate reflection from the seabed and sub-surface interfaces from target scattering.

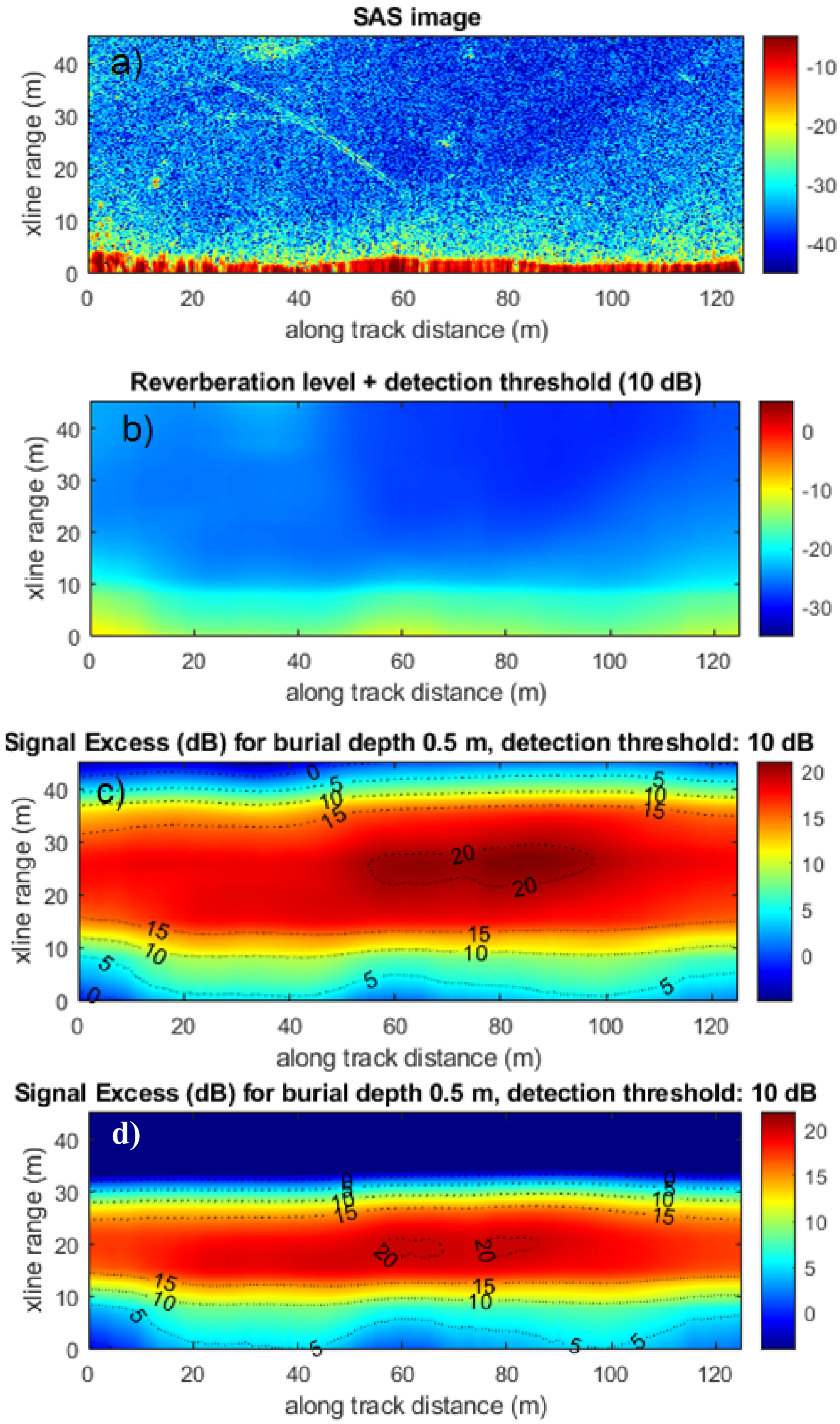

Figure 12-11: (a) SAS image of an example track from the survey. (b) Derived background trend with added detection threshold. (c and d) Coverage maps for NL-REF for 'very fine sand' and 'medium sand', with target orientation 30° and target burial depth of 0.5 m.

13 Conclusions and outlook

13.1 Conclusions

This report introduces a methodology for area and depth coverage assessment and evaluates the feasibility of the approach. The method relies on high-fidelity FEM TIER simulations of UXO objects of interest, which are subsequently merged with measured reverberation data. The detectability of the UXO objects of interest is assessed in SAS images, considering the Signal Excess (SE) for different target depths, target orientations, and target ranges. Because high-fidelity TIER simulations are used, it is also possible to assess the coverage for more sophisticated detectors. The impact of different seabed sediments is investigated as well, and coverage assessment results are compared to measurements from TNO's MUD system.

The method relies on the availability of detailed information on the UXO objects of interest as input to FEM simulations. The availability of information of geoacoustic properties of the sediment is necessary as well. The coverage assessment results have shown that the maximum range for detecting buried objects is limited by the critical angle of incidence for a sidelooking LF-SAS system. It is difficult to obtain information on sediment sound speed using an LF-SAS system, which primarily senses back-scattering properties of the seabed. It is therefore important to collect this information on seabed properties by alternative means, e.g. grab samples and/or gravity cores. There are well-established relations between grain size and sediment sound speed.

The coverage assessment methodology critically relies on a calibrated measurement system, processing, and TIER simulation chain. Hardware characteristics, such as beam patterns, need to be established by conducting basin measurements, and scale factors introduced in data acquisition, processing, and simulations need to be taken into account. Errors in the calibration will result in biased coverage assessment results. The availability of measurements in controlled conditions is important in establishing the calibration, as demonstrated by model-data comparisons in this report.

High-fidelity FEM TIER simulations are time consuming. The efficiency of the TIER simulations is improved by using a table-look-up approach, as explained in Section 9. More importantly, the simulations and the corresponding background-free SAS images can all be generated prior to an UXO detection survey. This means that coverage assessment, which require the fusion of these SAS images with the SAS reverberation background, can be easily generated during an UXO detection survey, provided that the simulated TIER SAS images are generated prior to the survey. The availability of coverage assessment results in-mission will help to improve the quality of UXO surveys. Furthermore, averaged performance curves, such as P(y) curves, are useful input to the planning of future UXO surveys.

Coverage assessment has been successfully demonstrated for TNO's MUD system for experimental data acquired near Gdynia, Poland. Simulation results for SRR for a scientific target at multiple ranges and depths agree well with measurements. Furthermore, single-view coverage assessment results are presented corresponding to single-view SAS images. This study therefore demonstrated that high-quality coverage assessment results can be efficiently obtained to aid UXO survey planning and evaluation.

As already mentioned, acoustic seabed parameters have a large influence on the range and depth coverage. When there remains a significant uncertainty in these parameters, range and depth coverage cannot be established by using the proposed model-based approach. It is then essential to deploy well-known objects in the operational area such that the range and depth coverage can be measured for a specific test object. The modelling approach can subsequently be used to extrapolate the results to different target depths.

13.2 Outlook

The current study demonstrated the feasibility of the coverage assessment approach. To enable the assessment of UXO surveys, the following four topics deserve consideration for further analysis:

1) In this report, single-view coverage assessment has been investigated and demonstrated. For the evaluation of UXO surveys, it is needed to generalize the results to include multiple-view coverage to evaluate the coverage achieved in an entire UXO survey.
2) The results presented in the current report are generated for an ad-hoc detector with an SRR detector threshold. It is of interest to extend the analysis to a state-of-the-art detector. It is of interest to include target classification/false alarm reduction as well in the analysis, since the tolerance to the number of false positives limits the detection performance.
3) It is of interest to apply the developed methodology to other UXO targets, for example to investigate the detectability of small-caliber UXO targets, or targets with a different shape.
4) It is of interest to apply the method to different LF-SAS systems or different system configurations (e.g. downlooking), to learn how to optimally conduct UXO surveys given specific environmental conditions, UXO of interest, and target depth.
5) Based on coverage assessment, the effectiveness of acoustic techniques for UXO detection can be evaluated. In gassy sediments, coverage assessment should indicate that acoustic techniques are not able to provide coverage, which means that non-acoustic techniques, such as magnetic or electromagnetic induction (EMI) techniques, should be considered in those situations instead.

The potential benefit is that valuable insights will be obtain how to plan, execute, and evaluate UXO surveys.

14 References

[1] Beckers, A.L.D., “The hunt for buried objects”, Maritime/Air Systems and Technologies, Amsterdam, 2016.

[2] Bucaro, J.A., Sarkissian, A., Houston, B.H., Saniga, M., “Effects of Target Corrosion/Bio-fouling on EMI & Structural Acoustic Signatures in Underwater Environments – Acoustic Component”, SERDP MR-2500, Final Report, 2017.

[3] Gutowski, M., Bull, J.M., Dix, J.K., Henstock, T.J., Hogarth, P., Hiller, T., Leighton, T.G., White, P.R. “3D high-resolution acoustic imaging of the sub-seabed”, Applied Acoustics, vol. 69, p. 262–271, 2008.

[4] Vardy, M.E., Dix, J.K., Henstock, T.J., Bull, J.M., Gutowski, M. “Decimeter-resolution 3D seismic volume in shallow water: a case study in small-object detection”, Geophysics, vol. 73, no. 2, p. B33–B40, 2008.

[5] Pangeo website, Sub-Bottom Imager flyer, https://www.pangeosubsea.com/wp-content/uploads/2019/05/PanGeo-SBI.pdf.

[6] Brown, D.C., Johnson, S.F., Brownstead, C.F. “Sediment Volume Search Sonar”, SERDP MR-2545, symposium presentation, 2018.

[7] Schock, S.G., Tellier, A., Wulf, J., Sara, J., Ericksen, M. “Buried Object Scanning Sonar”, IEEE Journal of Oceanic Engineering, vol. 26, no. 4, 2001.

[8] Schock, S.G., Wulf, J., Quentin, G., Sara, J. “Synthetic aperture processing of buried object scanning sonar data”, OCEANS MTS/IEEE, 2005.

[9] Sara, J., “Next Generation Buried Object Scanning Sonar (BOSS) for Detecting Buried UXO in Shallow Water”, SERDP MR-2752.

[10] Sternlicht D.D., Fernandez, J.E., Holtzapple, R., Kucik, D.P., Montgomery, T.C., Loeffler, C. M. “Advanced Sonar Technologies for Autonomous Mine Countermeasures”, OCEANS MTS/IEEE KONA 2011.

[11] Sternlicht, D.D., Fernandez, J.E., Prater, J.L., Weaver, J.N., “Advanced Sonar Technologies for High Clearance Rate Mine Countermeasures”, OCEANS MTS/IEEE Monterey 2016.

[12] Houston, B., “Demonstration of AUV-Based Structural Acoustic Look-Down and Side-Look Sonars for Underwater Buried UXO Detection and Classification”, SERDP MR-201714.

[13] Houston, B., “Wide-Area Detection and Identification of Underwater UXO Using Structural Acoustic Sensors”, SERDP MR-1513.

[14] Houston, B., “Structural Acoustic UXO Detection and Identification in Marine Environments”, SERDP MR-2103.

[15] Vossen, R. van, “Detection of Underwater Unexploded Ordnance in Mud”, SERDP MR-2200.

[16] Vossen, R. van, “UXO Detector for Underwater Surveys Using Low-Frequency Sonar”, SERDP MR-2415.

[17] Schneider von Deimling, J., Held, P., Feldens, P., and Wilken, D. “Effects of using inclined parametric echosounding on sub-bottom acoustic imaging and advances in buried object detection”, Geo-Marine Letters, vol. 36, no. 2, 2015.

[18] Ainslie, M.A., “Principles of sonar performance modelling”, Springer, 2010.

[19] Williams, K.L., Jackson, D.R., Tang, D., Briggs, K.B., Thorsos, E.I., “Acoustic backscattering from a sand and a sand/mud environment: experiments and data/model comparisons”, IEEE Journal of Oceanic Engineering 34, 388-398, 2009.

[20] Synnes, S.A., Hansen, R.E., and Torstein Olsmo, S., “Assessment of shallow water performance using interferometric sonar coherence.”, Proceedings of Underwater Acoustic Measurements 2009: Technologies & Results (UAM); 2009-06-21 - 2009-06-26, 2009.

[21] Zampolli, M., Tesei, A., Jensen, F.B., Malm, N., Blottman III, J.B., “A computationally efficient finite element model with perfectly matched layers applied to scattering from axially symmetric objects”, Journal of the Acoustical Society of America, Vol. 122, No. 3, 2007.

[22] Williams, K.L., Kargl, S.G., Thorsos, E.I., Burnett, D.S., Lopes, J.L., Zampolli, M., Marston, P.L., “Acoustic scattering from a solid aluminum cylinder in contact with a

sand sediment: Measurements, modeling, and interpretation", Journal of the Acoustical Society of America, Vol. 127, No. 6, 2010.

[23] Kargl, S.G., Williams, K.L., Marston, T.M., Kennedy, J.L., Lopes, J.L., "Acoustic Response of Unexploded Ordnance (UXO) and Cylindrical Targets", OCEANS 2010 – MTS/IEEE Seattle, 2010.

[24] Kargl, S.G., Marston, P.L., "Observations and modeling of the backscattering of short tone bursts from a spherical shell: Lamb wave echoes, glory, and axial reverberations", Journal of the Acoustical Society of America, Vol. 85, No. 3, 1989.

[25] Nijhof, M.J.J., Espana, A., Williams, K., "Efficient calculation of broadband acoustic scattering from a partially, obliquely buried cylinder", Proceedings of 1st International Conference Exhibition Underwater Acoustics, pp. 697-702, 2013.

[26] Abawi, A.T., "Finite Element Modeling of Scattering from Underwater Proud and Buried Military Munitions", SERDP MR-2408, 2017.

[27] Wilkens, R.H., and Richardson, M.D., "The influence of gas bubbles on sediment acoustic properties: in situ, laboratory, and theoretical results from Eckernförde Bay", Baltic sea Continental Shelf Research 18, 1859-1892, 1998.

[28] Piper, J.E., Lim, R., Thorsos, E.I., Williams, K.L., "Buried sphere detection using a synthetic aperture sonar", IEEE Journal of Engineering 34, 485-494, 2009.

[29] Nijhof, M.J.J., Espana, A., Williams, K.L., "Improved modeling accuracy of the elastic object response by inclusion of higher order scattering", Underwater Acoustic Conference, Greece, 2014.

[30] Hansen, R.E., "Introduction to Synthetic Aperture Sonar', in: Sonar Systems, chapter 1, IntechOpen, 2011.

[31] Berkhout, A.J., "Applied seismic wave theory", Elsevier, 1987.

[32] Kallweit, R. S., Wood, L. C., "The limits of resolution of zero-phase wavelets", Geophysics, 47 (07), p. 1035–1046, 1982.

[33] Ivakin, A., "A modeling approach to scattering and reverberation in shallow water.", The Journal of the Acoustical Society of America, vol. 138, pp. 1896-1896, 2015.

[34] Pinto, M., Bellettini, A., Wang, L.S., Munk, P., Myers, V., and Pautet, L., "A New Synthetic Aperture Sonar Design with Multipath Mitigation", Proc. High-Frequency Ocean Acoust. Conf., vol 728, pp. 489-496, 2004.

[35] Groen, J., Leier, S., Schmaljohann, H., and Jans, W., "Multipath and noise suppression by coherently processing images of an interferometric SAS system", 11th European Conference on Synthetic Aperture Radar, EUSAR 2016.

[36] Wang, L., Davies, G., Bellettini, A. and Pinto, M., "Multipath effect on DPCA micronavigation of a synthetic aperture sonar", in: Impact of Littoral Environmental Variability of Acoustic Predictions and Sonar Performance, pages 465– 472. Springer, 2002.

[37] Chen, Q, Xu, W., Pan, X., and Li, J., "Wideband Multipath Rejection in Synthetic Aperture Sonar Imaging", OCEANS 2008 - MTS/IEEE Kobe Techno-Ocean, pp. 1-6, 2008.

[38] Davis, B.J., Gough, P.T., and B.R. Hunt, "Modeling Surface Multipath Effects in Synthetic Aperture Sonar", IEEE Journal of Oceanic Engineering, Vol. 34, No. 3, 2009.

[39] Gonzalez, J.A.C, de Figueiredo, J.J.S, Coimbra, T.A., Schleicher, J., and Novais, A., "Migration velocity analysis using residual diffraction moveout: a real-data example", J. Geophys. Eng. 13, pp. 622–633, 2016.

[40] Zampolli, M., Tesei, A., Canepa, G., Godin, O.A., "Computing the far field scattered or radiated by objects inside layered fluid media using approximate Green's functions", Journal of the Acoustical Society of America 123 (6), pp. 4051–4058, 2008.

[41] Anderson, J.T., Van Holliday, D., Kloser, R., Reid, D.G., and Simard, Y., Acoustic seabed classification: current practice and future directions, ICES Journal of Marine Science, vol. 65, no. 6, pp. 1004–1011, 2008.

[42] Kenny, A.J., Cato, I., Desprez, M., Fader, G., Schüttenhelm, R.T.E., and Side, J., An overview of seabed-mapping technologies in the context of marine habitat classification, ICES Journal of Marine Science, vol. 60, no. 2, pp. 411–418, 2003

[43] Penrose, J., Siwabessy, P.J., Gavrilov, A., Parnum, I., Hamilton, L. Bickers, A., Brooke, B., Ryan, D., and Kennedy, P. Acoustic Techniques for Seabed Classification, CRC for Coastal Zone, Estuary & Waterway Management, 2006.

[44] Hamilton, L.J., Acoustic Seabed Classification Systems, DSTO Technical Note DSTO-TN-0401, 2001.

[45] Wilson, P.S., Knobles, D.P., and Neilsen, T.B., Guest Editorial – An Overview of the Seabed Characterization Experiment, IEEE Journal of Oceanic Engineering, vol. 45, no. 1, pp. 1–13, 2020.

[46] Ballard, M.S., Lee, K.M., McNeese, A.R., Wilson, P.S., Chaytor, J.D., Goff, J.A., and Reed, A.H., In Situ Measurements of Compressional Wave Speed During Gravity Coring Operations in the New England Mud Patch, IEEE Journal of Oceanic Engineering, vol. 45, no. 1, pp. 26–38, 2020.

[47] Yang, J., and Jackson, D.R., Measurement of Sound Speed in Fine-Grained Sediments During the Seabed Characterization Experiment, IEEE Journal of Oceanic Engineering, vol. 45, no. 1, pp. 39–50, 2020.

[48] Barclay, D.R., Bevans, D.A. and Buckingham, M.J., Estimation of the Geoacoustic Properties of the New England Mud Patch From the Vertical Coherence of the Ambient Noise in the Water Column, IEEE Journal of Oceanic Engineering, vol. 45, no. 1, pp. 51–59, 2020.

[49] Belcourt, J., Dosso, S.E., Holland, C.W., and Dettmer, J., Linearized Bayesian Inversion for Experiment Geometry at the New England Mud Patch, IEEE Journal of Oceanic Engineering, vol. 45, no. 1, pp. 60–68, 2020.

[50] Bonnel, J., Dosso, S.E., Eleftherakis, D., and Chapman, N.R., Trans-Dimensional Inversion of Modal Dispersion Data on the New England Mud Patch, IEEE Journal of Oceanic Engineering, vol. 45, no. 1, pp. 116–130, 2020.

[51] Brown, E.M., Lin, Y., Chaytor, J.D., Siegmann, W.L., Geoacoustic Inversion for a New England Mud Patch Sediment Using the Silt-Suspension Theory of Marine Mud, IEEE Journal of Oceanic Engineering, vol. 45, no. 1, pp. 144–160, 2020.

[52] Knobles, D.P., Wilson, P.S., Goff, J.A., Wan, L. Buckingham, M.J., Chaytor, J.D., and Mohsen, B., Maximum Entropy Derived Statistics of Sound-Speed Structure in a Fine-Grained Sediment Inferred From Sparse Broadband Acoustic Measurements on the

New England Continental Shelf, IEEE Journal of Oceanic Engineering, vol. 45, no. 1, pp. 161–173, 2020.

[53] Michalopoulou, Z., and Gerstoft, P., Multipath Broadband Localization, Bathymetry, and Sediment Inversion, IEEE Journal of Oceanic Engineering, vol. 45, no. 1, pp. 92–102, 2020.

[54] Potty, G.R., and Miller, J. H., Effect of Shear on Modal Arrival Times, IEEE Journal of Oceanic Engineering, vol. 45, no. 1, pp. 103–115, 2020.

[55] Belcourt, J., Holland, C.W., Dosso, S.E., Dettmer, J. and Goff, J.A., Depth-Dependent Geoacoustic Inferences With Dispersion at the New England Mud Patch via Reflection Coefficient Inversion, IEEE Journal of Oceanic Engineering, vol. 45, no. 1, pp. 69–91, 2020.

[56] Lin, Y., Bonnel, J., Knobles, D.P., and Wilson, P.S., Broadband Waveform Geoacoustic Inversions With Absolute Travel Time, IEEE Journal of Oceanic Engineering, vol. 45, no. 1, pp. 174–188, 2020.

[57] Lied, T.T., Walday, M., Olsgard, F., Ellingsen, K. and Holm, S., SEABEC - A single beam echo sounder seabed classification system, MTS/IEEE Techno-Ocean '04: Bridges across the Oceans - Conference Proceedings, vol. 4., pp. 2024–2028, 2004.

[58] Hamilton, L., Acoustic seabed segmentation for echosounders through direct statistical clustering of seabed echoes. Continental Shelf Research, vol. 31, no. 19, pp. 2001–2011, 2011.

[59] Saleh, M., and Rabah, M., Seabed sub-bottom sediment classification using parametric sub-bottom profiler, NRIAG Journal of Astronomy and Geophysics, vol. 5, no. 1, pp. 87–95, 2016.

[60] Alevizos, E., Snellen, M., Simons, D., Siemes, K., and Greinert, J., Multi-angle backscatter classification and sub-bottom profiling for improved seafloor characterization, Marine Geophysical Research, vol. 39, pp. 289–306, 2018.

[61] Eidem, E.J., and Landmark, K., Acoustic seabed classification using QTC IMPACT on single-beam echo sounder data from the Norwegian Channel, northern North Sea. Continental Shelf Research. Vol. 68, pp. 1–14, 2013.

[62] Ferretti, R., Fumagalli, E., Caccia, M. and Bruzzone, G., Seabed classification using a single beam echosounder, OCEANS 2015 - Genova, Genoa, pp. 1–5, 2015.

[63] Simons, D.G., and Snellen, M., A Bayesian approach to seafloor classification using multi-beam echo-sounder backscatter data, Applied Acoustics, vol. 70, pp. 1258–1268, 2009.

[64] Huang, Z., Siwabessy, J., Cheng, H., and Nichol, S., Using Multibeam Backscatter Data to Investigate Sediment-Acoustic Relationships, Journal of Geophysical Research, vol. 123, no. 7, pp. 4649–4665, 2018.

[65] Gaida, T.C., Snellen, M., van Dijk, T.A.G.P., and Simons, D.G., Geostatistical modelling of multibeam backscatter for full-coverage seabed sediment maps. Hydrobiologia, vol. 845, pp. 55–79, 2019.

[66] Cutter, G.R., and Demer, D.A., Seabed classification using surface backscattering strength versus acoustic frequency and incidence angle measured with vertical, split-beam echosounders, ICES Journal of Marine Science, vol. 71, pp. 882–894, 2014.

[67] Marston, T.M., Marston, P.L., Williams, K.L., Scattering resonances, filtering with reversible SAS processing, and applications to quantitative ray theory, OCEANS, 2010.

[68] Puleo, J., Mobility and burial of variable density munitions in the inner surf and swash zones during controlled extreme forcing, SERDM MR20-1094.

[69] van den Berg, J.H., Boersma, J.R., van Gelder, A., Diagnostic sedimentary structures of the fluvial-tidal transition zone - Evidence from deposits of the Rhine and Meuse, Netherlands Journal of Geosciences - Geologie en Mijnbouw, vol. 86, nr. 3, pp. 287-306, 2007.